THE UNIVERSITY OF CALGARY

Impact of Rubidium Clock Aiding on GPS Augmented Vehicular Navigation

by

Zhaonian Zhang

A THESIS
SUBMITTED TO THE FACULTY OF GRADUATE STUDIES
IN PARTIAL FULFILMENT OF THE REQUIREMENTS FOR THE
DEGREE OF MASTER OF SCIENCE

DEPARTMENT OF GEOMATICS ENGINEERING

CALGARY, ALBERTA
DECEMBER, 1997

ABSTRACT

The characteristics of a rubidium clock and the relationship between the clock offset error and position error were investigated. An adaptive filter algorithm and a rubidium clock aided GPS navigation System were developed, based on the characteristics of the rubidium clock. An integrated navigation system consisting of GPS with a rubidium clock, a barometer and a gyro was designed. Decentralized Kalman filters were employed and a software was developed to test the integrated navigation system. Two field tests were conducted at Nose Hill Park, Calgary and in downtown Calgary, respectively. The test results have shown that rubidium clock aided GPS is a practical approach; it can improve positioning accuracy, especially vertical accuracy, significantly; it is able to navigate using three satellites, and therefore, improve the navigation availability significantly; the integrated navigation system developed herein can improve navigation availability, for the case tested, by over 50%.

ACKNOWLEDGEMENTS

I would like to express my gratitude to my supervisor, Dr. Gérard Lachapelle, for his continued support and encouragement throughout my MSc program. His guidance and advice are greatly appreciated.

I would like to thank my colleagues Huangqi Sun, Jamie Henriksen, Weigen Qiu, Nobuyuki Hayashi, Chuanya Tang, Kirk Collins, Brad Groat, Hubiao Lan, John Raquet, Shawn Weisenburger, Robert Harvey and Thomas Morley, for their help. Jim Stephen is acknowledged for reviewing and editing the manuscript.

My deepest thanks are for my wife, Zheng Li, for her kindly allowing GPS signals to fill our home when I was working on my thesis. This thesis would never be done without her love and support.

TABLE OF CONTENTS

LIST OF TABLES

LIST OF FIGURES

NOTATION

Symbols:

A	nominal amplitude
AZ_i	the azimuth angle from the user to satellite i (= 1, 2, ..., n)
$a_1 = e^{-\frac{\Delta t}{\tau}}$	the parameter to be estimated
c	speed of light
C^j	correction to the pseudorange measurement for the satellite j
$c\delta t$	range clock offset error
$c\delta\omega_t$	range clock drift error
d	least squares adjustments to parameters
d^j	distance between the receiver and the satellite j
$d\rho$	range error induced by orbital error
dt	satellite clock error
dT	receiver clock offset
d_{ion}	ionospheric delay
d_{trop}	troposhperic delay
dT_m	receiver clock offset measurement
dT	real receiver clock offset measurement
El_i	the elevation angle from the user to satellite i (= 1, 2, ..., n)
H	design matrix
h	height
ht	true height
l	observation vector
n	number of all satellites in view
N	sampling number
p	range measurement
p(t)	in-phase low-pass process
p^j_{ref}	pseudorange measurement at the reference station for the satellite j
P^j	corrected pseudorange measurement for the satellite j
p^j_{rmt}	pseudorange measurement at the remote station for the satellite j
q(t)	quadrature low-pass process
r_ρ	variance of the pseudo-range measurement
$r_{\dot\rho}$	variance of the Doppler measurement

r_b	variance of the barometric height measurement
r_t	variance of the clock offset measurement
r_g	variance of the gyro heading measurement
Rx(k)	auto-correlation function of the process x_k
s_m	white noise spectral amplitude for W_m
$\varepsilon(t)$	amplitude low-pass noise process
t	real clock offset
dt	clock offset estimation error
ΔT	difference between the initial clock offset and the estimated clock offset
T_{rx}	clock offset estimate via single point positioning estimation
$V = \sqrt{V_E^2 + V_N^2}$	horizontal speed
V_E	GPS longitude velocity
$\mathbf{v}_l = \begin{bmatrix} v_b & v_t & v_g \end{bmatrix}^T$	measurement errors of barometric height, clock offset and gyro heading
V_N	GPS latitude velocity
$\mathbf{v}_\rho = \begin{bmatrix} v_{\rho 1} & \cdots & v_{\rho n} \end{bmatrix}^T$	pseudo-range measurement (white) noises
W	white noise
W_g	white noise drift
W_G	white noise driving process
W_m	white noise driving process
W_{mg}	driving white noise
W_k	sampling value of the white noise at the time of $t = k \cdot \Delta t$
X	GPS position and time solution
X_{ECEF}	vector of errors in estimation of position and clock offset
x	system state vector
x_0	nominal point of linearization based on predicted position and receiver time
x_k	sampling value of the height error at the time of $t = k \cdot \Delta t$
X_k	the value of the input signal at the time of t_k
X_{LTP}	vector of errors in estimation of latitude, longitude, height and clock offset
Y	vector of range measurement residuals
Y_e	vector of range measurement errors

Y_k	the value of the LPF output at the time of t_k
$\mathbf{Z}_p$	pseudo-range error
$\left[\alpha_{xi}\ \alpha_{yi}\ \alpha_{zi}\right]$	directional cosines of estimated line-of-site between the user and satellite i
ε_T	receiver clock offset measurement error
λ_u	estimated latitude of the user
ϕ_u	estimated longitude of the user
$\gamma(t)$	complex envelope
$\phi(t)$	phase low-pass noise process
τ	the time constant of the LPF
ρ	real range between the satellite and the receiver
ε_p	receiver noise.
ϕ	latitude
λ	longitude
σ_i^2	GPS range error variance for the i-th satellite $i = 1,\ldots,n$
σ_T^2	receiver clock offset measurement error variance
τ_m	correlation time
τ_G	correlation time
δv_m	velocity of the barometric height error
Δt	sampling interval
Ψ_0	initial heading, which satisfies
$\delta\Psi_g$	gyro heading error
$\delta\omega_g$	gyro drift
$\delta\omega_g$	random bias drift
$\delta\omega_m$	first-order Gauss-Markov process drift
τ_{mg}	correlation time
δV_E	GPS longitude velocity error
δV_N	GPS latitude velocity error
σ_E^2	variance of GPS longitude velocity error
σ_N^2	variance of GPS latitude velocity error
$\sigma_V^2 = \sigma_E^2 = \sigma_N^2$	variance of the GPS velocity error
δP_E	longitude position error

δV_E	longitude velocity error
δP_N	latitude position error
δV_N	latitude velocity error
δH	vertical position error
δV_H	vertical velocity error
ρ_i	measured pseudo-range
$\hat{\rho}_i(x_0)$	predicted pseudo-range based on x_0
$\dot{\rho}_i$	measured Doppler
$\hat{\dot{\rho}}_i(x_0)$	predicted pseudo-range based on x_0

Operators:

$\mathbf{A}^T$	matrix transpose
$\mathbf{A}^{-1}$	matrix inverse
$\bar{s}(t)$	Hilbert transform of s(t)
$\frac{df}{dt}$	partial derivative of the function f with respect to t

Acronyms:

AS	Anti-Spoofing
AR model	Autoregressive model
C/A code	Coarse/Acquisition code
DGPS	Differential GPS
DRMS	Distance Root Mean Square
ECEF	Earth-Center Earth-Fixed
EDOP	East Dilution of precision
FM	Frequency Modulation
GDOP	Geometric Dilution of Precision
GPS	Global Positioning System
HDOP	Horizontal Dilution of Precision
L1	L1 carrier (1575.42 MHz)
L2	L2 carrier (1227.6 MHz)
LPF	Low Pass Filter
NDOP	North Dilution of Precision
OEM	Original Equipment Manufacturer
P Code	Precision code
PC	Personal Computer
PDOP	Positional Dilution of Precision
PN	Pseudo Noise

PRN	Pseudo Random Memory
PV	Position - Velocity
PVA	Position - Velocity - Acceleration
RAIM	Receiver Autonomous Integrity Monitoring
RMS	Root Mean Square
SA	Selective Availability
SV	Space Vehicle
TDOP	Time Dilution of Precision
VDOP	Vertical Dilution of Precision
WGS84	World Geodetic System of 1984
Y code	Encrypt P code

CHAPTER 1
INTRODUCTION

It is well known that clocks are at the heart of the GPS. In order to ensure the stability of transmission over several revolutions of the space vehicles and adequate tracking to update the satellite orbit, and afford sufficient predictability in the clock's performance, very precise and stable clocks are installed on the satellites. In most GPS receivers, on the other hand, inexpensive crystal clocks are used.

1.1 Role of Clocks in GPS Receivers

The primary measurements made by a GPS receiver are the times of arrival of the satellite generated signals. Arrival time is measured with respect to the receiver clock which is a stable oscillator and counter. Signal-to-noise considerations preclude direct measurement of the arrival time of a particular PN code element edge. A replica PN code sequence generator is made to run in phase with the modulation of the incoming signal by a tracking loop. Simultaneously, the power recovered by the correlation of the incoming signal against slightly advanced and delayed versions of the local replica are compared to provide the tracking error indication. The arrival time may then be observed by comparing the replica code timing with the receiver clock timing. Either the clock time can be observed upon the occurrence of certain events of the replica, such as the first edge of a data word, or the phase of the replica relative to a hypothetical replica driven by the receiver clock, such as 1 second ticks.

The time and frequency offsets of the receiver clock from the GPS time system and true frequency are not critical, since these are determined from the navigation solutions. This approach basically allows the use of an inexpensive crystal oscillator as the receiver clock and makes GPS practical for wide use.

Usually, and always to some advantage, a more sophisticated viewpoint is taken which allows for utilization of additional inputs and thereby improving the solution in terms of accuracy and reliability under unfavorable conditions. Even in the absence of external inputs, there is a benefit to be obtained if the receiver clock is stable. It becomes possible to predict what the clock offset will be, and the number of unknowns in the navigation solution is reduced to three. If four measurements are still available, the redundant measurement can be used to improve the accuracy, availability and reliability of the solution. With encouraging developments in the time reference industry and a trend toward a higher stability at lower prices, it is of interest to investigate the advantages of receiver clock stability for GPS positioning and navigation.

Previous work on receiver clocks attempted to exploit higher stability for navigation and receiver autonomous integrity monitoring (RAIM). When the satellite coverage is sparse or the satellite geometry poor, "clock coasting" over relatively short periods has been proposed to skip estimation of the clock offset [Sturza, 1984]. The clock offset is held fixed at the last estimated value [Lee, 1993], or propagated forward in time using model parameters estimated before the period of poor coverage [McBurney & Brown, 1988]. When a low-cost atomic clock is added to a GPS receiver, the vertical accuracy and navigation availability will be improved significantly [Murphy & Skidmore, 1994]. A quadratic function model can also be developed to predict the receiver clock offset [Misra et al., 1995a]. It is proven that clock coasting with an atomic clock would improve RAIM availability [Lee, 1993]. Clock-aided RAIM, an effective approach based on receiver clock modeling to predict its offset, is presented in [Misra et al., 1995b].

1.2 Research Objectives and Thesis Outline

This thesis investigates the performance of a rubidium clock aided GPS receiver and determines the benefits of using a rubidium clock, while focusing on the improvement in navigation accuracy and availability.

The motivation for employing an atomic clock in a GPS receiver is that the timing is precise and stable enough so that the receiver clock offset from GPS time can be assumed known, avoiding its estimation. Therefore, GPS navigation can proceed by estimating only the position coordinates (x, y, z), i.e., only three satellites are needed. If the receiver clock offset is precisely known, the immediate question is in what environment and to what extent the position accuracy will be improved. Chapter 2 will answer this question by analyzing the relationship between clock offset error and position error, and looking into the effect of satellite geometry on their relationship.

While a quadratic function is an effective model to estimate the clock offset on the basis of GPS measurements, previous independent measurements are needed to estimate the parameters of the quadratic function. The available number of independent measurements depends upon the correlation time of the measurements. The error due to SA in GPS range measurements has been observed to have a correlation time of about 3-4 minutes. The correlation due to unmodeled ionospheric delay, however, may persist for several hours. In differential mode, the effects of both SA and ionosphere are substantially removed, and the correlation time is reduced to about 1 minute. The need for a more effective and practical model for the rubidium clock will be also addressed. In Chapter 3, the oscillator model and measurements will be briefly reviewed, then the characteristics of a rubidium clock are examined using precise post-mission precise satellite orbits and clock corrections. Based on these characteristics, a rubidium clock model for both stand-alone and differential GPS is developed. A practical navigation algorithm, in which the clock offset is estimated by a sequential process, is developed in Chapter 4.

To further improve GPS navigation availability, the integration of rubidium clock aided GPS with a barometer and a gyro is investigated in Chapter 5. The integrated navigation system is aimed at overcoming the GPS outages for land vehicle navigation in urban areas. The combination of precise clock aided GPS with a barometer is an ideal integration. When the satellite geometry is good, the rubidium clock is used to improve vertical

accuracy, and in turn, the calibration accuracy of the barometer. When the number of visible satellites falls to two, the stable rubidium clock and the more accurately calibrated barometer will provide the good measurements of clock offset and height information, and navigation quality can still be maintained. The gyro is also helpful over short periods of time, when there is only one visible satellite.

Field tests in both a controlled environment and downtown area were conducted to evaluate the navigation performance of the rubidium clock aided GPS and the integrated navigation system. Chapter 6 describes the tests and analyzes the results. Chapter 7 gives conclusions and recommendations.

CHAPTER 2
RELATIONSHIP BETWEEN CLOCK OFFSET ERROR AND POSITION ERROR

Since the rubidium clock makes it possible to predict the receiver clock offset, positioning accuracy could be enhanced through an improvement in clock offset estimation. To understand why and to what extent the position accuracy can be improved by rubidium clock aiding, the correlation between the clock offset error and position error needs to be investigated.

2.1 Analysis of Correlation Coefficients

To explore the relationship between clock offset error and position error, it is necessary to begin from the basic GPS navigation equation. In the Earth-Centered-Earth-Fixed (ECEF) coordinate system, the linearized navigation equation is given as

$$\mathbf{Y} = \mathbf{H} \cdot \mathbf{X}, \tag{2.1}$$

where $\mathbf{Y} = \begin{bmatrix} \Delta p_1 & \Delta p_2 & \cdots & \Delta p_n \end{bmatrix}^T$

= range measurement residuals for satellite 1, 2, ... , n.

$\mathbf{X} = \begin{bmatrix} \Delta x & \Delta y & \Delta z & \Delta T \end{bmatrix}^T$

= difference between the initial position and time solution $\overline{\mathbf{X}}$ and the estimated solution $\hat{\mathbf{X}}$.

$$\mathbf{H} = \begin{bmatrix} \alpha_{x1} & \alpha_{y1} & \alpha_{z1} & -1 \\ \alpha_{x2} & \alpha_{y2} & \alpha_{z2} & -1 \\ \cdots & \cdots & \cdots & \cdots \\ \alpha_{xn} & \alpha_{yn} & \alpha_{zn} & -1 \end{bmatrix} = \text{design matrix.}$$

$\begin{bmatrix} \alpha_{xi} & \alpha_{yi} & \alpha_{zi} \end{bmatrix}$ = directional cosines of estimated line-of-site between the user and satellite i.

The pseudorange measurement errors and errors in estimation of the position and the clock offset satisfy the same equation

$$Y_e = H \cdot X_{ECEF}, \tag{2.2}$$

where $\mathbf{Y}_e = [\delta p_1 \ \delta p_2 \ \dots \ \delta p_n]^T$

= range measurement errors for satellite 1, 2, ... , n.

$\mathbf{X}_{ECEF} = [\delta x \ \delta y \ \delta z \ \delta T]^T$

= errors in estimation of position and clock offset.

In order to compute the horizontal and vertical error, the ECEF coordinate errors must first be transferred to Local Tangent Plane (LTP) errors, defined as Latitude, Longitude and Height errors at the estimated location, where the LTP is tangent to Ellipsoid. This results in the new design matrix

$$\mathbf{H}_{LTP} = \mathbf{H} \cdot \mathbf{T}_{ECEF->LTP} = \begin{bmatrix} \cos El_1 \cos Az_1 & \cos El_1 \sin Az_1 & \sin El_1 & 1 \\ \cos El_2 \cos Az_2 & \cos El_2 \sin Az_2 & \sin El_2 & 1 \\ \dots\dots & \dots\dots & \dots\dots & \dots\dots \\ \cos El_n \cos Az_n & \cos El_n \sin Az_n & \sin El_n & 1 \end{bmatrix},$$

where El_i is the elevation angle from the user to satellite i (= 1, 2, ..., n).

Az_i is the azimuth angle from the user to satellite i (= 1, 2, ..., n).

$$\mathbf{T}^T_{ECEF->LTP} = \begin{bmatrix} -\cos\lambda_u \sin\phi_u & -\sin\lambda_u \sin\phi_u & \cos\phi_u & 0 \\ -\sin\lambda_u & \cos\lambda_u & 0 & 0 \\ \cos\lambda_u \cos\phi_u & \sin\lambda_u \cos\phi_u & \sin\phi_u & 0 \\ 0 & 0 & 0 & 1 \end{bmatrix}$$

where λ_u is estimated latitude of the user

ϕ_u is estimated longitude of the user.

The error equation becomes

$$\mathbf{Y}_e = \mathbf{H}_{LTP} \cdot \mathbf{X}_{LTP}, \tag{2.3}$$

where $\mathbf{X}_{LTP} = \begin{bmatrix} \delta N & \delta E & \delta H & \delta T \end{bmatrix}^T$

= errors in estimation of latitude, longitude, height and clock offset,

also written as

$$\mathbf{X}_{LTP} = \mathbf{G} \cdot \mathbf{Y}_e , \tag{2.4}$$

where $\mathbf{G} = (\mathbf{H}_{LTP}^T \cdot \mathbf{H}_{LTP})^{-1} \cdot \mathbf{H}_{LTP}^T = \begin{bmatrix} g_{N1} & g_{N2} & \cdots & g_{Nn} \\ g_{E1} & g_{E2} & \cdots & g_{En} \\ g_{H1} & g_{H2} & \cdots & g_{Hn} \\ g_{T1} & g_{T2} & \cdots & g_{Tn} \end{bmatrix}$.

Assume that the range measurement errors δp_1 , δp_2 , ... , δp_n are all random variables which all have normal distribution with zero mean and the same variance σ^2, and independent from one another. The errors in the estimation of latitude, longitude, height and clock offset are

$$\begin{cases} \delta N = \sum_{i=1}^{n} g_{Ni} \delta p_i \\ \delta E = \sum_{i=1}^{n} g_{Ei} \delta p_i \\ \delta H = \sum_{i=1}^{n} g_{Hi} \delta p_i \\ \delta T = \sum_{i=1}^{n} g_{Ti} \delta p_i \end{cases} \tag{2.5}$$

which are zero mean random variables with variances of

$$\begin{cases} \sigma_N^2 = \sum_{i=1}^{n} g_{Ni}^2 \sigma^2 \\ \sigma_E^2 = \sum_{i=1}^{n} g_{Ei}^2 \sigma^2 \\ \sigma_H^2 = \sum_{i=1}^{n} g_{Hi}^2 \sigma^2 \\ \sigma_T^2 = \sum_{i=1}^{n} g_{Ti}^2 \sigma^2 \end{cases} \tag{2.6}$$

respectively. The covariances of the clock offset error with latitude, longitude and height errors are

$$\begin{cases} \mathrm{cov}(\delta T, \delta N) = \sum_{i=1}^{n} g_{Ti} g_{Ni} \sigma^2 \\ \mathrm{cov}(\delta T, \delta E) = \sum_{i=1}^{n} g_{Ti} g_{Ei} \sigma^2 \\ \mathrm{cov}(\delta T, \delta H) = \sum_{i=1}^{n} g_{Ti} g_{Hi} \sigma^2 \end{cases} \tag{2.7}$$

The correlation coefficients of the clock offset error with the latitude, longitude and height errors, which will be referred to as latitude-time, longitude-time and height-time correlation coefficients respectively, are

$$\begin{cases} \rho_{TN} = \dfrac{\sum_{i=1}^{n} g_{Ti} g_{Ni}}{\sqrt{\sum_{i=1}^{n} g_{Ti}^2} \sqrt{\sum_{i=1}^{n} g_{Ni}^2}} \\ \rho_{TE} = \dfrac{\sum_{i=1}^{n} g_{Ti} g_{Ei}}{\sqrt{\sum_{i=1}^{n} g_{Ti}^2} \sqrt{\sum_{i=1}^{n} g_{Ei}^2}} \\ \rho_{TH} = \dfrac{\sum_{i=1}^{n} g_{Ti} g_{Hi}}{\sqrt{\sum_{i=1}^{n} g_{Ti}^2} \sqrt{\sum_{i=1}^{n} g_{Hi}^2}} \end{cases} \tag{2.8}$$

They indicate the correlation between the clock offset error and the coordinate errors at each epoch. The larger the correlation coefficients, the more improvement in position accuracy the rubidium clock aided GPS can obtain by improving the clock offset estimation. However, the correlation coefficients between the clock offset and position errors in the horizontal component can be positive or negative over a period of time. They are the function of the DOPs and time.

2.2 Geometry and Correlation Coefficients

The theoretical expressions for the above correlation coefficients are complex and clumsy, as is the satellite geometry. It is difficult to see the effect of the satellite geometry on the correlation coefficients. A set of data and results of a static test are used to demonstrate the relationship between the clock offset error and the position error. This static test will also be used in later chapters to show the performance of the rubidium clock aided GPS.

2.2.1 Static test description

The static test was conducted on December 20, 1995 in Calgary. Two single-frequency GPS receivers, namely NovAtel GPSCards (10 channels), were modified to take an input from external atomic oscillators, one rubidium and the other a cesium. The antenna for the receiver with the rubidium clock was placed on a pillar, whose coordinates were precisely known in WGS84, on the roof of the Engineering Building at the University of Calgary. The other antenna for the receiver with the cesium clock was placed on the roof of the NovAtel Building, some 10 km away. L1 code measurements at 1 second intervals were collected over 3 hours and 45 minutes. Both set-ups employed chokerings to reduce multipath.

Single point positioning results were computed using the C^3NAV^{TM} software (Cannon et al 1995). A one second processing interval was used, and carrier phase smoothing of the pseudorange measurements was performed. C/A code position solutions were computed using an elevation cutoff angle of five degrees. Troposphere corrections were included in all processing. The data presented in this chapter was collected by the receiver equipped with the rubidium clock.

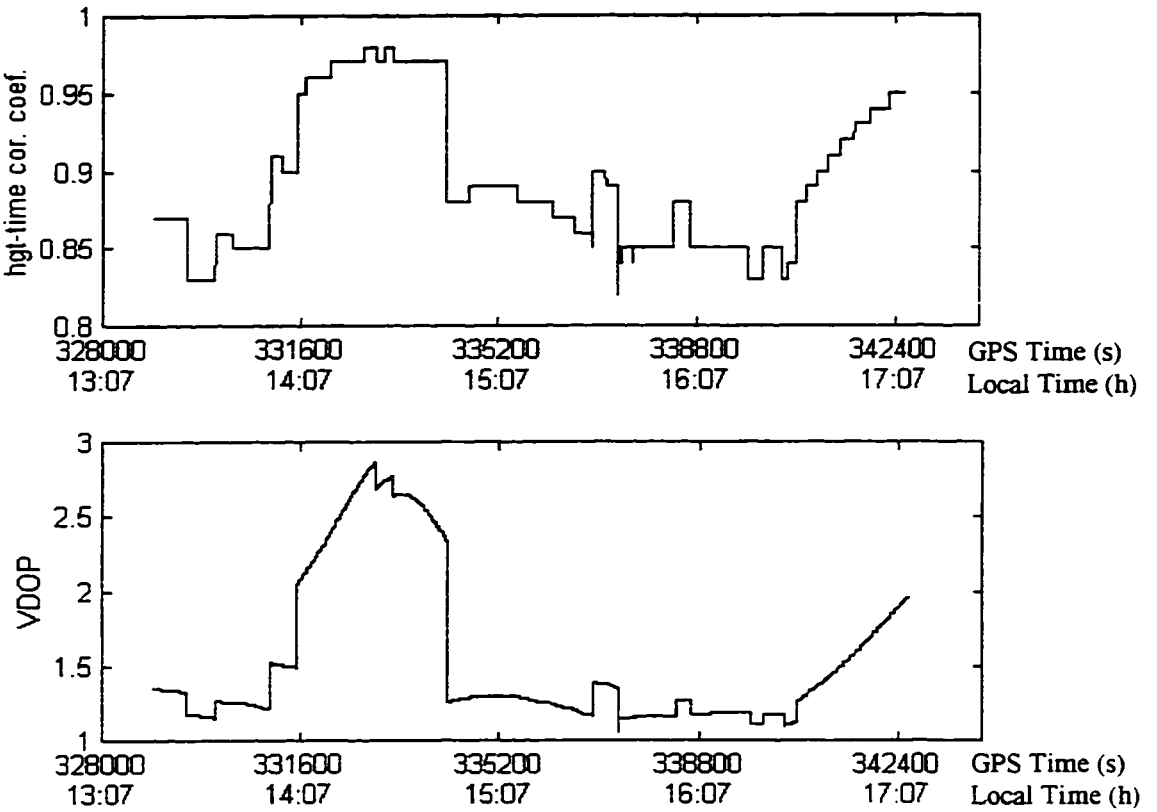

Figure 2.1 Height-time correlation coefficient and VDOP during the static test

2.2.2 Result analysis

Figure 2.1 presents the height-time correlation coefficient and VDOP during the static test. The height-time correlation coefficient always stays positive and close to 1. The larger the VDOP, the more closely the height-time correlation coefficient approaches 1. This is because all satellites are above the receiver, hence, the projection of range errors which result from the clock offset error on the height axis is always positive. The larger the VDOP, the more satellites are in high elevation, and the larger the projection of range errors on the height axis. Figure 2.2 presents the number of visible satellites. During GPS time of 331529 to 334260 seconds, the number of visible satellites falls down to six ,

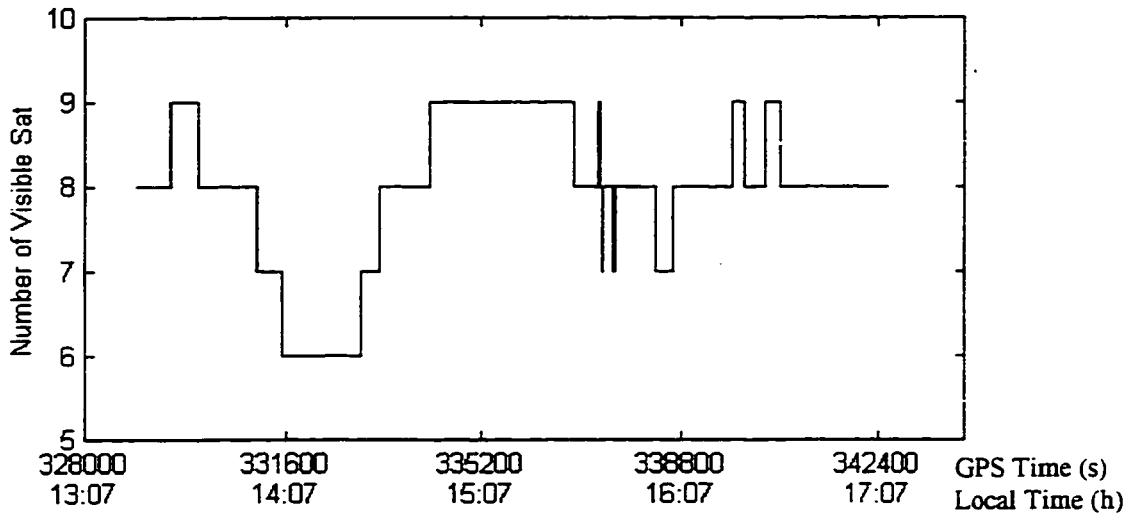

Figure 2.2 The number of visible satellites during the static test with cutoff angle of five degree

and the VDOP reaches its largest value. Figure 2.3a shows the satellite constellation during GPS time of 329422 to 329883 seconds, when the VDOP is better; Figure 2.3b shows the satellite constellation during GPS time of 331529 to 334260 seconds, when the VDOP is poorer.

Figure 2.4 and Figure 2.5 present the latitude-time and longitude-time correlation coefficients during the test. Since the satellites can be in any direction, the projection of range errors, which result from the clock offset error, on the latitude axis and/or longitude axis can be both positive and negative. The latitude-time and longitude-time correlation coefficients, therefore, change around zero. It is interesting to notice that the latitude-time correlation coefficient remains large and positive during GPS time of 331529 to 334260 seconds. Examining Figure 2.3b again, we find that most of satellites are on the north side during this period of time. It is obvious that the less the number of visible satellites, the lower the likelihood the satellite constellation keeps symmetry in latitude and/or longitude.

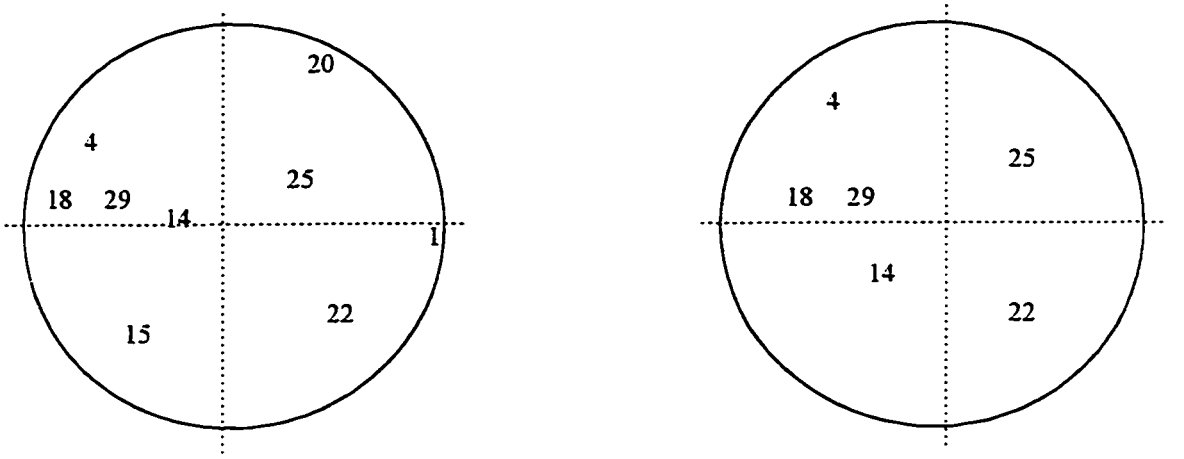

(a) the satellite constellation during 329422 to 329883

(b) the satellite constellation during 331539 to 334260

Figure 2.3 The satellite constellation during the static test

From the above analysis, we can summarize with the following conclusions:

1) The vertical error is almost linearly correlated to the clock offset error. The larger the VDOP, the more correlated the two errors.
2) The latitude error and longitude error is nearly independent of the clock offset error when the satellite geometry is good. The poorer the satellite geometry, the more likely the horizontal error is correlated to the clock offset error.
3) If the rubidium clock aiding can improve the clock offset estimation, it will definitely improve the vertical accuracy. Under poorer satellite geometry, it is also likely to improve the horizontal accuracy.

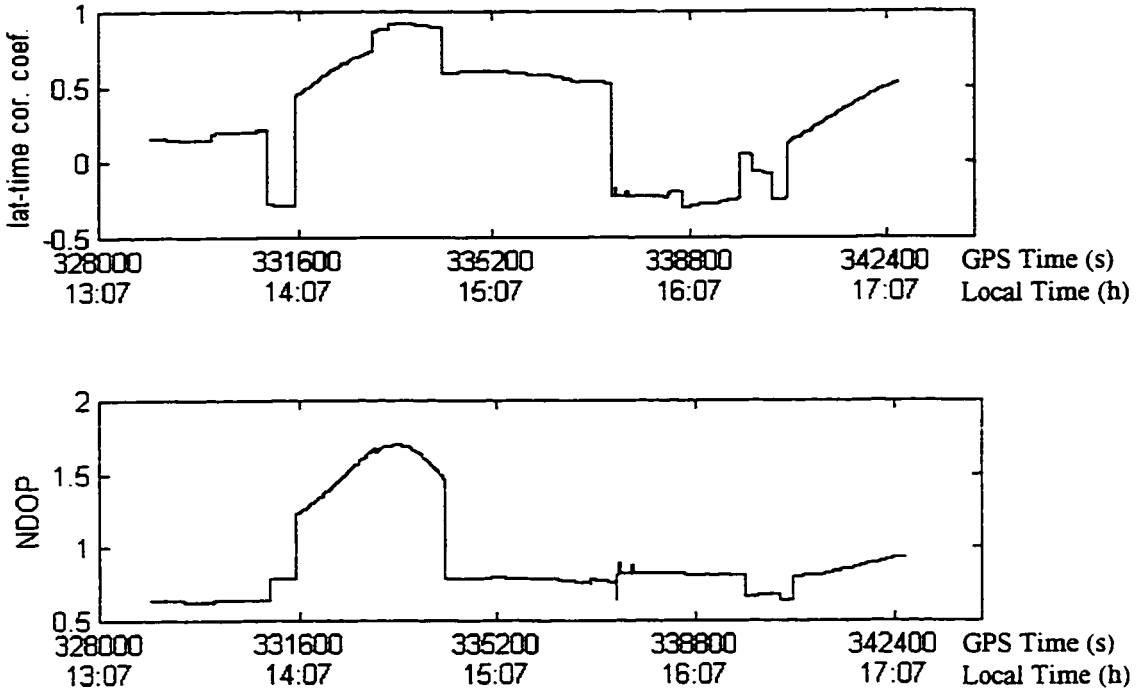

Figure 2.4 The latitude-time correlation coefficient and NDOP during the static test

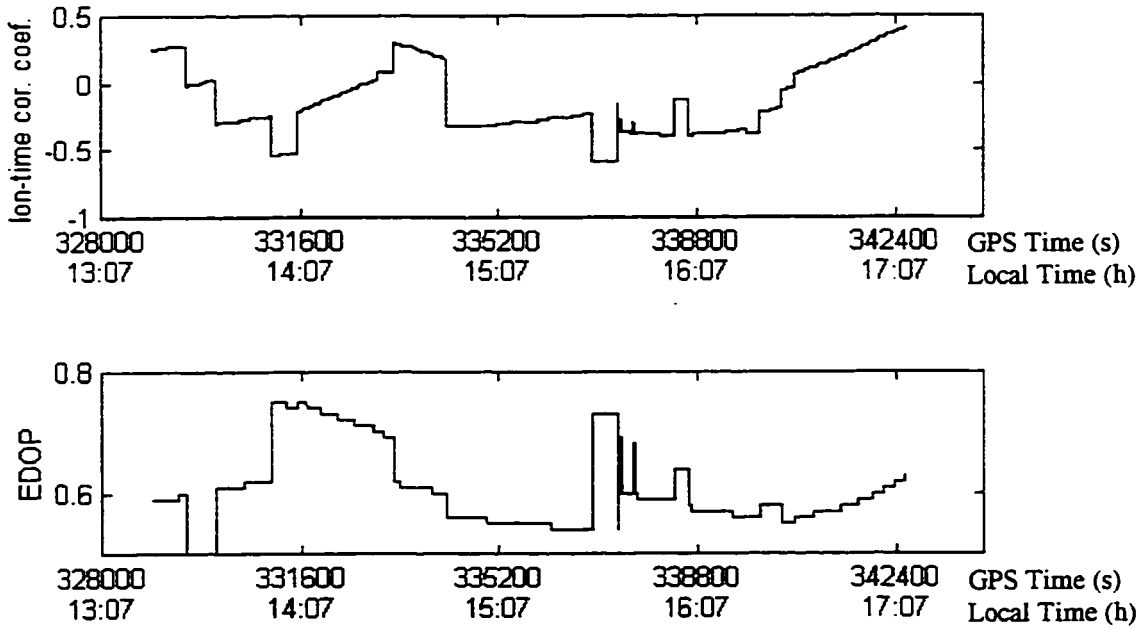

Figure 2.5 The longitude-time correlation coefficient and EDOP during the static test

CHAPTER 3
CHARACTERISTICS OF RUBIDIUM CLOCK

It is necessary to investigate the characteristics of the rubidium clock before modeling it for GPS navigation. While the GPS time system is very precise, the receiver clock offset solution is not accurate enough to evaluate the rubidium clock performance when SA is on. With post-mission precise orbits and satellite clock corrections, the receiver clock offset solution can be used to estimate the rubidium clock errors.

3.1 The Oscillator Model

The signal of the sinusoidal oscillator is a band-pass signal, centered about the carrier frequency f_0 . It can be modeled by a phasor (Bedrosian, 1962; Bernier & Gardiol, 1985), i.e.

$$Y(t) = A \cdot \gamma(t) \cdot \exp(j2\pi f_0 t) \tag{3.1}$$

where A is nominal amplitude,

$\gamma(t)$ is the complex envelope.

The real signal s(t) is the real part of the phasor

$$Y(t) = s(t) + j\bar{s}(t) \tag{3.2}$$

where $\bar{s}(t)$ is the Hilbert transform of s(t).

$\gamma(t)$ is a low-pass complex random process that represents the information modulated on the carrier (Papoulis, 1984)

$$\gamma(t) = p(t) + jq(t) = [1 + \varepsilon(t)]\exp(j\phi(t)) \tag{3.3}$$

where p(t) is an in-phase low-pass process

q(t) is a quadrature low-pass process

$\varepsilon(t)$ is an amplitude low-pass noise process

$\phi(t)$ is a phase low-pass noise process.

In the case of precision or low-noise oscillator, that is

$$\begin{cases} E\{\phi^2(t)\} << 1 \\ E\{\varepsilon^2(t)\} << 1 \end{cases}, \tag{3.4}$$

the phase noise may be expressed as

$$\exp(j\phi(t)) \approx 1 + j\phi(t). \tag{3.5}$$

The signal of the sinusoidal oscillator becomes

$$Y(t) = A \cdot \{1 + \varepsilon(t) + j\phi(t)] \cdot \exp(j2\pi f_0 t). \tag{3.6}$$

One may obtain

$$\begin{cases} p(t) = 1 + \varepsilon(t) \\ q(t) = \phi(t) \end{cases}. \tag{3.7}$$

The phase noise and the amplitude noise are orthogonal. This property enables the independent demodulation of the phase and amplitude noise process by synchronous demodulation. For the purpose of frequency stability analysis, the amplitude noise can be neglected and it is the phase noise that is relevant.

The time error process x(t) can be defined as the normalized phase difference accumulated between an oscillator used as a clock and a reference oscillator considered as errorless. It is related to the phase noise process by

$$x(t) = \frac{\phi(t)}{2\pi f_0} \tag{3.8}$$

where f_0 is the nominal frequency of the reference oscillator.

The normalized instantaneous frequency deviation y(t) is defined as

$$y(t) = \frac{dx(t)}{dt} = \frac{1}{2\pi f_0} \cdot \frac{d\phi(t)}{dt}. \tag{3.9}$$

It is a frequency "deviation" in the sense that being associated with the complex envelope, it does not describe the instantaneous frequency of the oscillator signal s(t), but the frequency deviation with respect to f_0.

The instantaneous frequency f(t) is related to y(t) by the following

$$y(t) = \frac{f(t) - f_0}{f_0}. \tag{3.10}$$

The normalized frequency deviation is conserved after frequency multiplication or division and it also enables the direct comparison between the frequency instability levels of two oscillators of different nominal carrier frequencies.

3.2 Time Domain Measurement

3.2.1 The true variance

The logical way to characterize frequency stability of an oscillator would be the true variance of the frequency samples (Sydnor & Allan, 1996):

$$I^2(\tau) = E\{y_k^2\} = \frac{1}{N}\sum_{i=1}^{N} y_i^2 . \tag{3.11}$$

The time series y_k is non-stationary, and the mean squared value of $y(t,\tau)$, which defines the true variance, diverges, i.e., becomes infinite when it is averaged over an infinite time. This is due to the non-stationary model representing the oscillator. This problem led to the definition of more appropriate measurements of frequency stability in the time domain, namely the Allan variance.

3.2.2 The Allan variance

The traditional or classical Allan variance is defined as (Allan, 1961)

$$\sigma_y^2(\tau) = \frac{1}{2}E\{(y_k - y_{k-1})^2\}. \tag{3.12}$$

With N successive samples of x(t) and the sampling interval τ, the Allan variance may be written as

$$\sigma_y^2(\tau) = \frac{1}{2\tau^2(N-2)}\sum_{i=1}^{N-2}(x_{i+2} - 2x_{i+1} + x_i)^2 , \tag{3.13}$$

where x_i is the time series of time error acquired.

3.3 GPS Time Standard

In terms of navigation accuracy, one nanosecond of time error is equivalent to approximately 0.3 metres of range error; this means that precision timing and frequency control are essential to the GPS system. All system timing requirements are synchronized with GPS system time, which is maintained by the Master Control Station (MCS) through the use of a set of highly accurate cesium clocks. Precision timing is maintained in the space vehicles by the use of highly stable atomic clocks (cesium and rubidium oscillators), which have stability of about 1 part in 10^{13} over a day (Martin 1980). The GPS system time, therefore, can be used to measure the time error of a rubidium clock.

To evaluate a rubidium clock by GPS system time, the clock is used in a phase-loop with a GPS receiver or as the oscillator of a GPS receiver. The receiver clock offset is with respect to GPS system time so it is this time offset which must be determined.

When SA is on, however, the accuracy of the receiver clock offset solution is approximately 340 nanoseconds (95%), which equates to a 2DRMS horizontal accuracy of 100 m. The receiver clock offset solution is not accurate enough to evaluate the atomic clock.

With post-mission precise orbits and satellite clock corrections, which are provided by NRCan (Kouba & Popelar, 1994, Gao et al. 1994), the height estimate is at the 2 m accuracy level when using a low code noise receiver (Henriksen et al. 1996, Skone et al. 1996). Since the height error is almost linearly correlated to the receiver clock offset error, the receiver clock offset has a similar accuracy level, which is approximately equivalent to 7 nanoseconds. The receiver clock offset solution with post-mission information is accurate enough to evaluate the rubidium clock.

3.4 GPS Receiver with an External Rubidium Clock

The GPS receiver with an external rubidium clock tested herein is composed of a NovAtel GPSCard™ 951R L1 GPS receiver, an Efratom Model FRK-LLN Rubidium clock, a Silicon Valley GPS Reference Frequency Generator and a PC computer, as shown in Figure 3.1.

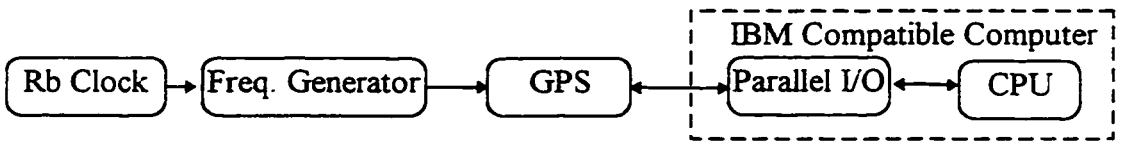

Figure 3.1 GPS receiver with an external rubidium clock

Table 3.1 Performance of NovAtel GPSCard™ 951R GPS receiver

Frequency	L1, 1575.43 MHz
Code tracked	C/A code (SPS)
Channels	10
Position Accuracy	15 metres CEP (SA off), GDOP<2 40 metres CEP (SA on) 1-5 metres CEP differential with standard reference station
Time Accuracy (relative)	50 nanoseconds (SA off) 250 nanoseconds (SA on)
Pseudorange Measurement Accuracy	10 cm RMS, no multipath, C/N>44 dBHz 25 cm RMS in multipath environment with Choke Ring
Singie Channel Phase Accuracy	3mm RMS, C/N>44 dBHz Loop BW=15 Hz
Differential Channel Phase Measurement Accuracy	0.75 mm RMS, 1 second smoothed, no multipath, C/N>44 dBHz
Velocity, Dynamics	515 metres per second
Acceleration, Dynamics	4g (sustained tracking)
Position Update Rate	10 solutions per second (100 msec)
Raw Data Availability Rate	20 data per second (50 msec)
Time to First Fix	70 seconds typical
Re-acquisition	3 seconds typical
Height Measurements	up to 18,288 metres (60,000 feet) maximum

The NovAtel GPS receiver's patented C/A code Narrow Correlator™ technology achieves pseudorange accuracy with near P-code performance and provides the robust resistance against errors introduced by multipath signals. Table 3.1 summarizes the receiver's performance (NovAtel 1994).

The Efratom Model FRK-LLN Rubidium clock is a compact, atomic resonance-controlled oscillator, which provides an extremely pure and stable sinusoidal signal of 10 MHz. Table 3.2 lists the performance specification for the rubidium clock (Ball Efratom 1989).

Table 3.2 Specifications for Efratom Model FRK-LLN rubidium clock

Output	10 MHz sine wave 1.0 Vrms into 50 ohms
Accuracy	Factory set to 10.0 MHz ± 5E-11 at shipment
Signal to Noise (SSB 1 Hz BW)	120 dB at 10 Hz and 147 dB at 100 Hz from carrier
Warm-up Characteristics	≤ 10 minutes to reach 2E-10 at 25 °C ambient
Retrace	± 2E-11
Long-term Stability	<4E-11/month
Sort-term Stability	3E-11 τ =1 sec 1E-11 τ =10 sec 3e-12 τ =100 sec
Trim Range	≥ 2E-9
Voltage Variation	<1E-10/10% change
Operating Temperature	<3E-10 from -25 °C to +65 °C
Magnetic Field	<4E-13/ AM^{-1} (3E-11/0.1 millitesla)
Altitude	<1E-13/mbar (sea level to 21,000 m)
Humility	95% MIL-5422F

The GPS Silicon Valley GPS Reference Frequency Generator provides an externally generated reference clock signal for the NovAtel GPSCard™. The card generates the 20.473 MHz reference signal required by the GPSCard™ (GPS Silicon Valley 1994). The signal is phase locked to the rubidium clock. This is necessary because the GPSCard™ does not accept the 10 MHz output of the rubidium clock.

3.5 Evaluation of Rubidium Clock by Using Post-mission Information

The data used herein is that collected in the static test described in Chapter 2. All point positioning results were computed using the C^{3}NAV^{TM} software and processed as previously described. The elevation cutoff angle was changed to ten degrees. Broadcast and post-mission satellite orbits and clock corrections were used respectively.

Section 4.1 will discuss rubidium clock modeling and Figure 4.1 shows the clock offset estimates using broadcast information and post-mission information for the rubidium clock. The fluctuation of the clock offset estimates using broadcast information is mainly the result of SA. Post-mission precise orbits and clock corrections eliminate SA. The clock offset estimates using post-mission information become very smooth.

Table 3.3 Comparison of specified Allan Variance with measured Allan Variance by GPS post-mission information for the rubidium clock

Sampling Interval (s)	Specification	Measured
1	3E-11	4.8E-10
10	1E-11	1.4E-10
100	3E-12	2.6E-11
300	N/A	8.4E-12
500	N/A	3.4E-12
1000	N/A	2.9E-12

Table 3.3 summarizes the results of evaluation of the rubidium clock. When the sampling interval is less than 300 seconds, the measured Allan variance of the rubidium clock is larger than the specifications provided by the manufacturer due to the GPS measurement noise. With the increase of sampling interval, the effect of the GPS measurement noise gradually decreases. On the other hand, the Allan variance for the rubidium clock is almost constant when the sampling interval is greater than 100 seconds and less than one day (Ball Efratom Division 1989). The measured Allan Variance approaches the specification provided by the manufacturer. It is believed that the appropriate sampling interval for evaluating the long term stability of the rubidium clock in this case is 500 seconds.

CHAPTER 4
RUBIDIUM CLOCK AIDED GPS

It was demonstrated in Chapter 2 that an improvement in the clock offset estimation will improve the position accuracy. The problem to be solved now is how to estimate the clock offset more accurately. With a knowledge of the characteristics of the rubidium clock, the proper modeling of the clock can be proposed for GPS navigation.

4.1 Rubidium Clock Modeling for Stand-alone GPS

In general, we cannot expect to know the true receiver clock offset. But we can estimate it from GPS measurements over a time period consistent with the stability characteristics of a given clock. How well and how far ahead such clock behavior can be predicted depends upon the stability characteristics of the clock.

The rubidium clock is a very stable clock. Figure 4.1 presents behavior typical of the rubidium clock using successively the clock offset solutions estimated with post-mission precise satellite orbits and clock corrections, and the broadcast satellite orbits and clock corrections respectively. The 430 nanoseconds bias of the reference clock, which is used to produce precise satellite clock corrections at the Algonquin ACS reference station with respect to GPS time is removed in Figure 4.1 (Héroux, 1997).

The clock offset solution with the post-mission information basically describes the characteristics of the rubidium clock with an accuracy of two metres (7 nanoseconds). It is nearly a straight line with a slow drift. In real-time, however, only the clock offset solution with broadcast information and C/A code is available for the users without encryption help needed to remove SA. This solution, degraded mainly by the SA, wanders around the real clock offset. The effect of SA on the clock offset estimate is much similar to mixing of interference, which consists of higher frequency components, with the slowly drifting clock offset. In other words, the clock offset measurements made from GPS contains the

interference with higher frequency components. Since SA is an intentional manipulation of both the navigation message orbit data and the satellite clock frequency, its effect on height estimate, the height error sequence, has been observed to make the mean height estimate error approach zero over a long enough period of time. We have proven that the clock offset error is almost linearly correlated to the height error. The mean of the clock offset error made from GPS, therefore, approaches zero, i.e., the mean of the clock offset estimates made from GPS is approximately the real clock offset.

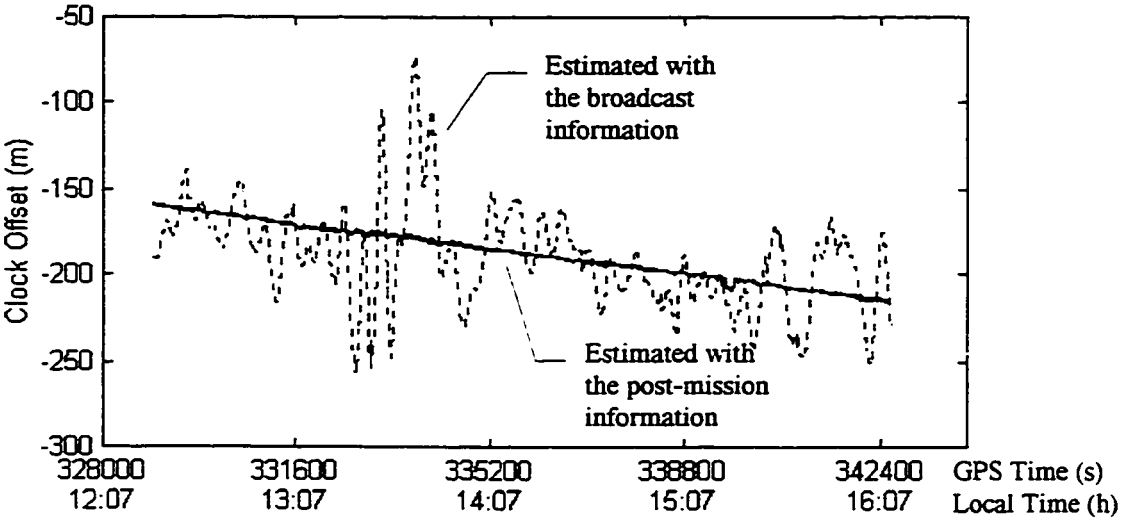

Figure 4.1 Rubidium clock offset solutions estimated with the post-mission information and broadcast information, respectively

In order to estimate and predict the clock offset from GPS measurements, the problem becomes how to estimate the mean of the measurements from the noisy signals. One of the practical and efficient solutions is to use a low-pass filter (LPF). A first-order low-pass filter, shown in Figure 4.2, is a practical scheme to obtain the mean of a signal. Given a proper cut-off frequency ($f_c = \frac{1}{\tau}$), the LPF will cut off all the components of the input signal with the frequency higher than the cut-off frequency, and output the direct component of the signal, i.e., the mean of the signal. The discrete digital formula for this LPF is (Damper, 1995)

$$Y_{k-1} = \frac{X_{k-1}}{\tau} + \left(1 - \frac{1}{\tau}\right) \cdot Y_k \qquad (4.1)$$

where X_k is the value of the input signal at the time of t_k,

Y_k is the value of the LPF output at the time of t_k,

τ is the time constant of the LPF.

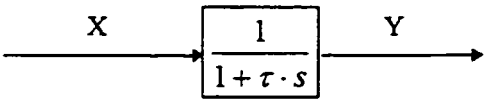

Figure 4.2 Block diagram of first-order Low-pass Filter

The time constant τ of the LPF gives the cut-off frequency. Noting that the average period of the alternating components is around 500 seconds, we set the time constant τ at 1200 seconds. At the first epoch (k=0), $Y_0 = X_0$. It will take 3 τ (3600 seconds) for

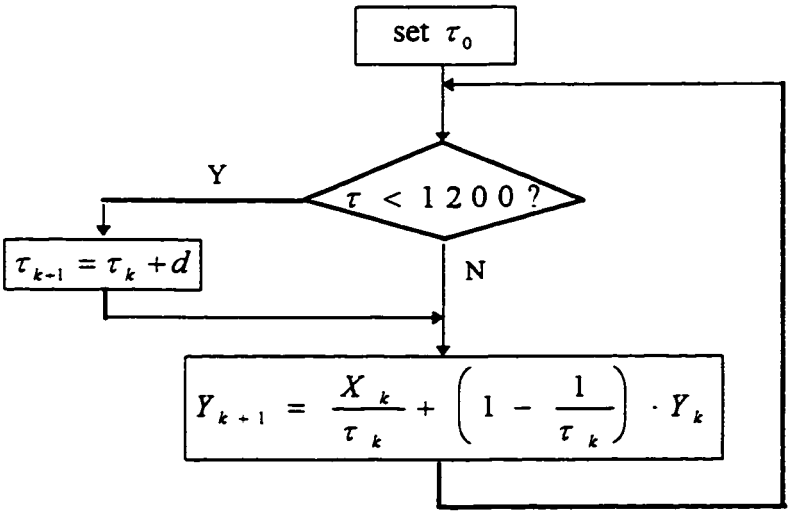

Figure 4.3 Flow chart of the algorithm for the adaptive LPF

the LPF to reach the mean of the input signal. To adapt the LPF to the mean of the input signal faster, an adaptive time constant LPF is implemented. The algorithm of the adaptive LPF is shown in Figure 4.3. At start, a small initial value τ_0 is given to the time constant, then the time constant τ is increased by a step of d at every epoch, until τ = 1200 when the time constant is held fixed.

Figure 4.4 presents the clock offset estimated by the LPF from the GPS measurements. It takes approximately 2000 seconds for the LPF to yield an estimation error less than 10% of the GPS measurement error. Figure 4.5 presents the clock offset estimated by the adaptive LPF from the GPS measurements. It takes 900 seconds for the adaptive LPF to yield an estimation error less than 10% of GPS measurements. The adaptive LPF is more effective than the LPF to reach the mean of the GPS measurements.

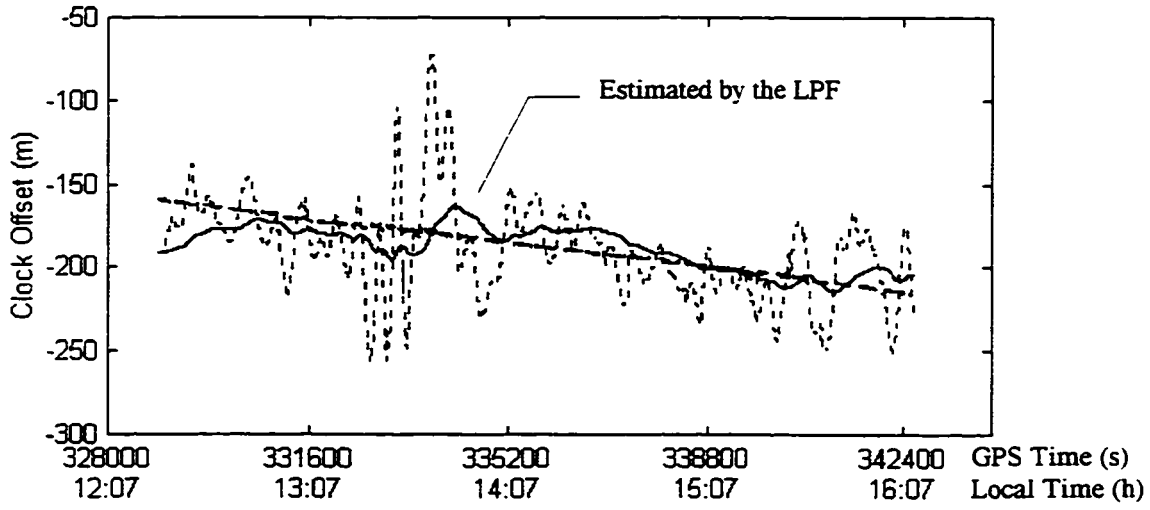

Figure 4.4 Clock offset estimated by the LPF from the GPS measurements

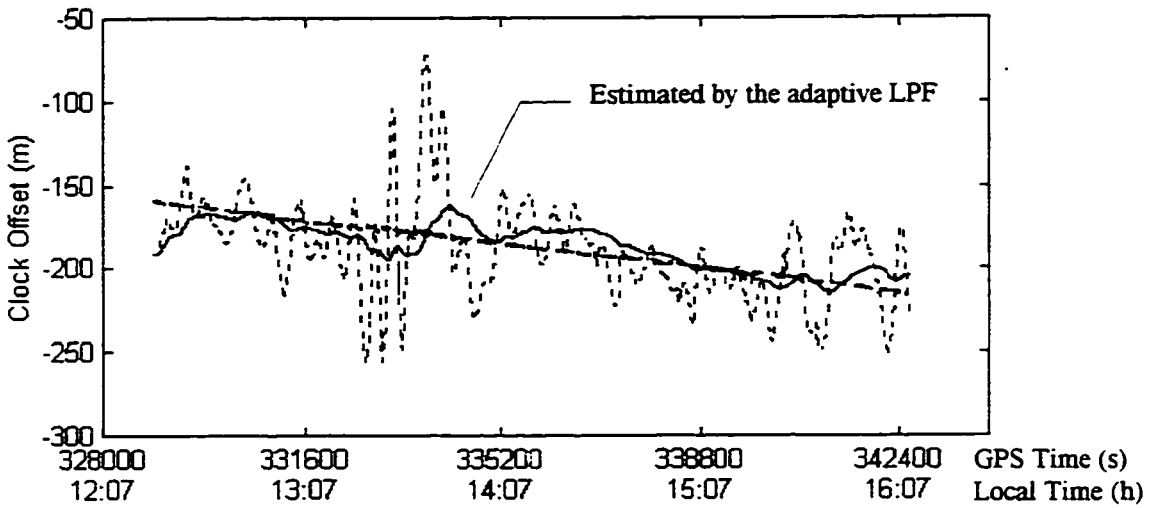

Figure 4.5 Clock offset estimated by the adaptive LPF from the GPS measurements

4.2 Rubidium Clock Modeling for Differential GPS (DGPS)

The adaptive LPF is an efficient means to estimate the clock offset from GPS measurements in stand-alone mode. This method can be directly used in differential mode, but the implementation is more complicated.

4.2.1 Procedure of Differential GPS (DGPS)

DGPS requires a reference station at a known location that receives the same GPS signals as does the remote user. This reference station processes its GPS measurements, calculating pseudorange and pseudorange rate errors with respect to its precisely known location, and then transmits these corrections to remote users in the area. The remote users then apply these corrections to their measurements thus canceling all common errors.

C^3NAV^{TM}, developed at the University of Calgary (Cannon et al., 1995), is a typical GPS navigation software which is able to process data using between receiver single difference, carrier phase smoothed code measurements. In C^3NAV^{TM}, the procedure to generate the corrections to pseudorange measurements is illustrated in Figure 4.6.

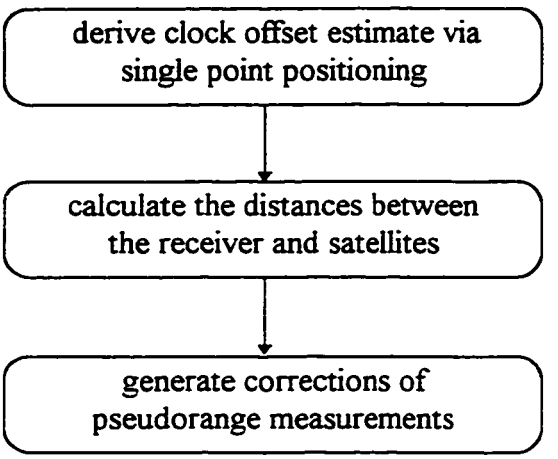

Figure 4.6 Generation of pseudorange corrections with C^{3}NAV^{TM}

At each epoch the clock offset is estimated via single point positioning estimation. Then, the distances between the receiver and all satellites in view are calculated. Finally, the corrections to the pseudorange measurements are generated with the following formula:

$$C^j = d^j_{ref} - p^j_{ref} + cT_{rx}, \tag{4.2}$$

where C^j is the correction to the pseudorange measurement for satellite j,

d^j_{ref} is distance between the receiver and satellite j,

p^j_{ref} is a pseudorange measurement at the reference station for satellite j,

T_{rx} is the clock offset estimate via single point positioning estimation,

c is speed of light,

$j = 1, 2, \ldots, n$,

where n is the number of all satellites in view.

At the remote station, the corrections generated by the reference station are applied to the pseudorange measurements

$$P^j = p^j_{rmt} + C^j, \tag{4.3}$$

where P^j is the corrected pseudorange measurement for the satellite j,

p^j_{rmt} is the pseudorange measurement at the remote station for the satellite j.

With the corrected pseudorange measurements, the remote user's coordinates and clock offset can be estimated via least squares.

4.2.2 Remote User's Clock Offset Estimate

The coordinates of the receiver at the reference station are precisely known in WGS84. Therefore, the clock offset T_{rx} can be estimated by either normal single point positioning estimation (4-D estimation), or single parameter estimation with fixed coordinates (1-D estimation). One may write the clock offset estimate as

$$T_{rx} = t - dt, \tag{4.4}$$

where t is real clock offset, dt is the clock offset estimation error, and the corrections to the pseudorange measurements as

$$C^j = d^j_{ref} - p^j_{ref} + ct + cdt. \tag{4.5}$$

At the remote station, the corrections generated by the reference station are applied to correct the pseudorange measurements

$$P^j = p^j_{rmt} + C^j = p^j_{rmt} + d^j_{ref} - p^j_{ref} + ct + cdt. \tag{4.6}$$

In the following, the corrections with the clock offset estimate via 4-D estimation will be referred to as 4-D estimation corrections, and the corrections with the clock offset estimate via 1-D estimation will be referred to as 1-D estimation corrections. It is obvious that the clock offset estimation error dt using 1-D estimation will not be the same as that using 4-D estimation.

The linearized navigation equations Eq. (2.1) may be written as

$$\mathbf{Y} = \mathbf{H}_l \mathbf{X}_l - c\Delta T, \tag{4.7}$$

where $\mathbf{X}_l = \begin{bmatrix} \Delta x & \Delta y & \Delta z \end{bmatrix}^T$

$$\mathbf{H}_i = \begin{bmatrix} \alpha_{1x} & \alpha_{1y} & \alpha_{1z} \\ \alpha_{2x} & \alpha_{2y} & \alpha_{2z} \\ \cdots\cdots & \cdots\cdots & \cdots\cdots \\ \alpha_{nx} & \alpha_{ny} & \alpha_{nz} \end{bmatrix}$$

= directional cosine matrix of the estimated line of site(LOS).

ΔT = difference between the initial clock offset and the estimated clock offset.

Assume that the reference station time is synchronized to GPS time, that is, the clock offset estimation error dt in Eq. (4.4) is 0. The corrections to the pseudorange measurements become:

$$C_0^j = d_{ref}^j - p_{ref}^j + ct \tag{4.8}$$

and the corrected pseudorange measurements are

$$P_0^j = p_{rmt}^j + d_{ref}^j - p_{ref}^j + ct\,. \tag{4.9}$$

With the above corrected pseudorange measurements, the solution for $\left[x_0 \;\; y_0 \;\; z_0 \;\; T_0\right]^T$ can be derived from Eq.(4.7). The accuracy of this solution depends upon the DOP and the variances of the corrected pseudorange measurements.

In practice, it is very difficult to synchronize the reference station's time to GPS time. The clock offset of the receiver located at the reference station is usually estimated via 1-D or 4-D single point positioning estimation, that is, via Eq.(4.4) with $dt \neq 0$.

From Eq.(4.4) we note that all the corrections for the satellites in view have the same clock offset estimation error at each epoch. The pseudorange measurement corrections for SV j are

$$C^j = d_{ref}^j - p_{ref}^j + ct + cdt = C_0^j + cdt \tag{4.10}$$

where C_0^j is pseudorange measurement corrections for the satellite j when $dt = 0$. The corresponding corrected pseudorange measurement is

$$P^j = p^j_{rmt} + d^j_{ref} - p^j_{ref} + ct + cdt = P^j_0 + cdt\,, \tag{4.11}$$

where P^j_0 is corrected pseudorange measurement for the satellite j when $dt = 0$.

It is straightforward to conclude from Eq. (4.7) that if the solution $\begin{bmatrix} x_0 & y_0 & z_0 & T_0 \end{bmatrix}^T$ satisfies that equation with P^j_0, the solution $\begin{bmatrix} x_0 & y_0 & z_0 & T_0 - dt \end{bmatrix}^T$ will also satisfy the equation with $P^j_0 + cdt$. In other words, the remote user's clock offset estimate entirely absorbs the clock offset estimation error produced at the reference station. Therefore, the remote user's position accuracy is the same with either 1-D estimation corrections or 4-D estimation corrections, while the 1-D clock offset estimation error is not equal to that of 4-D estimation.

The remote user's clock offset solution is now with respect to the clock offset at the reference station, which is referred to as time base. Depending upon how the clock offset solution is derived at the reference station, the effective time base will vary with respect to GPS time.

The remote user's clock offset estimation error is made up of two parts: the estimation error with respect to the time base of the reference station and the time base error with respect to GPS time. The first part of the clock offset estimation error is at the same level as the position error of DGPS. This is the case when the reference station's time is synchronized to GPS time. The remote user's clock offset estimation error depends upon the TDOP and the variances of corrected pseudorange measurements. The second part of the clock offset estimation error depends upon how the time solution at the reference station is derived, namely via 1-D or 4-D estimation, and the level of SA.

The clock offset estimation error using the 4-D method, or normal single point positioning estimation, is caused directly by the errors of pseudorange measurements, which result from Selective Availability errors, ionospheric delays, tropospheric delays, ephemeris

errors and satellite clock errors etc. In 1-D estimation, however, a clock offset solution is maintained at the reference station that drives the average of the corrections of all satellite in view to zero, under the assumption that the means of all errors are zero. The errors of pseudorange measurements are averaged. It is obvious that the clock offset estimate via 1-D estimation is better than that via 4-D estimation, assuming that the WGS84 coordinates are precisely known.

Figure 4.7 through Figure 4.9 demonstrate the relationship between the clock offset solution at the reference station and that at the remote station. All the data were collected during the static test described in Chapter 2. Figure 4.7 presents the clock offset estimate (time base) at the reference station via 1-D estimation using broadcast information. The receiver clock at the reference station is a cesium clock which is more stable than the rubidium clock. The time base in Figure 4.7 is relatively noisy due to the effect of SA over a period of four hours. Figure 4.8 shows the clock offset solution estimated at the remote station using differential corrections, which is generated using the time base as shown in Figure 4.7. This solution is with respect to the time base. Figure 4.9 presents the difference between the clock offset solution at the remote station and the time base at the reference station. This difference is similar to the clock offset estimate using post-mission information (see Figure 4.5) which basically reflects the remote receiver clock's actual drift with respect to GPS time. There is, however, an 80 metres bias between the two estimates because the time base wanders around -80 metres. It is reasonable to believe that the real clock offset is smoother than the curve shown in Figure 4.9 which include a clock offset error. This clock offset error results from the residual effect of SA, difference of ionosphere and troposphere etc., and only this error is correlated to the position errors as analyzed in Chapter 2. As will be shown later, the cesium and rubidium clocks have similar linear drift characteristics over the time interval tested.

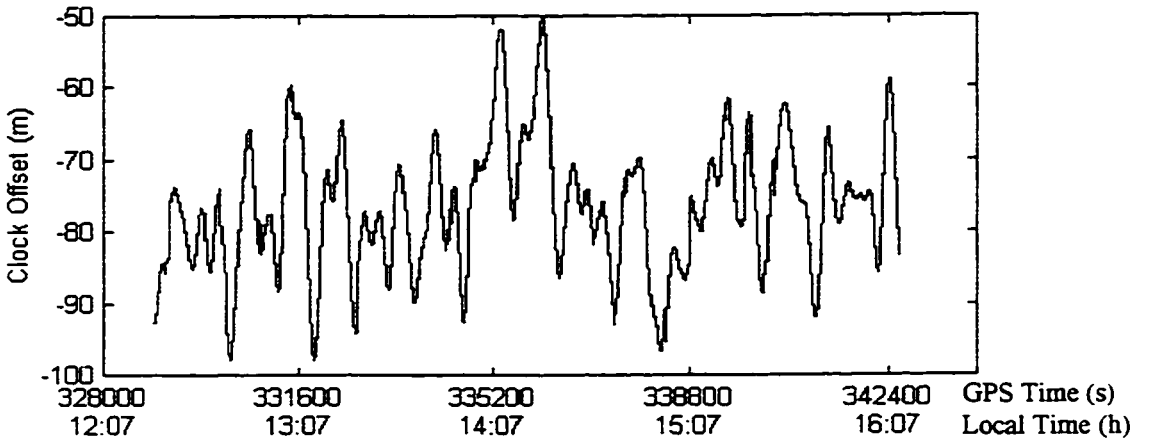

Figure 4.7 Time base estimated via 1-D estimation at a reference station equipped with a cesium clock

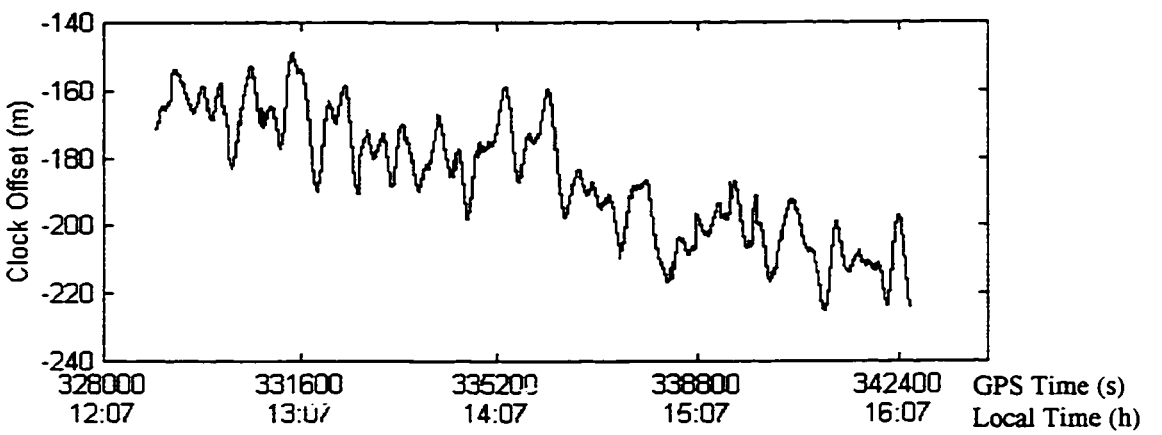

Figure 4.8 Rubdium Clock offset solution at the remote station using differential corrections

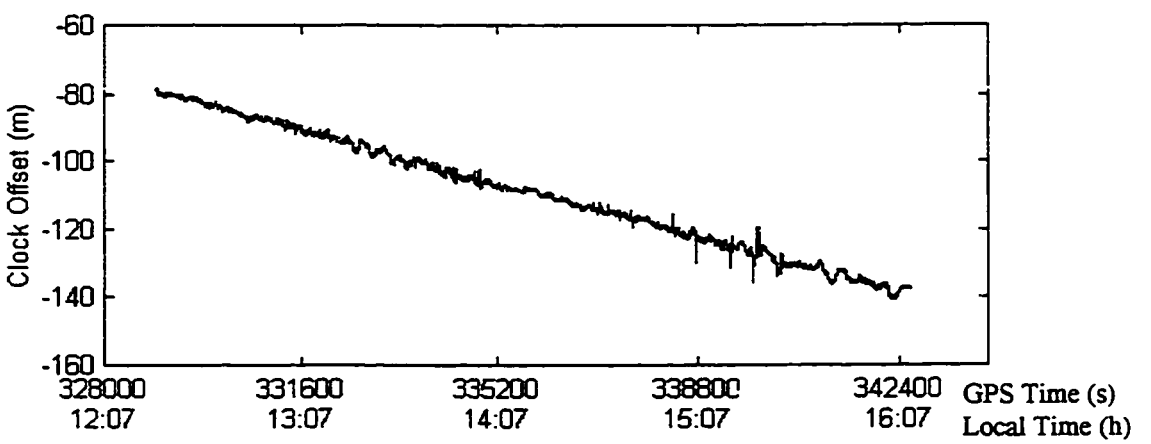

Figure 4.9 Difference between the remote clock offset solution and the time base

4.2.3 Considerations on the clock at the reference station

In order to apply the adaptive filter to DGPS, it is necessary to separate the remote clock offset estimation error with respect to the time base from the time base error with respect to GPS time. If the time base is estimated via 1-D or 4-D estimation using broadcast information, the time base estimation error is quasi-random since SA is quasi-random over a sufficiently long period of time. It is difficult to predict the time base error.

When very stable clocks, such as cesium or rubidium clocks, are used at both the reference and remote station, the time base can be simply fixed, i.e. substitute T_{rx} in equation (4.2) with a constant. At the remote station, the linearly changing component of the clock offset solution is the effect of the drifts of both the clock at the reference station and the clock at the remote station, and the high frequency component is the clock offset estimation error with respect to the time base. The two errors can be separated by a low-pass filter. Figure 4.10 presents the clock offset solution at the remote station using differential corrections with the time base fixed (T_{rx} was fixed at -80 metre) at the reference station. Figure 4.11 shows the clock offset estimated by the adaptive LPF from the GPS measurements. In the next section, it will be shown that the filtered clock offset from the GPS measurements in differential mode is more accurate than direct computation using GPS measurements.

When a less stable clock, such as TCXO, is used at the reference station, the clock drifts rapidly and in a non-linear manner. The time base at the reference can not be fixed. If the receiver at the reference station could access the Y code or precise satellite orbits and clock corrections, the time base could be estimated with an accuracy of better than 10 nanoseconds at each epoch. Figure 4.12 shows this is possible by presenting the time base estimated with post-mission precise satellite orbits and clock corrections. Generated with the precise time base, the pseudorange corrections are applied to solve the clock offset at the remote station as shown in Figure 4.13. The adaptive LPF can still be applied to reduce receiver and atmospheric noise. The data used in Figure 4.14 and 4.15 were collected at Nose Hill Park, Calgary. The test will be described in detail in Chapter 6

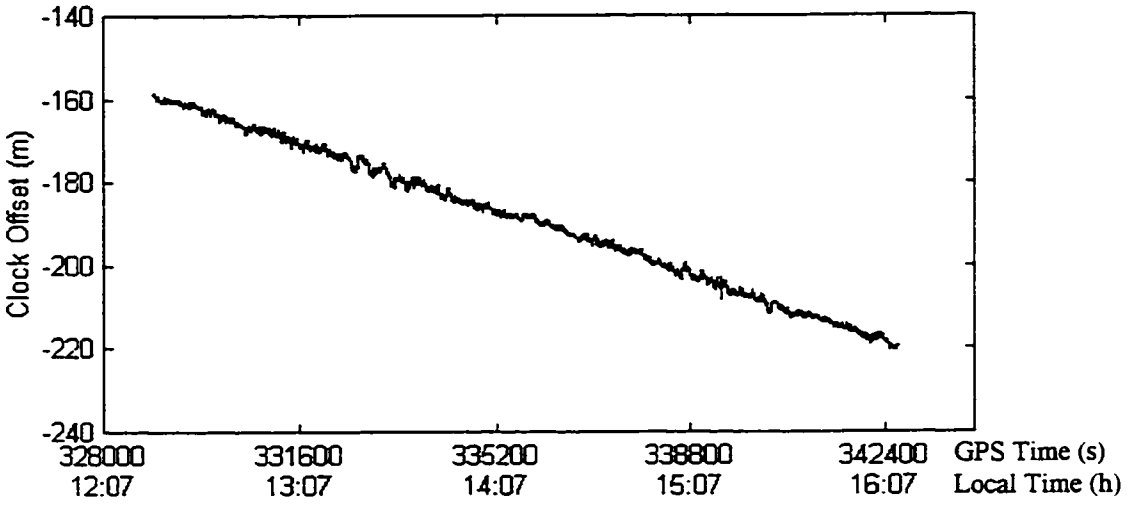

Figure 4.10 Rubidium clock offset solution at the remote station using the differential corrections with the fixed time base at the reference station with a cesium clock

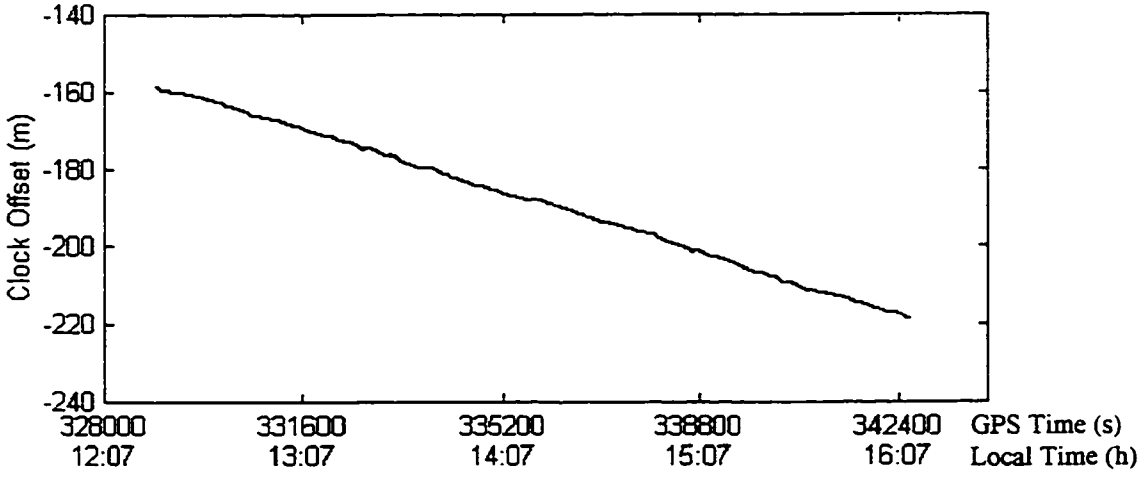

Figure 4.11 Clock offset estimated by the adaptive LPF from GPS measurements in differential mode

and referred to as the Nose Hill test. A TCXO clock at the reference station and a rubidium clock at the remote station were used. The TCXO clock is that used internally in the NovAtel 951R receiver. Figure 4.14 presents the clock offset solution at the remote station with differential corrections using the time base calculated with broadcast information by 1-D estimation. The remote clock offset changes rapidly because the effect

of SA enters into the time base estimation and in turn affects the remote solution. Figure 4.15 depicts the remote clock offset solution with differential corrections using the time base with post-mission precise satellite orbits and clock corrections by 4-D estimation. The remote clock offset becomes smooth and the adaptive LPF can be applied. If SA was off, the use of a TCXO clock with broadcast ephemeris at the reference station would be sufficient.

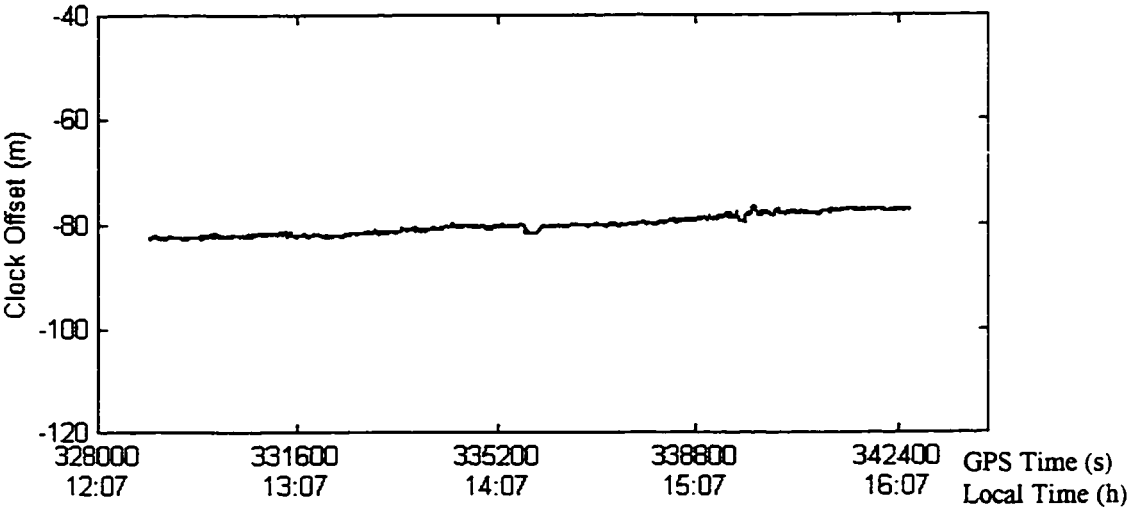

Figure 4.12 Cesium time base estimated with post-mission precise satellite orbits and clock corrections at the reference station

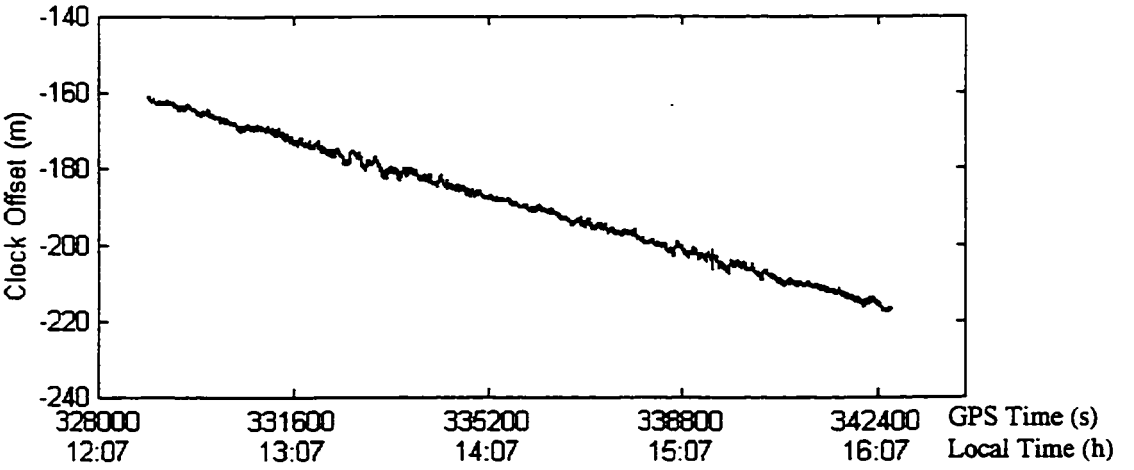

Figure 4.13 Rubidium clock offset solution at the remote station using the differential corrections generated with the reference station cesium time base estimated with post-mission information

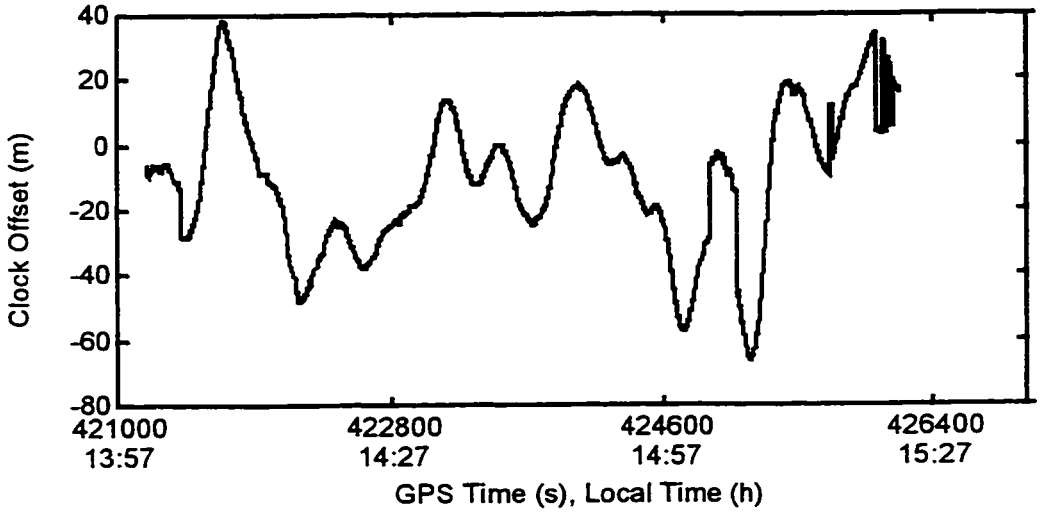

Figure 4.14 Rubidium clock offset estimate at remote with differential corrections using a reference station TCXO time base solved by 1-D estimation with broadcast information

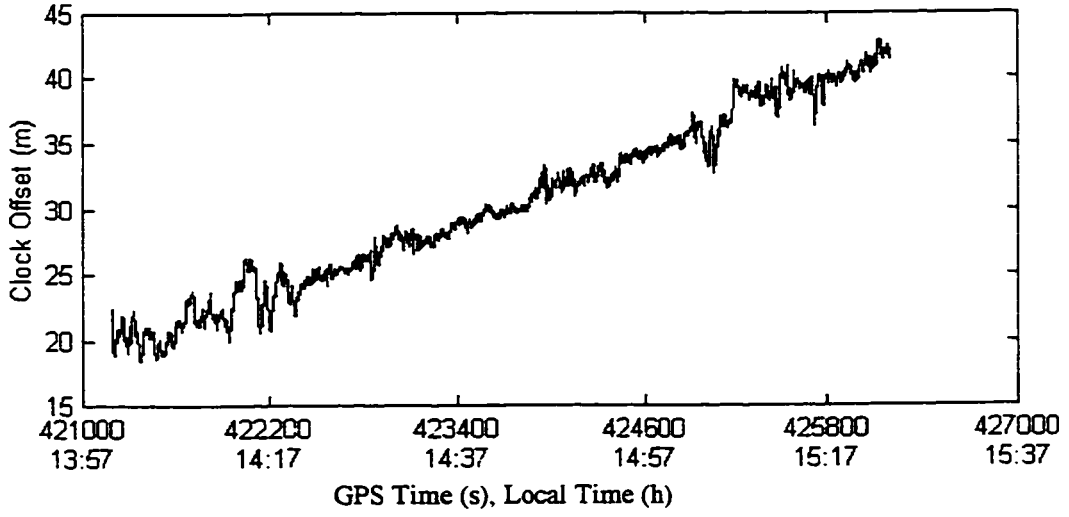

Figure 4.15 Rubidium clock offset solution at remote with differential corrections using a reference station use TCXO time base solved by 4-D estimation with post-mission information

4.3 Navigation Algorithm Design for Rubidium Clock Aided GPS

Usually, the GPS navigation algorithm used to estimate point solutions is either a least squares or Kalman filtering algorithm. This section will discuss the least squares method and leave the Kalman filtering algorithm to Chapter 5.

4.3.1 Rubidium clock constrained GPS

In the case of rubidium clock constrained GPS navigation, the clock offset information, which is estimated from the GPS measurements, is used to constrain the position estimate. A mathematical model of the GPS range measurement is given by [Lachapelle, 1995]:

$$p = \rho + d\rho + c(dt - dT_m) + d_{ion} + d_{trop} + \varepsilon_p \tag{4.12}$$

where p is range measurement

ρ is the real range between the satellite and the receiver

$d\rho$ is the range error induced by orbital error

dt is the satellite clock error

dT_m is the receiver clock offset

d_{ion} is the ionospheric delay

d_{trop} is the troposhperic delay

ε_p is receiver noise and multipath.

For the clock offset measurement, the mathematical model may be written as:

$$dT_m = dT + \varepsilon_T \tag{4.13}$$

where dT_m is the receiver clock offset measurement

dT is the real receiver clock offset measurement

ε_T is the receiver clock offset measurement error

Given the design matrix A, the covariance matrix of measurements $\mathbf{C}_l$, the *a priori* position estimate vector $\mathbf{x}^0$ and the misclosure vector $\mathbf{w}^0$, a solution vector $\hat{\mathbf{x}}$ may be obtained by the following equations (Krakiwsky, 1990):

$$\mathbf{w}^0 = f(\mathbf{x}^0, \mathbf{l}) \tag{4.14}$$

$$\mathbf{d} = -[\mathbf{A}^T\mathbf{C}_l^{-1}\mathbf{A}]^{-1}\mathbf{A}^T\mathbf{C}_l^{-1}\mathbf{w}^0 \tag{4.15}$$

$$\hat{\mathbf{x}} = \mathbf{x}^0 + \mathbf{d} \tag{4.16}$$

where $\mathbf{l}$ is the observation vector and

$\mathbf{d}$ is the least squares adjustment to parameters $\mathbf{x}^0$.

The design matrix A may be obtained by linearizing the equations with respect to the geodetic coordinates and the receiver clock offset. For a GPS range measurement,

$$\mathbf{A}_i = \begin{bmatrix} \frac{\partial p_i}{\partial \phi} & \frac{\partial p_i}{\partial \lambda} & \frac{\partial p_i}{\partial h} & -1 \end{bmatrix}$$

where ϕ is latitude,

λ is longitude,

h is height,

and for the receiver clock offset measurement, the design matrix is

$$\mathbf{A}_T = \begin{bmatrix} 0 & 0 & 0 & -1 \end{bmatrix}. \tag{4.17}$$

The constraint weight matrix $\mathbf{C}_l^{-1}$ is defined as:

$$\mathbf{C}_l^{-1} = \begin{bmatrix} \sigma_1^2 & 0 & \cdots & 0 & 0 \\ 0 & \sigma_2^2 & \cdots & 0 & 0 \\ \vdots & \vdots & \ddots & \vdots & \vdots \\ 0 & 0 & \cdots & \sigma_n^2 & 0 \\ 0 & 0 & \cdots & 0 & \sigma_T^2 \end{bmatrix},$$

where σ_i^2 is the GPS range error variance for the i-th satellite $i = 1, \cdots, n$,

σ_T^2 is the receiver clock offset measurement error variance.

Figure 4.16 presents a basic navigation algorithm for rubidium clock aided GPS. The algorithm estimates three coordinates and the receiver clock offset by standard least squares, then filters the clock offset estimated from GPS measurements using the adaptive low-pass filter. Finally, the algorithm employs the clock constraint in the least squares solution. In terms of processing time, this is not a efficient algorithm, since the least squares solution must be calculated twice.

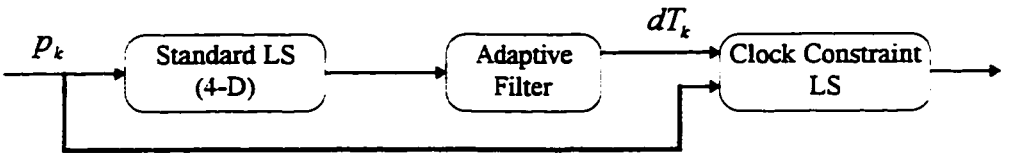

Figure 4.16 Basic navigation algorithm for rubidium clock aided GPS

Since the rubidium clock drifts very slowly, an alternative navigation algorithm was designed by the author for rubidium clock constrained GPS. Figure 4.17 shows this improved navigation algorithm. The least squares estimator takes the GPS range measurements and the filtered clock offset from the last epoch. The two algorithms have the same accuracy, but the improved algorithm is faster than the basic navigation algorithm.

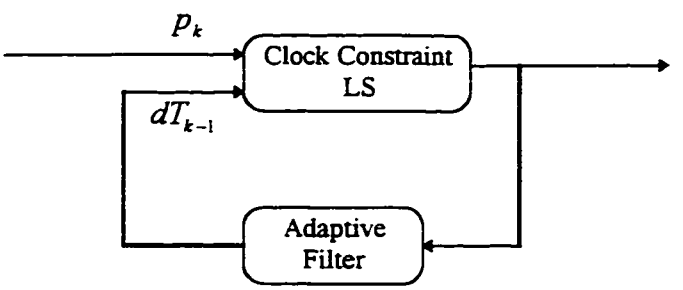

Figure 4.17 Improved navigation algorithm for rubidium clock aided GPS

4.3.2 Single point solution example

The GPS navigation program C^{3}NAV™ was modified to implement the navigation algorithm for rubidium clock aided GPS. The data used herein were collected in the static test described in Chapter 2. All the point results were computed using a satellite cutoff angle of five degrees and a processing interval of 1 second. Carrier phase smoothing of the pseudorange measurements was performed and troposhperic corrections were employed.

Figure 4.18 presents the position errors of unaided GPS which were computed by C^{3}NAV™ in stand-alone mode. Typical SA positioning errors of 100 metres in horizontal

and 150 meters in vertical occur. It is noted that the position accuracy was degraded severely during GPS time of 331529 to 334260 seconds, when the satellite geometry was relatively poor (please refer to Figure 2.1 through 2.5).

Figure 4.19 presents the position errors of rubidium clock aided GPS, which were computed by the modified navigation program implementing the navigation algorithm shown in Figure 4.17, in stand-alone mode. The position accuracy, especially the vertical accuracy, is improved significantly. Table 4.1 summarizes the results of the static test.

The height accuracy was improved the most by clock aiding, since the height error was most correlated to the clock offset error during the test. The longitude accuracy was improved the least significantly, since the longitude error was least correlated to the clock offset error during the test.

Table 4.1 Statistics for the results of the static test (entire test)

MEAN/RMS (m)

	LATITUDE	LONGITUDE	HEIGHT
unaided GPS	6.82/27.48	1.90/15.06	6.13/41.83
clock aided GPS	5.84/20.65	0.29/14.15	9.04/21.82

It is interesting to observe the relationship among the correlation coefficients, the satellite geometry and improvement in position accuracy. During GPS time 331529 to 334260 seconds, the satellite geometry is poorer. Table 2 summarizes the results during this period.

Table 4.2 Statistics for the results of the static test during 331529 to 334260 seconds

MEAN/RMS (m)

	LATITUDE	LONGITUDE	HEIGHT
unaided GPS	-0.88/42 59	-2.28/17.18	9.79/68.79
clock aided GPS	-7.37/21.62	-3.33/17.17	1.77/20.11

Both the height and latitude accuracies are increased significantly since the height and latitude errors are strongly correlated to the clock offset error during this period. The

longitude accuracy is not improved at all since the longitude error is independent of the clock offset error in this case.

4.3.3 DGPS solution example

Figure 4.20 presents the position errors of unaided GPS, which were computed by C^3NAV^{TM}, in differential mode. The accuracy of DGPS increases significantly over stand-alone GPS since the common errors, such as SA errors, ionospheric delays, tropospheric delays, ephemeris errors and satellite clock errors etc., are eliminated.

Figure 4.21 shows the remote position errors of rubidium clock aided GPS in differential mode. The differential corrections were generated by using a fixed time base fixed (-80 metres) at the reference station which was equipped with a cesium clock. The point-to-point remote station results were computed by the modified navigation program which implements the navigation algorithm as shown in Figure 4.17. Table 4.3 summarizes the results in differential mode. While there are improvements in position accuracy, they are not as significant as in stand-alone mode because the satellite geometry is relatively good in this case. Under degraded geometry, the improvement is significant, however, as will be shown in subsequent chapters.

Table 4.3 Statistics for the results of the static test

MEAN/RMS (m)

	LATITUDE	LONGITUDE	HEIGHT
4-D Estimation	-0.07/0.67	-0.31/0.54	0.42/1.30
3-D Estimation	-0.03/0.63	-0.29/0.45	0.47/0.99

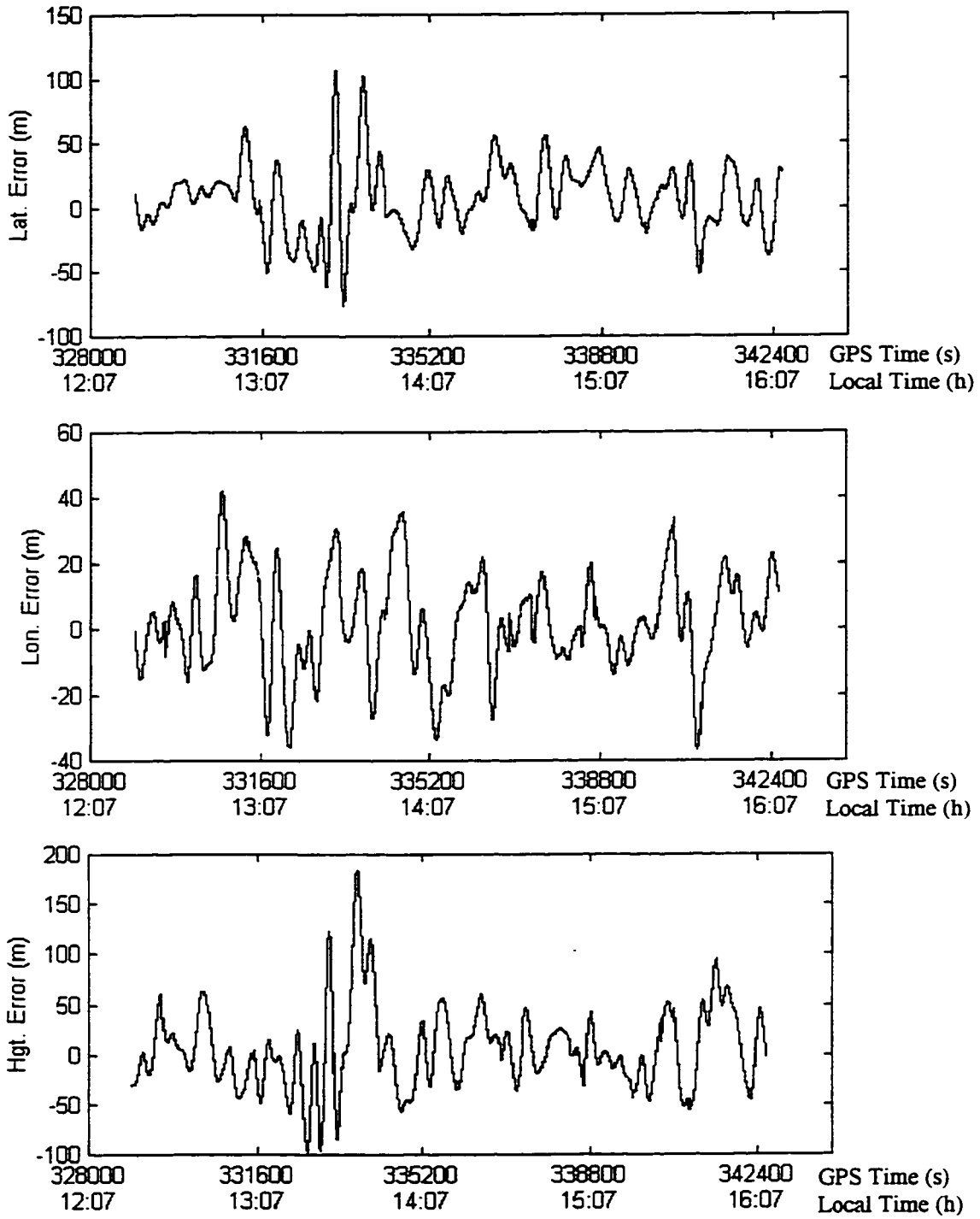

Figure 4.18 Position errors of unaided GPS in stand-alone mode

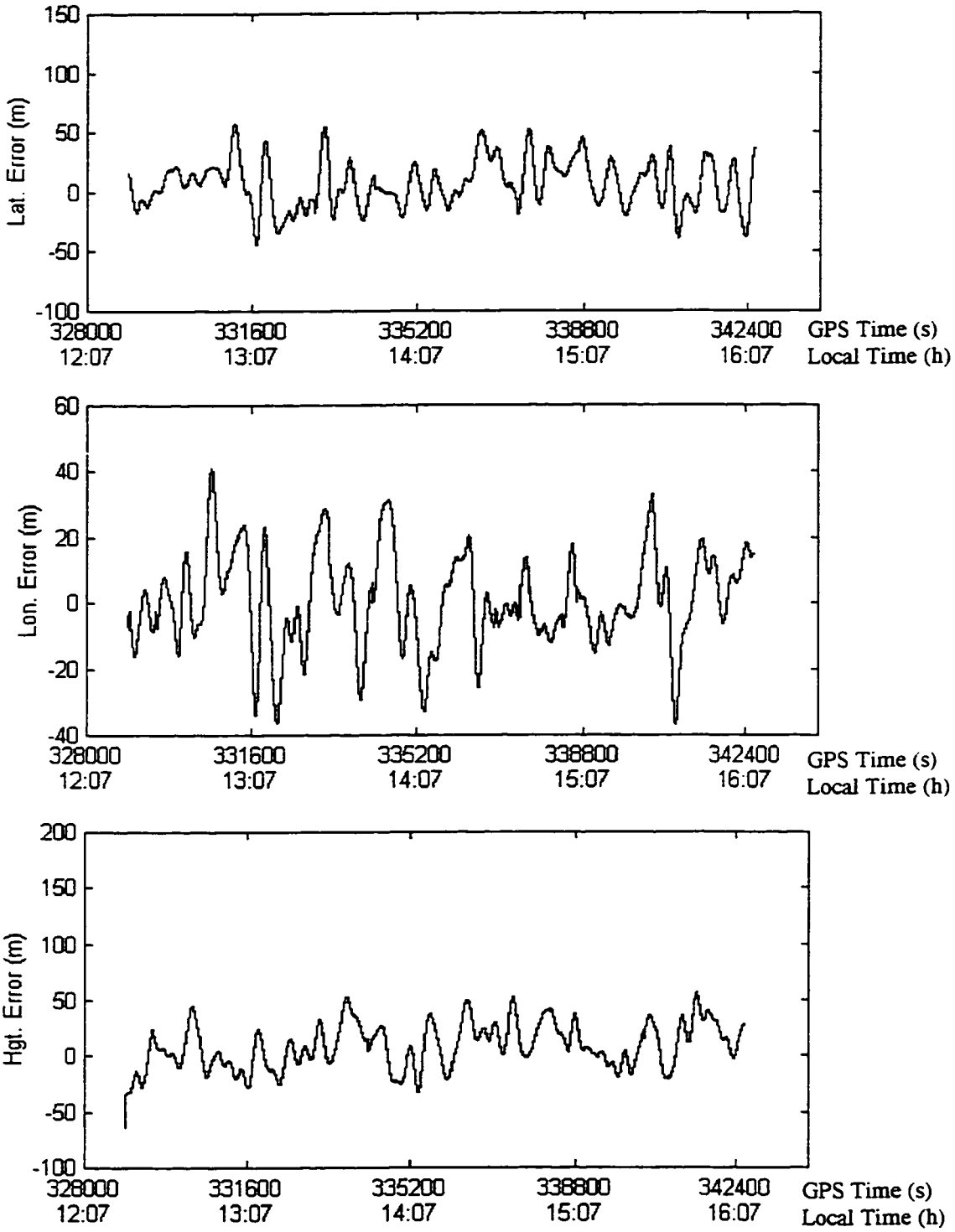

Figure 4.19 Position errors of rubidium clock aided GPS in stand-alone mode

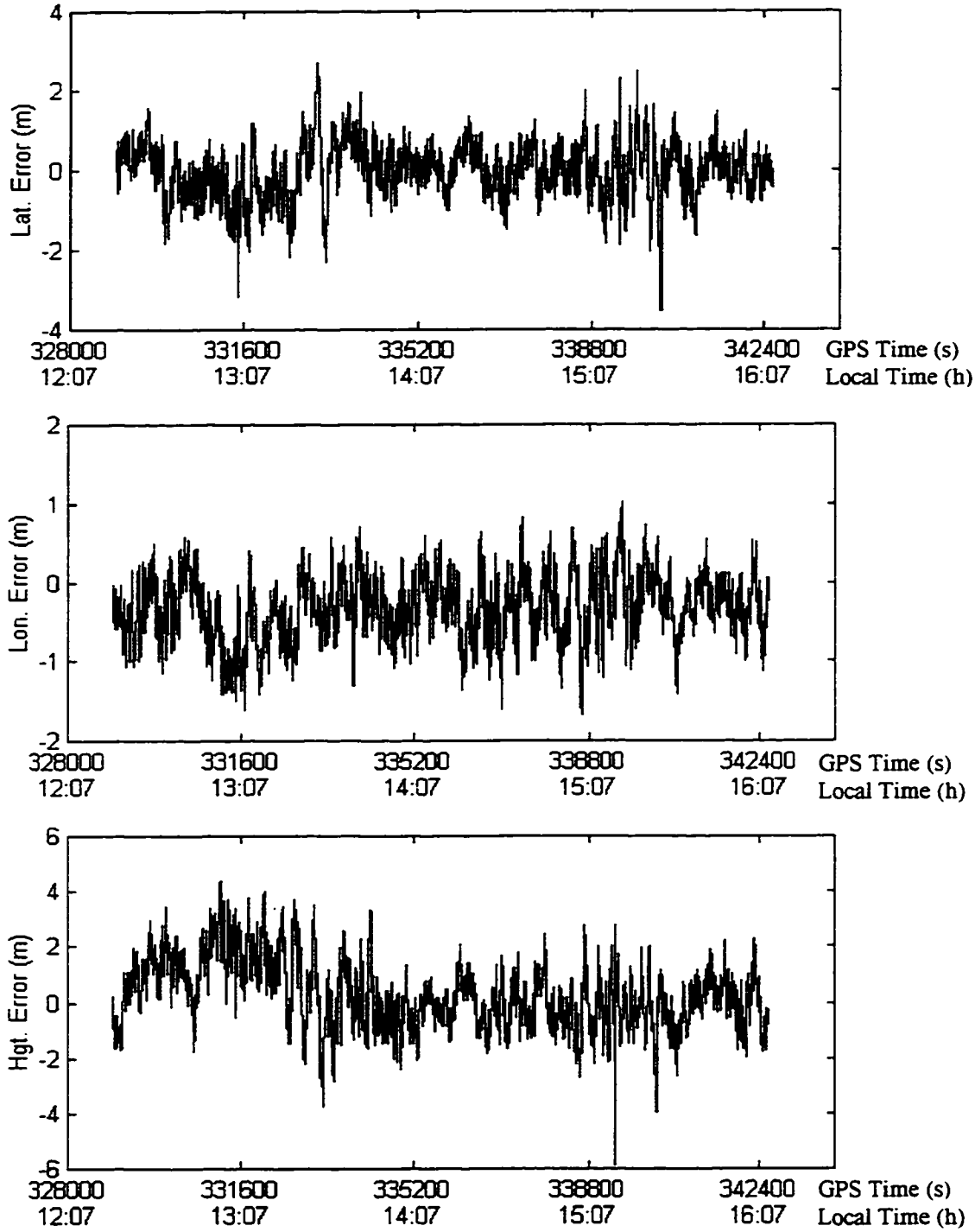

Figure 4.20 Position errors of unaided GPS in differential mode

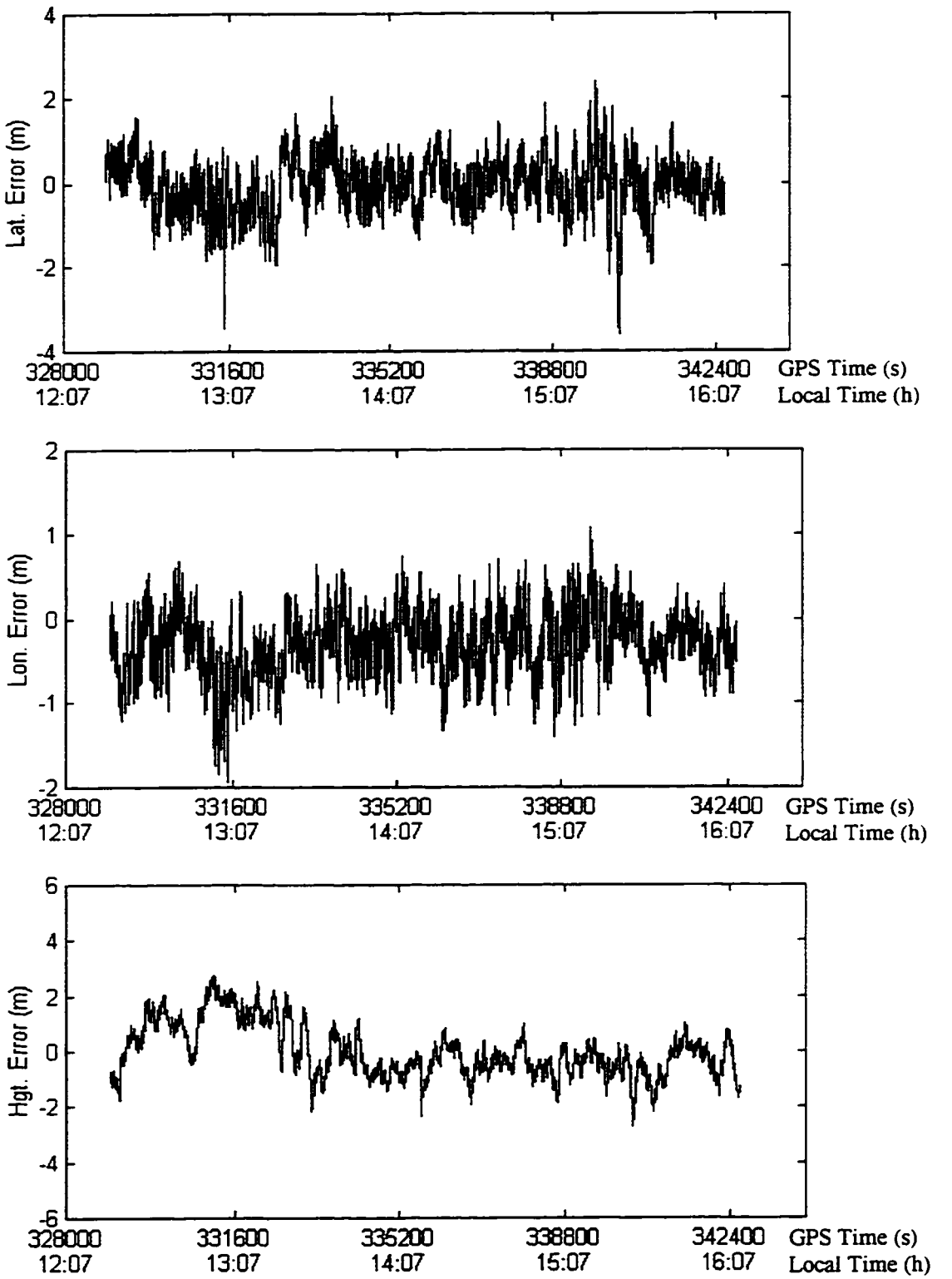

Figure 4.21 Position errors of rubidium clock aided GPS in differential mode

CHAPTER 5
RUBIDIUM CLOCK AIDED GPS/BAROMETER/GYRO INTEGRATED NAVIGATION SYSTEM

Augmentation of GPS with a barometer and a heading rate gyroscope improves positioning availability significantly (Hayashi, 1996a & b). Integration of rubidium clock aided GPS with a barometer and a gyro will be investigated in this chapter.

5.1 System Hardware Overview

The integrated navigation system developed herein consists of a NovAtel GPSCard 951R L1 GPS receiver, an Efratom Model FRK-LLN Rubidium clock, a Silicon Valley GPS Reference Frequency Generator, a Viatran Model 246 barometric pressure transducer, an Andrew AutoGYRO digital fiber optic gyro, an Advantech PCL-711 12-bit data acquisition board and PC, as shown in Figure 5.1. Another GPSCard is used as the reference station to generate differential corrections. The reference station may also include an external clock to improve timing accuracy.

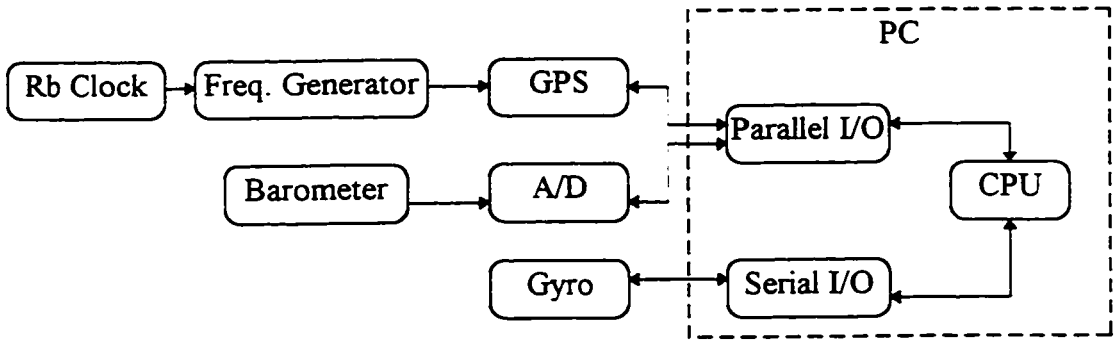

Figure 5.1 On board hardware overview - integrated navigation system

The GPS receiver, the GPS reference frequency generator and the Advantech PCL-711 12-bit data acquisition board are all PC compatible circuit boards, and installed in the expansion slots of the PC.

The Viatran Model 246 barometric pressure transducer senses an ambient barometric pressure and translates it into an output of voltage ranging from zero to five volts. The voltage output is converted into 12-bit digital data by the PCL-711 data acquisition board. Table 5.1 presents the barometer's specification (Viatran 1995). The height difference accuracy achievable will be discussed later.

Table 5.1 Viatran Model 246 Barometer Specifications

Full Scale Pressure Range	25" to 32" Hg absolute (1" = 25.4 mm)
Total Error Band due to Non-linearity, Hysterisis and Repeatability	≤ ± 0.01" Hg
Response Time	≤ ± 5 msec
Zero Repeat after 100°F Temperature Shift	≤ ± 0.007"Hg
Compensated Temperature Range	0°F to +200°F
Operating Temperature Range	-40°F to +250°F
Temperature Effect on Zero	≤ ± 0.0018" Hg per 1°F
Temperature Effect on Span	≤ ± 0.0018" Hg per 1°F
Long-term Stability	≤ ± 0.035" Hg per 6 months
Supply Voltage	8.5 to 40 VDC
Power Supply Regulation	≤ ± 0.000007" Hg per Volt
Output Signal	0 to 5 VDC
Output Signal Noise Levels	≤ 10 mV peak to peak

The Andrew AutoGYRO digital fiber optic gyro is a one-axis gyro mounted vertical to the road surface to sense the vehicle's heading rate. It outputs a digital signal with a RS-232E serial port. The computer can obtain the gyro data directly through the serial port. Table 5.2 gives the gyro's performance (Andrew 1994).

Table 5.2 Performance of Andrew AutoGYRO

Input Rotation Rate	± 100 deg/sec
Minimum Detectable Rotation Rate (in 100 Hz bandwith)	± 0.02 deg/sec (60 deg/hr) angle random walk
Bias Drift (at stabilized temperature)	0.005 deg/sec, rms (18 deg/hr)
Scale Factor Non-linearity	0.25%, rms
Scale Factor Temperature Stability	0.5%, rms
Warm-up Time	1 second
Operating Temperature	-40°C to +75°C
Power	+9 to +18 VDC, 630 mA
Sensor Output	RS-232E, 9600 baud

5.2 System Algorithm Design

The integrated navigation system was designed to be modular and decentralized, as shown in Figure 5.2. The navigation sensors used are the following:

1. GPS pseudorange and Doppler for position and velocity;
2. rate gyro for azimuth change;
3. barometer for height; and
4. rubidium clock for time.

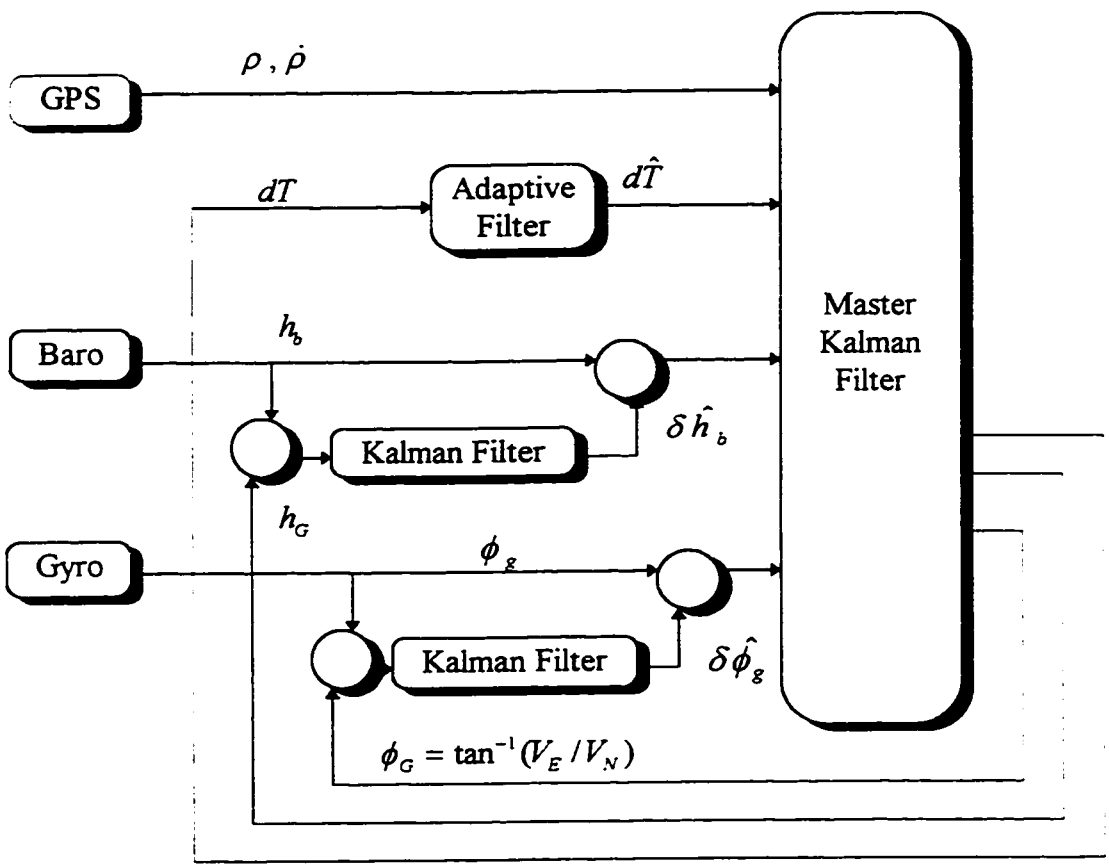

Figure 5.2 Block diagram of the integrated navigation system algorithm

Each sensor has its own filter. The master filter is GPS-based, while each sensor has its own local filter for determining bias and performing fault detection. All local filters feed in the master filter where fusion of all information is made. The master filter then feeds back in the local filters.

The feed back from the master filter to each local filter allow for frequent and automatic calibration of each sensor separately. In this manner, outliers, blunders and spurious data in each sensor can be eliminated and recalibration can take place. Only clean data moves from each local filter into the master filter.

At the beginning of a run, when the number of satellites in view is more than 3 and the satellite geometry as measured by the DOP is good enough (less than 5), the adaptive filter will estimate the clock offset from GPS measurements; the Kalman filter for the barometer will estimate the barometric height error from GPS height measurements; the Kalman filter for the gyro will estimate the gyro heading error from GPS velocity measurements. With GPS pseudorange and instantaneous Doppler measurements, improved clock offset, and height and heading estimates, the master Kalman filter will be capable of better estimation of the position.

When the number of satellites in view falls to three or less, or the satellite geometry becomes poor, the adaptive filter will predict the clock bias and the Kalman filters will predict the barometric height error and gyro heading error. The master Kalman filter can still estimate the position with reasonable accuracy.

5.3 Kalman Filter Design for the Barometer

The Kalman filter for the barometer is a complementary filter (Yu, 1984), which estimates the barometric height error from the measurement differences between the barometric height and the GPS height.

5.3.1 Barometric height

The barometric pressure p measured by the Viatran pressure transducer can be converted into pressure altitude, or barometric height h_b, from the U.S. Standard Atmosphere model (Lutgens & Tarbuck, 1982), i.e.:

$$h_b = a_0 + a_1 p + a_2 p^2 + a_3 p^3 + a_4 p^4 + a_5 p^5 \qquad (5.1)$$

where $a_0 = -1.42463372756486 \times 10^3 \ m$

$a_1 = 3.776791975661281 \times 10 \ m \cdot (kPa)^{-1}$

$a_2 = -6.074065901439399 \times 10^{-1} \ m \cdot (kPa)^{-2}$

$a_3 = 5.643398665717297 \times 10^{-3} \ m \cdot (kPa)^{-3}$

$a_4 = -2.814440431082333 \times 10^{-5} \ m \cdot (kPa)^{-4}$

$a_5 = 5.846393362917872 \times 10^{-8} \ m \cdot (kPa)^{-5}$

The pressure altitude is the height in a model atmosphere above the standard pressure datum plane (sea level) of 760 mm of mercury. It differs from the true altitude (above the standard sea level) in that the pressure altitude does not consider pressure or temperature variations over the surface of the earth due to changing weather pattern and height of the surface above sea level at the starting point.

5.3.2 Barometric height error

In static mode, the primary error for the barometric height is the barometric height bias with respect to the GPS height (above the WGS 84 Ellipsoid). This is due to the height difference between the barometer and the GPS antenna, and pressure or temperature variations. Over a short time period, the height bias is approximately constant. Figure 5.3 shows the barometric height error in static mode, the result of a field test which was conducted on November 27, 1996, at Nose Hill park, Calgary, and will be described in detail in section 6.1 (we will refer to the test as the Nose Hill test). The barometric height bias δh_0, therefore, can be modeled as a random constant, namely

$$\dot{\delta h_0} = 0 \ . \qquad (5.2)$$

In kinematic mode, the barometric height measurement error becomes significant. The barometer uses a silicon strain gage, which senses the deformation of the silicon to determine the barometric pressure. The relationship between the deformation of the silicon and the variation of pressure is very complicated and hard to model, but it is a lag system. Figure 5.4 shows the barometric height measurement error in kinematic mode, during the Nose Hill test. The height error may be modeled as a first-order Gauss-Markov process driven by a white noise process as shown in Figure 5.5 (Siouris, 1993).

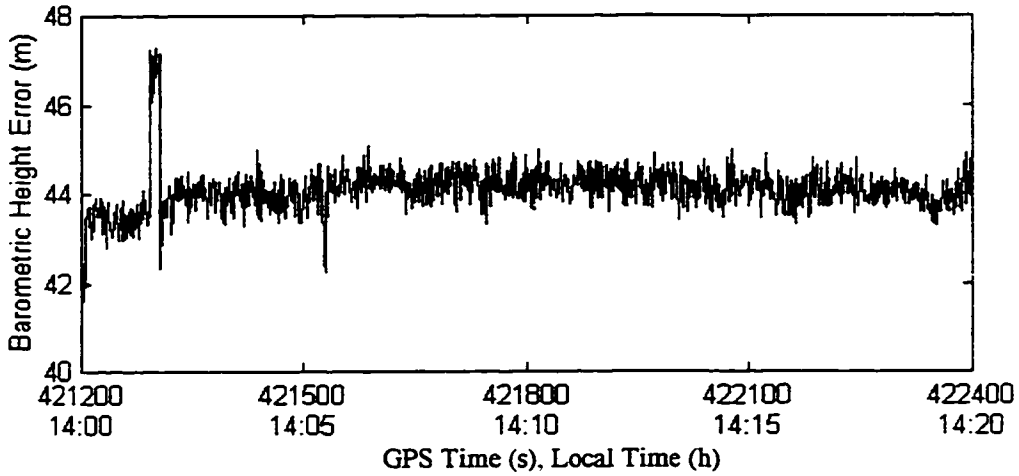

Figure 5.3 Barometric height error in static mode

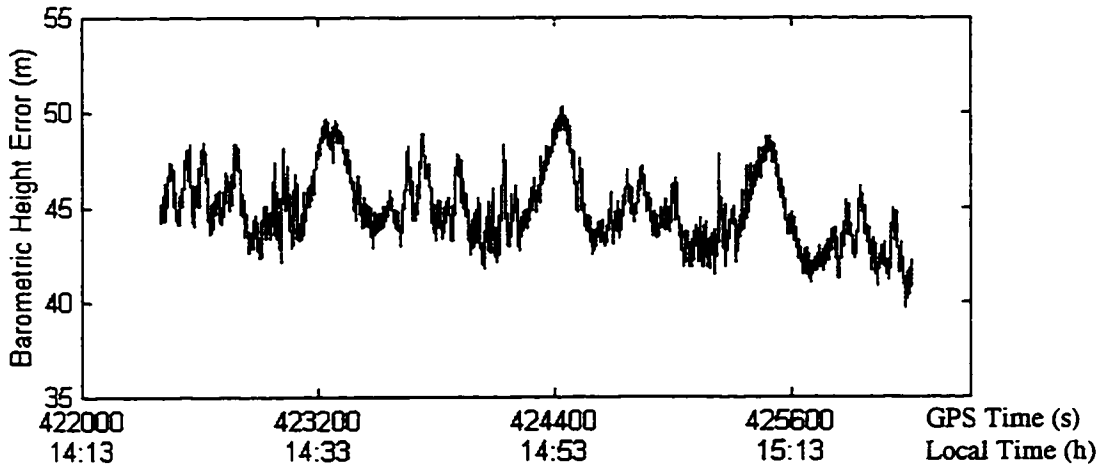

Figure 5.4 Barometric height error in kinematic mode

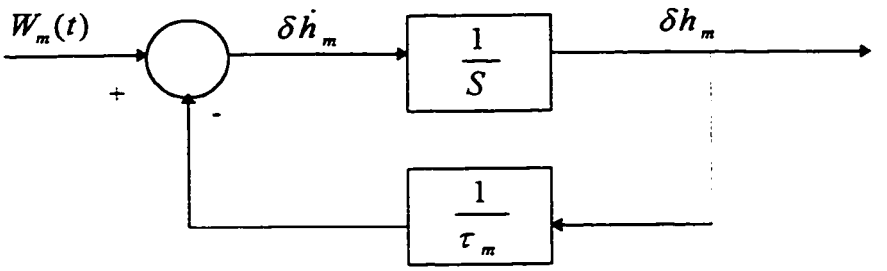

Figure 5.5 Model for the barometric height measurement error

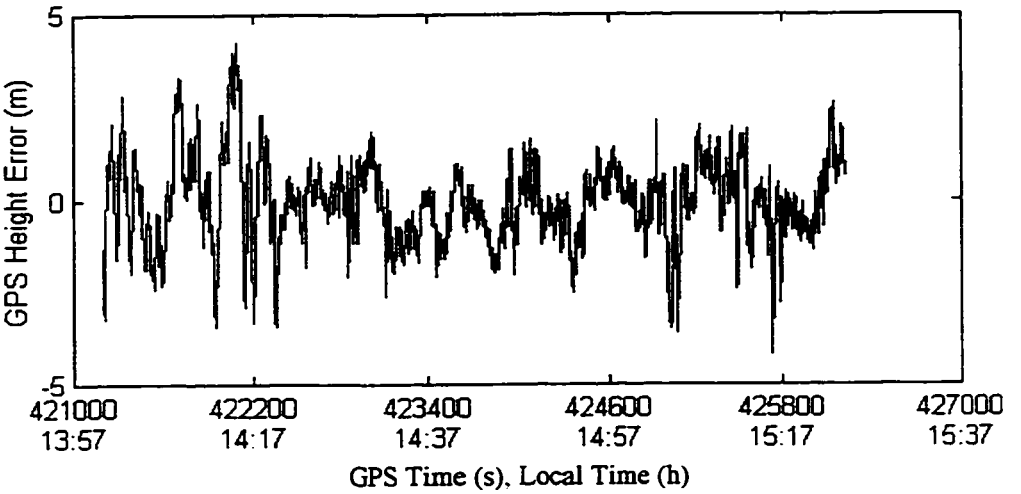

Figure 5.6 GPS height error in static differential mode

The barometric height measurement error can be written directly from Figure 5.5 as follows (where S is the complex frequency of the Laplace transform):

$$\delta\dot{h}_m = -\frac{1}{\tau_m}\delta h_m + W_m \tag{5.3}$$

where τ_m is correlation time

W_m is white noise driving process

5.3.3 GPS height error

Figure 5.6 shows the GPS height error results of the Nose Hill test. The GPS height error can be modeled as a first-order Gauss-Markov process also. It can be written as follows:

$$\dot{\delta h}_G = -\frac{1}{\tau_G}\delta h_G + W_G \tag{5.4}$$

where τ_G is correlation time

W_G is white noise driving process

5.3.4 Estimation of parameters in height error models

Both the barometric height measurement error and the GPS height error are modeled as first-order Gauss-Markov processes. Their discrete forms are:

$$x_k + a_1 x_{k-1} = W_k \tag{5.5}$$

where x_k is the sampling value of the height error at time $t = k \cdot \Delta t$

W_k is the sampled value of the white noise at time $t = k \cdot \Delta t$

$a_1 = e^{-\frac{\Delta t}{\tau}}$ is the parameter to be estimated

τ is the correlation time

Δt is the sampling interval.

When the process x_k has a zero mean, Eq. (5.5) is a standard Autoregressive (AR) model. When the process x_k has a non-zero mean μ, then a suitable model is easily constructed by using a model for the deviation (x_k -μ). This leads to the slightly more general model (Priestley, 1981):

$$x_k - \mu + a_1(x_{k-1} - \mu) = W_k . \tag{5.6}$$

To estimate the parameter a_1 and the variance of the white noise $\sigma^2 = E\{W_k^2\}$, Yule-Walker equations are used (Blais & Vassiliou, 1987):

$$\begin{bmatrix} R_x(0) & R_x(-1) \\ R_x(1) & R_x(0) \end{bmatrix} \begin{bmatrix} 1 \\ a_1 \end{bmatrix} = \begin{bmatrix} \sigma^2 \\ 0 \end{bmatrix} \tag{5.7}$$

where $R_x(k) = \frac{1}{N-k}\sum_{i=0}^{N-k-1} x_{k+i}x_i$ is the autocorrelation function of the process x_k

N is the sampling number and τ is derived from a_1 .

Table 5.3 lists the parameters estimated from the data of the Nose Hill test.

Table 5.3 Summary of parameter estimation from the data of the Nose Hill test

Static mode

	a_1	σ^2 (m^2)	τ (second)
Barometric height error	0.6244	1.72×10^{-5}	2.12
GPS height error	0.9813	0.0827	52.97

Kinematic mode

Barometric height error	0.9858	3.34×10^{-5}	69.92
GPS height error	0.9825	0.0627	56.64

5.3.4 Consideration of the height error models

In static mode, the measured correlation time of the barometric height measurement error is much shorter than that of the GPS height error. The Kalman filter can decouple the two height errors from the measurement of $(h_b - h_G)$ by separating the rapidly changing error (barometric height measurement error) from the slowly changing error (GPS height error).

In kinematic mode, however, the measured correlation time of the barometric height error is very close to that of the GPS height error. The Kalman filter is unable to separate the two height errors. That is, the estimation of the barometric height error would be very poor. Besides, the barometric height error is actually proportional to the variation of pressure. It is both time and space correlated. Therefore, the first-order Gauss-Markov process is not appropriate for the barometric channel. If the model for the barometric height error is built as an integrated random walk as shown in Figure 5.7, the Kalman filter for the barometer will be able to distinguish the two height errors. The model can be written as:

$$\begin{cases} \dot{\delta v}_m = W_m \\ \dot{\delta h}_m = \delta v_m \end{cases} \tag{5.8}$$

where δv_m is the velocity of the barometric height error

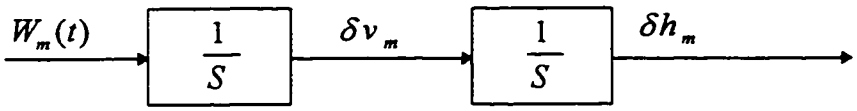

Figure 5.7 Integrated random walk model for the barometric height error

5.3.6 Kalman filter models for the barometer

Four variables, namely the barometric height bias, the barometric height measurement error, the velocity of the barometric height error and the GPS height error are chosen to compose the system state vector. By combining Eq. (5.2), (5.4) and (5.8), the process model can be described by the following differential equation:

$$\begin{bmatrix} \dot{\delta h}_0 \\ \dot{\delta h}_m \\ \dot{\delta v}_m \\ \dot{\delta h}_G \end{bmatrix} = \begin{bmatrix} 0 & 0 & 0 & 0 \\ 0 & 0 & 1 & 0 \\ 0 & 0 & 0 & 0 \\ 0 & 0 & 0 & -\frac{1}{\tau_G} \end{bmatrix} \begin{bmatrix} \delta h_0 \\ \delta h_m \\ \delta v_m \\ \delta h_G \end{bmatrix} + \begin{bmatrix} 0 \\ 0 \\ W_m \\ W_G \end{bmatrix} \tag{5.9}$$

From Eq. (5.9), the state transition matrix can be derived as:

$$\Phi = \begin{bmatrix} 1 & 0 & 0 & 0 \\ 0 & 1 & \Delta t & 0 \\ 0 & 0 & 1 & 0 \\ 0 & 0 & 0 & e^{-\frac{\Delta t}{\tau_G}} \end{bmatrix} \tag{5.10}$$

The process noise covariance matrix is as follows:

$$\mathbf{Q} = \begin{bmatrix} 0 & 0 & 0 & 0 \\ 0 & \frac{s_m \Delta t^3}{3} & \frac{s_m \Delta t^2}{2} & 0 \\ 0 & \frac{s_m \Delta t^2}{2} & s_m \Delta t & 0 \\ 0 & 0 & 0 & \sigma_G^2 \frac{\tau_G}{2}(1 - e^{-\frac{2\Delta t}{\tau_G}}) \end{bmatrix}$$

(5.11)

where s_m is the white noise spectral amplitude for W_m

$\sigma_G^2 = E\{W_G^2\}$ is the variance of W_G.

The white noise spectral amplitude $s_m = 1 \times 10^{-6}$ was chosen for the process noise matrix.

For the barometric height h_b, the observation equation is:

$$h_b = h + \delta h_0 + \delta h_m \tag{5.12}$$

where h is the true height.

For the GPS height h_G, the observation equation can be written as:

$$h_G = h + \delta h_G + W \tag{5.13}$$

where W is white noise.

Combining Eq. (5.12) and (5.13), the measurement model can be described as:

$$Z = h_b - h_G = \delta h_0 + \delta h_m - \delta h_G - W \tag{5.14}$$

or, in vector form:

$$\mathbf{Z} = \begin{bmatrix} 1 & 1 & 0 & -1 \end{bmatrix} \begin{bmatrix} \delta h_0 \\ \delta h_m \\ \delta v_m \\ \delta h_G \end{bmatrix} + [-W] \tag{5.15}$$

The Kalman filter measurement matrix is

$$\mathbf{H_k} = [\,1 \;\; 1 \;\; 0 \;\; -1\,] \tag{5.16}$$

and the measurement noise covariance is:

$$R = E\{W^2\}. \tag{5.17}$$

5.4 Kalman Filter Design for the Gyro

The Kalman filter for the gyro is similar to the filter for the barometer. It estimates the gyro heading error from the measurement difference between the gyro heading and the GPS heading.

5.4.1 Gyro heading

The Andrew AutoGYRO digital fiber optic gyro was used as a heading rate gyro. The relationship between the gyro heading Ψ_g and the output of the gyro, i.e., gyro rate ω_g, is as follows:

$$\Psi_g = \int_0^t \omega_g dt + \Psi_0 \tag{5.18}$$

where Ψ_0 is the initial heading, which satisfies:

$$\dot{\Psi}_0 = 0 \tag{5.19}$$

The heading rate gyro cannot measure the initial heading. It needs calibration by external information to make the gyro useful. This calibration is implemented by the GPS heading in the system.

5.4.2 Gyro heading error

Besides the initial heading, the heading rate gyro has its measurement error, or gyro drift. The gyro heading error may be written as:

$$\delta\dot{\Psi}_g = \delta\omega_g \tag{5.20}$$

where $\delta\Psi_g$ is the gyro heading error

$\delta\omega_g$ is the gyro drift

Usually, the gyro drift consists of white noise, a random bias and a first-order Gauss-Markov process, namely (Yu, 1984):

$$\delta\omega_g = W_g + \delta\omega_b + \delta\omega_m \tag{5.21}$$

where W_g is white noise drift

$\delta\omega_b$ is random bias drift

$\delta\omega_m$ is the first-order Gauss-Markov process drift

with $\delta\dot{\omega}_b = 0$ (5.22)

and $$\delta\dot{\omega}_m = -\frac{1}{\tau_{mg}}\delta\omega_m + W_{mg} \tag{5.23}$$

where W_{mg} is driving white noise and

τ_{mg} is the correlation time

5.4.3 GPS heading error

The GPS heading Ψ_G can be obtained from velocity component solutions:

$$\Psi_G = \tan^{-1}\left(\frac{V_E}{V_N}\right) \tag{5.24}$$

where V_E is the GPS longitude velocity

V_N is the GPS latitude velocity.

The GPS heading error $\delta\Psi_G$ can be derived from Eq. (5.24):

$$\delta\Psi_G = \frac{V_N}{V_E^2 + V_N^2}\delta V_E - \frac{V_N}{V_E^2 + V_N^2}\delta V_N \tag{5.25}$$

where δV_E is the GPS longitude velocity error and

δV_N is the GPS latitude velocity error.

The variance of the GPS heading error σ_G^2 can be written as:

$$\sigma_G^2 = \frac{V_N^2}{(V_E^2 + V_N^2)^2}\sigma_E^2 + \frac{V_E^2}{(V_E^2 + V_N^2)^2}\sigma_N^2 \tag{5.26}$$

where σ_E^2 is the variance of GPS longitude velocity error and

σ_N^2 is the variance of GPS latitude velocity error.

Under the assumption that the GPS longitude velocity error is independent of the GPS latitude velocity error and both of the velocity errors have the same variance to simplify the estimation of GPS heading error, Eq. (5.26) may be written as

$$\sigma_G^2 = \frac{\sigma_{VC}^2}{V^2}, \tag{5.27}$$

where $V = \sqrt{V_E^2 + V_N^2}$ is the horizontal speed and

$\sigma_{VC}^2 = \sigma_E^2 = \sigma_N^2$ is the variance of the GPS velocity component error.

The accuracy of the GPS heading depends on the horizontal speed and the accuracy of the GPS velocity. In differential mode, the standard deviation of the GPS velocity error is approximately 0.05 ms^{-1} under good geometry. To calibrate the gyro heading to an accuracy of 0.01 rad (95%), the horizontal speed should be more than 10 ms^{-1}.

5.4.4 Estimation of parameters in heading error models

The gyro shift error is modeled as combination of a constant bias and a first-order Gauss-Markov process. The standard AR model of Eq. (5.5) is used to estimate the parameter a_1 and the variance of the driving white noise σ^2.

Figure 5.8 presents the gyro drift error in static mode, the result of the Nose Hill test. The constant bias dominates the gyro shift error. Figure 5.9 presents the gyro shift error in kinematic mode, results of the Nose Hill test. The Gauss-Markov process dominates the gyro shift error in kinematic operation since the gyro was fixed on the frame of the vehicle; the attitude of the vehicle varied with the road surface and so did the gyro, as it sensed the related false heading rate. Table 5.4 summarizes the parameters estimated by Eq. (5.7).

Table 5.4 The summary of the parameters in gyro shift error model

	a_1	σ^2 (rad^2)	τ (second)
Static mode	0.4226	5.36×10^{-4}	1.16
Kinematic mode	0.0663	0.2496	0.37

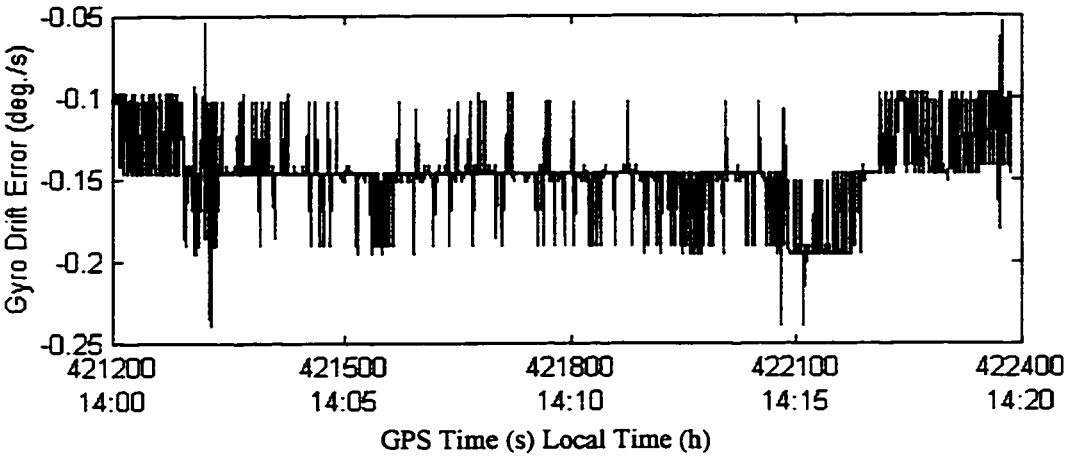

Figure 5.8 Gyro drift error in static mode

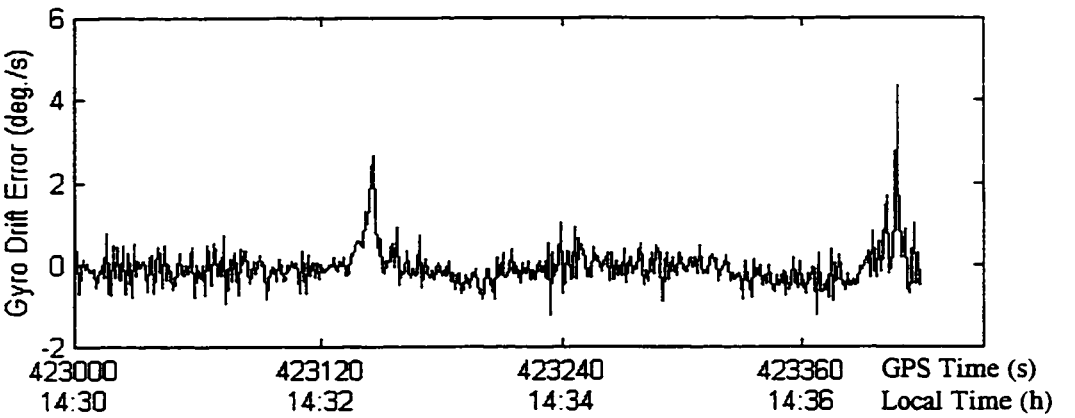

Figure 5.9 Gyro drift error in kinematic mode

5.4.5 Kalman filter models for the gyro

Four variables, namely initial heading, gyro heading error, gyro's constant bias drift and gyro's Gauss-Markov process drift, were chosen to compose the system state vector. By combining Eq. (5.19) through (5.23), the process model can be derived as the following differential equation:

$$\begin{bmatrix} \dot{\Psi}_0 \\ \delta\dot{\Psi}_g \\ \delta\dot{\omega}_b \\ \delta\dot{\omega}_m \end{bmatrix} = \begin{bmatrix} 0 & 0 & 0 & 0 \\ 0 & 0 & 1 & 1 \\ 0 & 0 & 0 & 0 \\ 0 & 0 & 0 & -\dfrac{1}{\tau_m} \end{bmatrix} \begin{bmatrix} \Psi_0 \\ \delta\Psi_g \\ \delta\omega_b \\ \delta\omega_m \end{bmatrix} + \begin{bmatrix} 0 \\ W_g \\ 0 \\ W_m \end{bmatrix} \tag{5.28}$$

From Equ. (5.28), the state transition matrix can be derived as:

$$\Phi = \begin{bmatrix} 1 & 0 & 0 & 0 \\ 0 & 1 & \Delta t & e^{-\frac{\Delta t}{\tau_m}} \\ 0 & 0 & 1 & 0 \\ 0 & 0 & 0 & e^{-\frac{\Delta t}{\tau_m}} \end{bmatrix} \tag{5.29}$$

The process noise is as follows:

$$\mathbf{Q} = \begin{bmatrix} 0 & 0 & 0 & 0 \\ 0 & \sigma_g^2 \Delta t + \frac{\tau_m}{3} - e^{-\frac{3\Delta t}{\tau_m}} & 0 & \frac{\tau_m}{3} - e^{-\frac{3\Delta t}{\tau_m}} \\ 0 & 0 & 0 & 0 \\ 0 & \frac{\tau_m}{3} - e^{-\frac{3\Delta t}{\tau_m}} & 0 & \sigma_m^2 \left(\frac{\tau_m}{2} - e^{-\frac{2\Delta t}{\tau_m}} \right) \end{bmatrix} \tag{5.30}$$

where $\begin{cases} \sigma_g^2 = E\{W_g^2\} \\ \sigma_m^2 = E\{W_m^2\} \end{cases}$

For the gyro heading, the observation equation can be written as:

$$\Psi_g = \Psi + \Psi_0 + \delta\Psi_g \tag{5.31}$$

where Ψ is the true heading.

For the GPS heading, the observation equation can be written as:

$$\Psi_G = \Psi + W_{\Psi.G} \tag{5.32}$$

where $W_{\Psi.G}$ is white noise.

Combining Eq. (5.31) and (5.32), the measurement model can be written as:

$$Z = \Psi_g - \Psi_G = \Psi_0 + \delta\Psi_g - W_{\Psi.G} \tag{5.33}$$

or, in vector form:

$$\mathbf{Z} = \begin{bmatrix} 1 & 1 & 0 & 0 \end{bmatrix} \begin{bmatrix} \Psi_0 \\ \delta\Psi_g \\ \delta\omega_b \\ \delta\omega_m \end{bmatrix} + [-W_{\Psi.G}]. \tag{5.34}$$

The Kalman filter measurement matrix is:

$$\mathbf{H_k} = [\,1 \quad 1 \quad 0 \quad 0\,] \tag{5.35}$$

and the measurement noise variance is as follows:

$$R = E\{W_{\Psi.G}^2\}. \tag{5.36}$$

5.5 Master Kalman Filter Design

In the master filter, the updated local information, the barometric height, the gyro heading and the filtered clock offset, are recombined with the raw measurement of GPS, namely, pseudorange and Doppler, to form a new total sum - a fused solution (Carlson, 1988).

The Position-Velocity (PV) model was chosen for the GPS problem, since the Position-Velocity-Acceleration (PVA) model hardly improves positioning accuracy in the case of moderate vehicle dynamics (e.g. Cannon, 1991; Gao, 1992; Bullock, 1995). The PV dynamic process can be described by the following vector differential equation (Hwang & Brown, 1990; Brown & Hwang, 1992):

$$\begin{bmatrix} \delta\dot{P}_E \\ \delta\dot{V}_E \\ \delta\dot{P}_N \\ \delta\dot{V}_N \\ \delta\dot{H} \\ \delta\dot{V}_H \\ c\dot{\delta t} \\ c\dot{\omega}_t \end{bmatrix} = \begin{bmatrix} 0 & 1 & 0 & 0 & 0 & 0 & 0 & 0 \\ 0 & 0 & 0 & 0 & 0 & 0 & 0 & 0 \\ 0 & 0 & 0 & 1 & 0 & 0 & 0 & 0 \\ 0 & 0 & 0 & 0 & 0 & 0 & 0 & 0 \\ 0 & 0 & 0 & 0 & 0 & 1 & 0 & 0 \\ 0 & 0 & 0 & 0 & 0 & 0 & 0 & 0 \\ 0 & 0 & 0 & 0 & 0 & 0 & 0 & 1 \\ 0 & 0 & 0 & 0 & 0 & 0 & 0 & 0 \end{bmatrix} \begin{bmatrix} \delta P_E \\ \delta V_E \\ \delta P_N \\ \delta V_N \\ \delta H \\ \delta V_H \\ c\delta t \\ c\omega_t \end{bmatrix} + \begin{bmatrix} 0 \\ W_E \\ 0 \\ W_N \\ 0 \\ W_H \\ W_t \\ W_\omega \end{bmatrix} \tag{5.37}$$

where δP_E is the longitude position error

δV_E is the longitude velocity error

δP_N is the latitude position error

δV_N is the latitude velocity error

δH is the vertical position error

δV_H is the vertical velocity error

$c\delta t$ is the range clock offset error

$c\delta\omega_t$ is the range clock drift error

and the amplitudes associated with the white noise driving function are s_p for W_E, W_N and W_H, s_f for W_t and s_g for W_ω.

From Eq. (5.37), the state transition matrix can be derived as:

$$\Phi = \begin{bmatrix} 1 & \Delta t & 0 & 0 & 0 & 0 & 0 & 0 \\ 0 & 1 & 0 & 0 & 0 & 0 & 0 & 0 \\ 0 & 0 & 1 & \Delta t & 0 & 0 & 0 & 0 \\ 0 & 0 & 0 & 1 & 0 & 0 & 0 & 0 \\ 0 & 0 & 0 & 0 & 1 & \Delta t & 0 & 0 \\ 0 & 0 & 0 & 0 & 0 & 1 & 0 & 0 \\ 0 & 0 & 0 & 0 & 0 & 0 & 1 & \Delta t \\ 0 & 0 & 0 & 0 & 0 & 0 & 0 & 1 \end{bmatrix} \tag{5.38}$$

The process noise covariance matrix is as follows:

$$\mathbf{Q}=\begin{bmatrix}
\frac{s_p\Delta t^3}{3} & \frac{s_p\Delta t^2}{2} & 0 & 0 & 0 & 0 & 0 & 0 \\
\frac{s_p\Delta t^2}{2} & s_p\Delta t & 0 & 0 & 0 & 0 & 0 & 0 \\
0 & 0 & \frac{s_p\Delta t^3}{3} & \frac{s_p\Delta t^2}{2} & 0 & 0 & 0 & 0 \\
0 & 0 & \frac{s_p\Delta t^2}{2} & s_p\Delta t & 0 & 0 & 0 & 0 \\
0 & 0 & 0 & 0 & \frac{s_p\Delta t^3}{3} & \frac{s_p\Delta t^2}{2} & 0 & 0 \\
0 & 0 & 0 & 0 & \frac{s_p\Delta t^2}{2} & s_p\Delta t & 0 & 0 \\
0 & 0 & 0 & 0 & 0 & 0 & s_f+\frac{s_g\Delta t^3}{3} & \frac{s_g\Delta t^2}{2} \\
0 & 0 & 0 & 0 & 0 & 0 & \frac{s_g\Delta t^2}{2} & s_g\Delta t
\end{bmatrix} \tag{5.39}$$

For the measurement of pseudoranges, the measurement vector equation is given by:

$$\mathbf{Z}_\rho = \mathbf{H}_\rho\mathbf{x} + \mathbf{v}_\rho \tag{5.40}$$

where $\mathbf{x}=\begin{bmatrix}\delta P_E & \delta V_E & \delta P_N & \delta V_N & \delta H & \delta V_H & c\delta t & c\delta\omega_t\end{bmatrix}^T$ is the system state vector

$\mathbf{Z}_\rho=\begin{bmatrix}\rho_1-\hat{\rho}_1(x_0) & \cdots & \rho_n-\hat{\rho}_n(x_0)\end{bmatrix}^T$ is the pseudorange error

ρ_i is the measured pseudorange

x_0 is the nominal point of linearization based on predicted position and receiver time,

$\hat{\rho}_i(x_0)$ is the predicted pseudorange based on x_0.

$$\mathbf{H}_\rho=\begin{bmatrix}
h_x^{(1)} & 0 & h_y^{(1)} & 0 & h_z^{(1)} & 0 & 1 & 0 \\
\vdots & \vdots & \vdots & \vdots & \vdots & \vdots & \vdots & \vdots \\
h_x^{(n)} & 0 & h_y^{(n)} & 0 & h_z^{(n)} & 0 & 1 & 0
\end{bmatrix}$$

$\begin{bmatrix}h_x^{(i)} & h_y^{(i)} & h_z^{(i)}\end{bmatrix}=\begin{bmatrix}\frac{\partial\rho_i}{\partial P_E} & \frac{\partial\rho_i}{\partial P_N} & \frac{\partial\rho_i}{\partial h}\end{bmatrix}$ are the direction cosines

$\mathbf{v}_\rho=\begin{bmatrix}v_{\rho 1} & \cdots & v_{\rho n}\end{bmatrix}^T$ is pseudorange measurement (white) noise

For the instantaneous Doppler measurements, the measurement equation is described as:

$$\mathbf{Z}_{\dot{\rho}} = \mathbf{H}_{\dot{\rho}}\mathbf{x} + \mathbf{v}_{\dot{\rho}} \tag{5.41}$$

where $\mathbf{Z}_{\dot{\rho}} = \left[\dot{\rho}_1 - \hat{\dot{\rho}}_1(x_0) \quad \cdots \quad \dot{\rho}_n - \hat{\dot{\rho}}_n(x_0)\right]^T$ is the Doppler error

$\dot{\rho}_i$ is the measured Doppler

$\hat{\dot{\rho}}_i(x_0)$ is the predicted Doppler based on x_0

$$\mathbf{H}_{\dot{\rho}} = \begin{bmatrix} 0 & h_x^{(1)} & 0 & h_y^{(1)} & 0 & h_z^{(1)} & 0 & 1 \\ \vdots & \vdots & \vdots & \vdots & \vdots & \vdots & \vdots & \vdots \\ 0 & h_x^{(n)} & 0 & h_y^{(n)} & 0 & h_z^{(n)} & 0 & 1 \end{bmatrix}$$

$\mathbf{v}_{\dot{\rho}} = \left[v_{\dot{\rho}1} \quad \cdots \quad v_{\dot{\rho}n}\right]^T$ is the Doppler measurement (white) noise.

For the measurements filtered by the local filters, namely, barometric height, gyro heading and clock offset, the measurement equation can be written as:

$$\mathbf{Z}_l = \mathbf{H}_l\mathbf{x} + \mathbf{v}_l \tag{5.42}$$

where $\mathbf{Z}_l = \left[h_b - \hat{H}(x_0) \quad ct_r - c\hat{t}(x_0) \quad \Psi_g - \hat{\Psi}(x_0)\right]^T$

h_b, ct, Ψ_g are measured barometric height, range clock offset and gyro heading

$\hat{H}(x_0), c\hat{t}(x_0), \hat{\Psi}(x_0)$ are predicted height, range clock offset and heading

$$\mathbf{H}_l = \begin{bmatrix} 0 & 0 & 0 & 0 & 1 & 0 & 0 & 0 \\ 0 & 0 & 0 & 0 & 0 & 0 & 1 & 0 \\ 0 & \dfrac{V_N}{V_E^2 + V_N^2} & 0 & -\dfrac{V_E}{V_E^2 + V_N^2} & 0 & 0 & 0 & 0 \end{bmatrix}$$

$\mathbf{v}_l = \left[v_b \quad v_t \quad v_g\right]^T$ is the measurement error vector of barometric height, clock offset and gyro heading

Combining Eq. (5.40) through (5.42), the measurement vector equation for the master filter is written as:

$$\mathbf{Z} = \mathbf{H}_k\mathbf{x} + \mathbf{v} \tag{5.43}$$

where $\mathbf{Z} = \begin{bmatrix} Z_\rho & Z_{\dot\rho} & Z_t \end{bmatrix}^T$

$\mathbf{H}_k = \begin{bmatrix} H_\rho & H_{\dot\rho} & H_t \end{bmatrix}^T$

$\mathbf{v} = \begin{bmatrix} v_\rho & v_{\dot\rho} & v_t \end{bmatrix}^T$

Under the assumption (Brown & Hwang, 1992) that measurement errors are uncorrelated, the corresponding measurement covariance matrix is:

$$\mathbf{R} = \begin{bmatrix} r_\rho & 0 & \cdots & 0 & 0 & 0 & 0 & \cdots & 0 & 0 & 0 & 0 & 0 \\ 0 & r_\rho & \cdots & 0 & 0 & 0 & 0 & \cdots & 0 & 0 & 0 & 0 & 0 \\ \vdots & \vdots & \ddots & \vdots & \vdots & \vdots & \vdots & \cdots & \vdots & \vdots & \vdots & \vdots & \vdots \\ 0 & 0 & \cdots & r_\rho & 0 & 0 & 0 & \cdots & 0 & 0 & 0 & 0 & 0 \\ 0 & 0 & \cdots & 0 & r_\rho & 0 & 0 & \cdots & 0 & 0 & 0 & 0 & 0 \\ 0 & 0 & \cdots & 0 & 0 & r_{\dot\rho} & 0 & \cdots & 0 & 0 & 0 & 0 & 0 \\ 0 & 0 & \cdots & 0 & 0 & 0 & r_{\dot\rho} & \cdots & 0 & 0 & 0 & 0 & 0 \\ \vdots & \vdots & \vdots & \vdots & \vdots & \vdots & \vdots & \ddots & \vdots & \vdots & \vdots & \vdots & \vdots \\ 0 & 0 & \cdots & 0 & 0 & 0 & 0 & \cdots & r_{\dot\rho} & 0 & 0 & 0 & 0 \\ 0 & 0 & \cdots & 0 & 0 & 0 & 0 & \cdots & 0 & r_{\dot\rho} & 0 & 0 & 0 \\ 0 & 0 & \cdots & 0 & 0 & 0 & 0 & \cdots & 0 & 0 & r_b & 0 & 0 \\ 0 & 0 & \cdots & 0 & 0 & 0 & 0 & \cdots & 0 & 0 & 0 & r_t & 0 \\ 0 & 0 & \cdots & 0 & 0 & 0 & 0 & \cdots & 0 & 0 & 0 & 0 & r_g \end{bmatrix} \begin{matrix} \\ \\ \\ \} n \\ \\ \\ \\ \\ \\ \} n \\ \\ \\ \\ \\ \end{matrix} \tag{5.44}$$

where r_ρ is the variance of the pseudorange measurement

$r_{\dot\rho}$ is the variance of the Doppler measurement

r_b is the variance of the barometric height measurement

r_t is the variance of the clock offset measurement

r_g is the variance of the gyro heading measurement.

r_ρ and $r_{\dot\rho}$ can be obtained directly from the receiver measurements, and $r_b = 4$ m^2, $r_t = 1$ m^2, $r_g = 0.25$ rad^2 were chosen according to the test results described above.

5.6 Software Design

A program, based on C^{3}NAV™, was developed to implement the system algorithm design described above in post-mision. It uses the basic routines of C^{3}NAV™, such as satellite

ephemeris decoding, satellite orbit computation, satellite clock computation, ionospheric and tropospheric corrections, generating and applying differential corrections, carrier smoothed code generation and standard least squares estimation etc. Therefore, it keeps most of the features of C^3NAV^{TM}, and can process GPS data with Kalman filtering algorithm and integrate GPS with a rubidium clock, a barometer and a gyro. The code for the program was written in C language. Figure 5.10 shows the flowchart of the integrated navigation software.

The navigation software will first read the GPS data and sensor data, then process the GPS data, after that implement Kalman filters, if the standard deviation derived by the master Kalman filter is less than 10 m, the estimates are considered as good estimates.

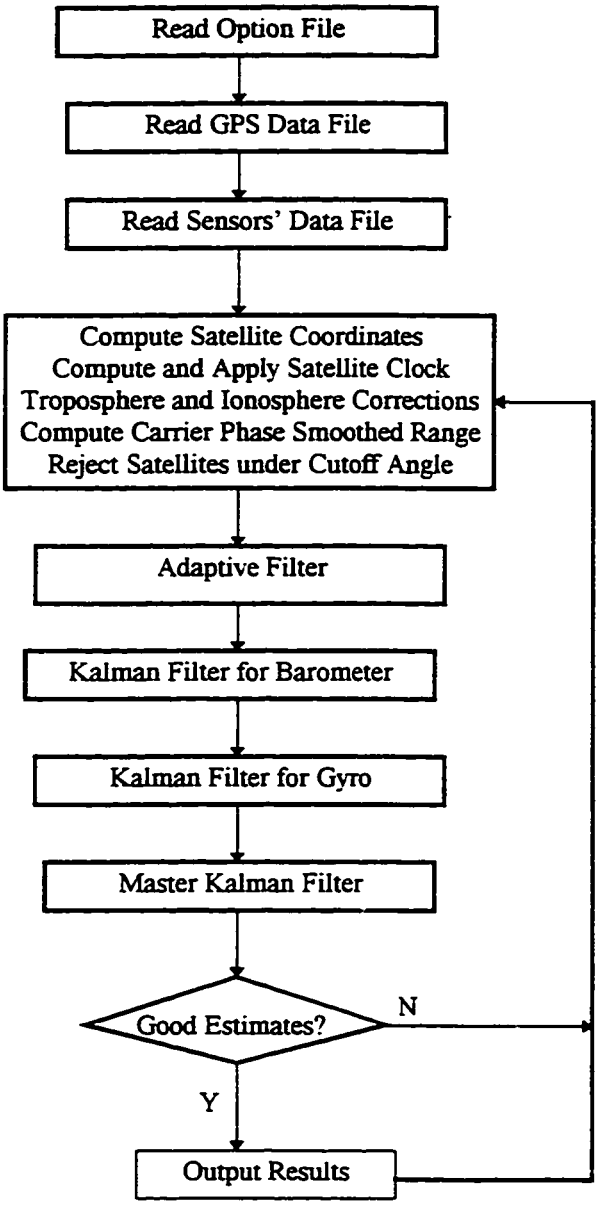

Figure 5.10 Flowchart of the integrated navigation software

CHAPTER 6
FIELD TRIALS AND RESULT ANALYSIS

In order to evaluate the navigation system discussed above, two field tests were conducted. The first test was carried out in a controlled environment, where there were no obstructions along the test route so that excellent satellite coverage and geometry could be continuously obtained during the test. Since a reference route can be provided by carrier phase differential GPS with decimetre level accuracy under these conditions, the advantages of using the rubidium clock can be examined in terms of both accuracy and availability. The second test was carried out in a downtown area of Calgary, where the satellite signals are often masked by tall buildings and/or trees. The purpose of this test was to examine the performance of the navigation system in a typical operational environment.

6.1 Field Test in Controlled Environment

6.1.1 Test description

A field test was carried out at Nose Hill Park, Calgary, on November 28, 1996. To obtain a reference trajectory with a decimetre level accuracy from carrier phase processing with FLYKIN™ (Lachapelle et al., 1996), an ideal environment with excellent satellite coverage and geometry was chosen.

The navigation system, which includes a GPS receiver, a rubidium clock, a barometer and a gyro, was mounted on a vehicle. The antenna of the GPSCard receiver was installed on the roof of the car. Another NovAtel GPSCard receiver with a normal internal TXCO clock was used as the reference station, placed on the roof of the Engineering Building at the University of Calgary, approximately 5 to 10 km away.

L1 C/A code, Doppler, carrier phase, barometric pressure and gyro heading rate measurements were collected at one second intervals over a period of 90 minutes. The

vehicle was kept stationary for twenty minutes before moving to allow the rubidium clock to stabilize. The carrier phase measurements were used to determine the reference trajectory of the test route using FLYKIN™ with an estimated accuracy of about 10 - 20 cm using the ambiguity float mode. Figure 6.1 shows the horizontal reference trajectory.

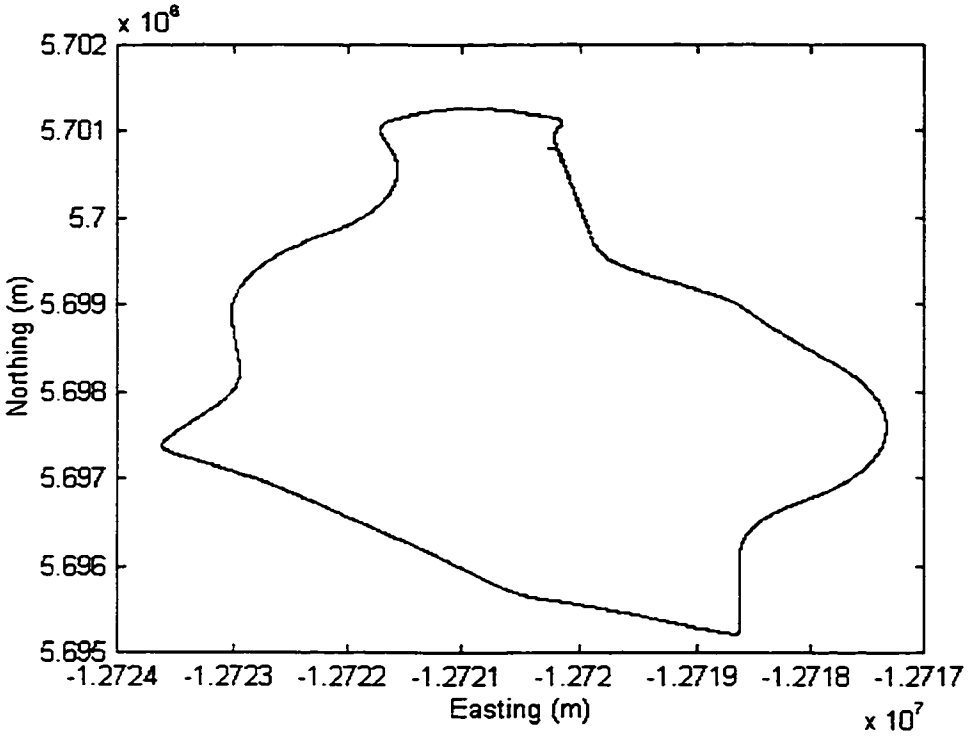

Figure 6.1 Horizontal reference trajectory computed with FLYKIN™

Figure 6.2 presents the number of visible satellites above a cutoff angle of five degrees. Most of the time, the number of visible satellites was more than six. Occasionally, the number of visible satellites fell to five. These few intervals resulted in poor geometry, especially in height (VDOP), as shown in Figure 6.3.

This trial was designed for evaluating the accuracy of rubidium clock aided GPS, and inspecting the capability of the integrated navigation system presented earlier using three, two or even one satellite.

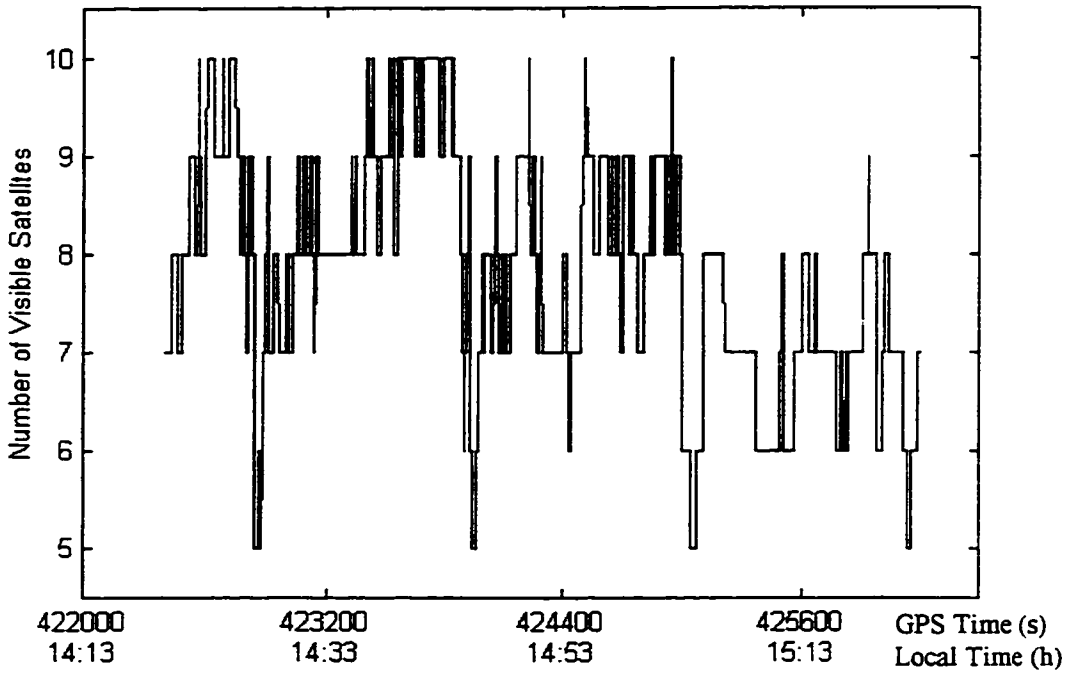

Figure 6.2 Number of visible satellites during the Nose Hill test, above cutoff angle of five degrees

6.1.2 Rubidium clock aided GPS

All point positioning results in this section were computed by using either C^{3}NAV™, which implements a standard LS algorithm and will be referred to as unaided GPS, or C^{4}NAV, which was modified to implement rubidium clock aided GPS algorithm. Both software operate in either stand-alone mode with broadcast clock and ephemeris information, stand-alone mode with post-mission information, or differential mode. C/A code position solutions were computed each second using a satellite cutoff angle of five degrees. Tropospheric corrections were applied and the pseudoranges were carrier phase smoothed in all cases.

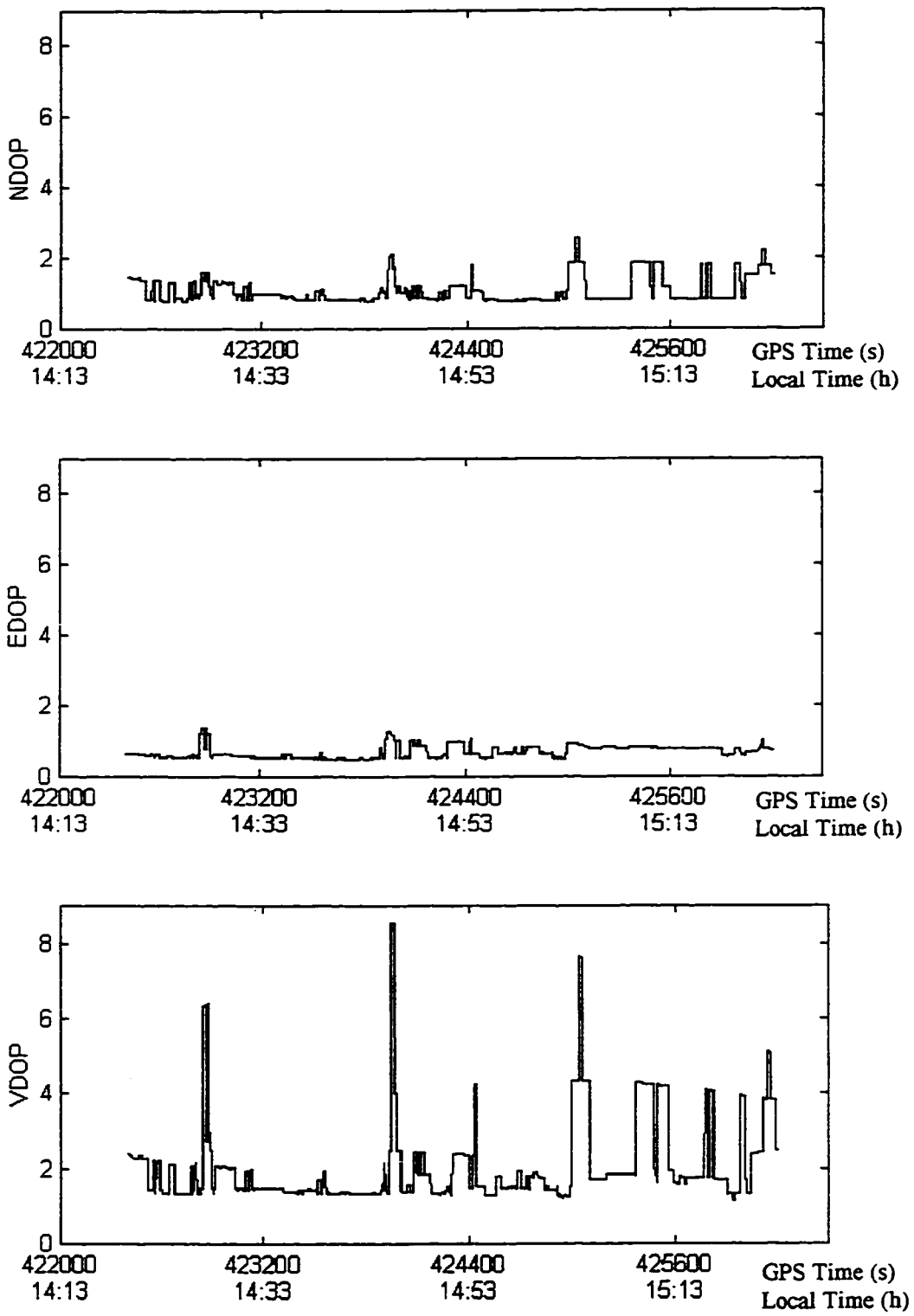

Figure 6.3 Satellite geometry during the Nose Hill test

1. Stand-alone mode with broadcast information

Figure 6.4 presents the position errors of unaided GPS in stand-alone mode using broadcast information. It is obvious that SA was on during the test. Typical SA positioning errors of up to 100 metres occur. The vertical position error spikes due to poor geometry exceed 200 metres several times during the test. The dashed envelopes indicate 3σ error envelopes derived from the least squares estimation. The actual errors are within the estimated accuracy some 95% of the time.

Figure 6.5 presents the position errors of rubidium clock aided GPS in stand-alone mode using broadcast information. Since the low-pass filter is used in the rubidium clock aided algorithm, the effect of smoothing is demonstrated. The sudden changes in positioning errors are eliminated and the position error spikes are removed. Table 6.1 summarizes the results. The results are consistent with the results of the static test described in chapter 4. The EDOP shown is less than 1 during most periods of the time. The longitude errors are practically independent of the clock offset errors. Therefore, the longitude accuracy is nearly not affected with the improvement in the clock offset estimate.

Table 6.1 Statistics of the Nose Hill test, processed in stand-alone mode with broadcast information

MEAN/RMS (m)

	LATITUDE	LONGITUDE	HEIGHT
UNAIDED GPS	2.43/23.24	5.00/15.86	2.70/56.94
RUBIDIUM CLOCK AIDED GPS	1.67/19.02	7.10/16.54	-5.43/14.96

Figure 6.6 presents the correlation coefficients among the three position errors. The solid line indicates the coefficients using unaided GPS, and the dashed line represents the coefficients using clock aided GPS. The latitude error is almost independent of the longitude error, the correlation coefficient between them does not change much for both unaided and clock aided GPS. However, the latitude and longitude errors are correlated to a certain degree with the height error using unaided GPS. The correlation coefficients between the height error and the horizontal errors tend to be smaller and constant when using clock aided GPS.

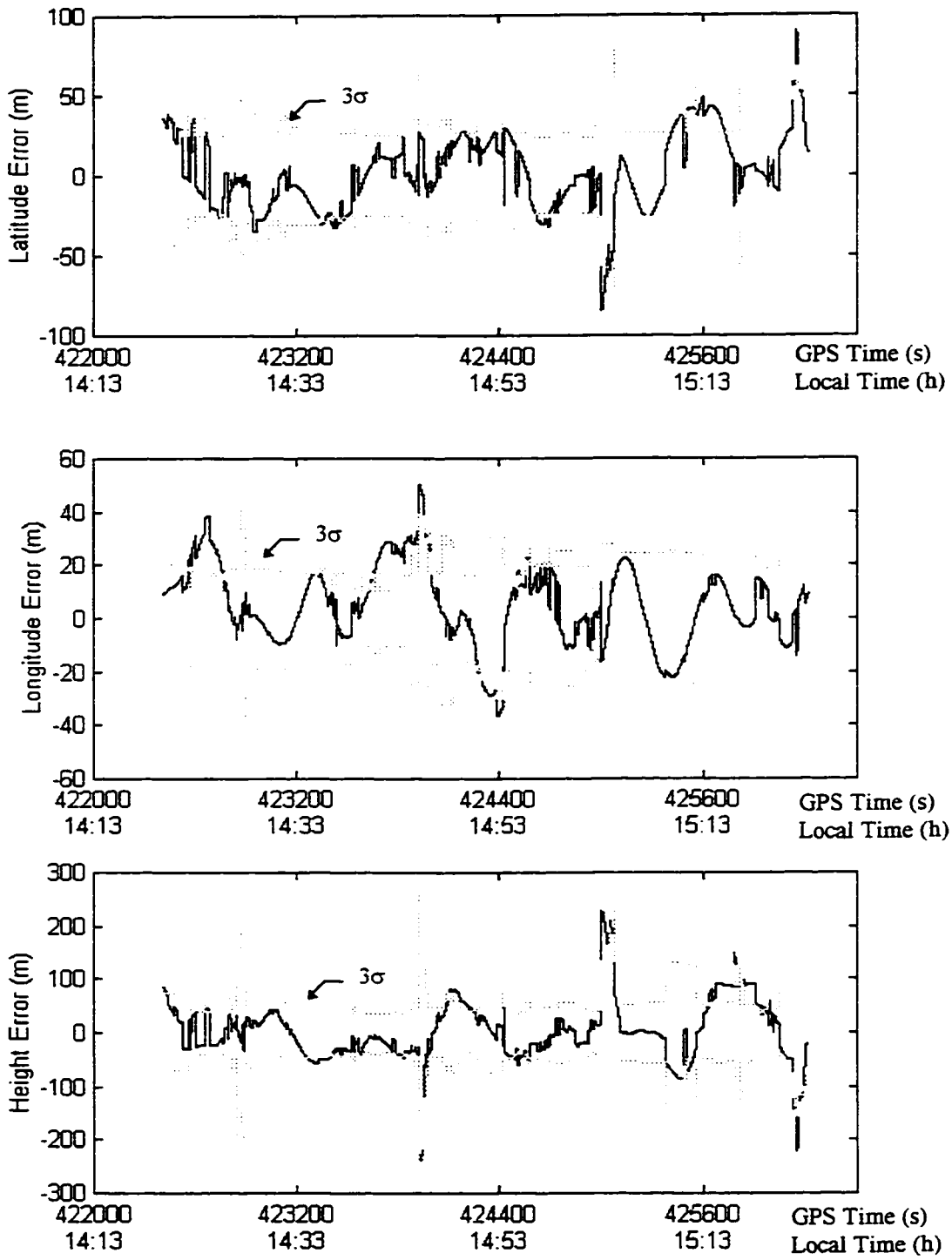

Figure 6.4 Position errors of unaided GPS, processed in stand-alone mode with broadcast information, Nose Hill test

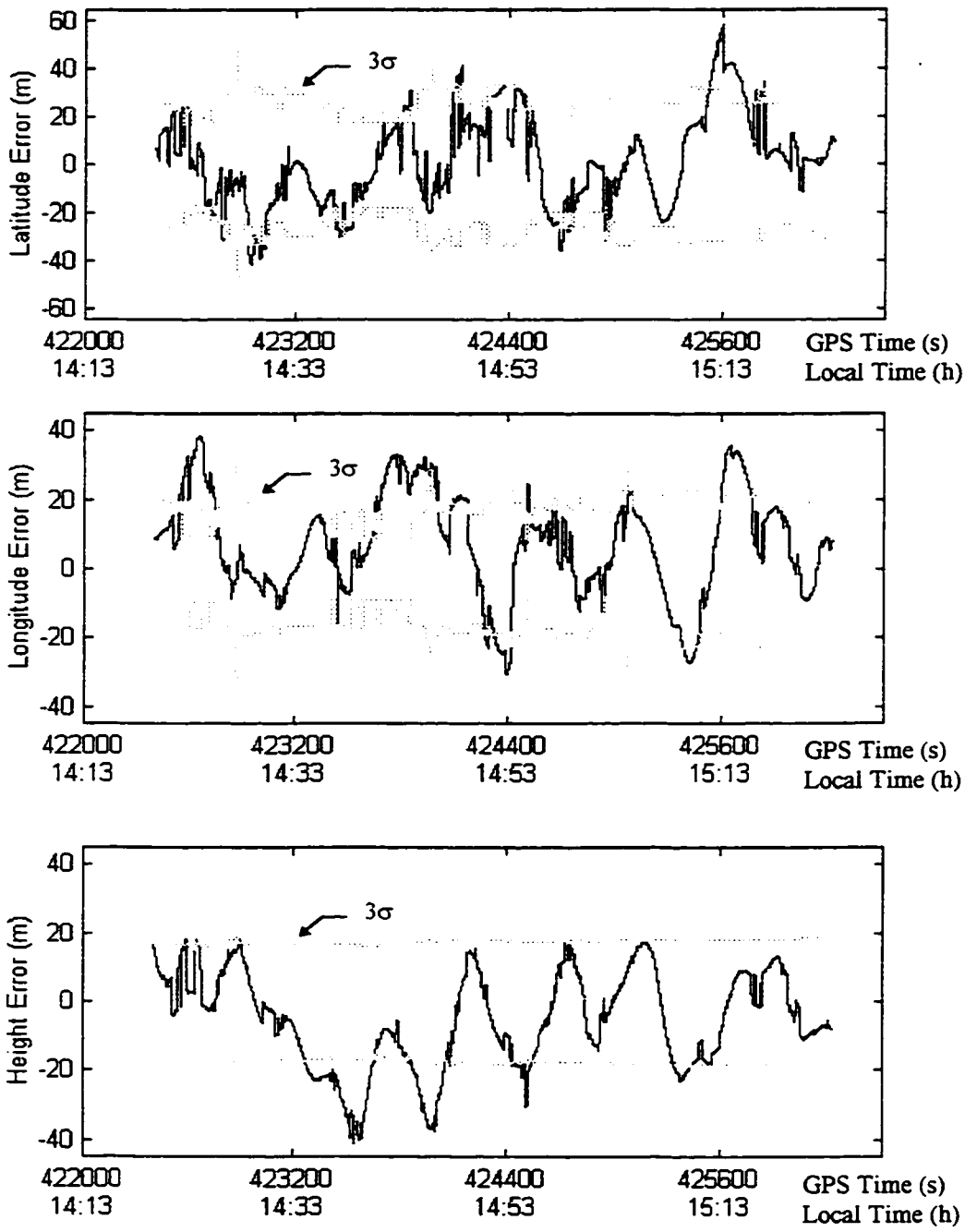

Figure 6.5 Position errors of rubidium clock aided GPS, processed in stand-alone mode with broadcast information, Nose Hill test

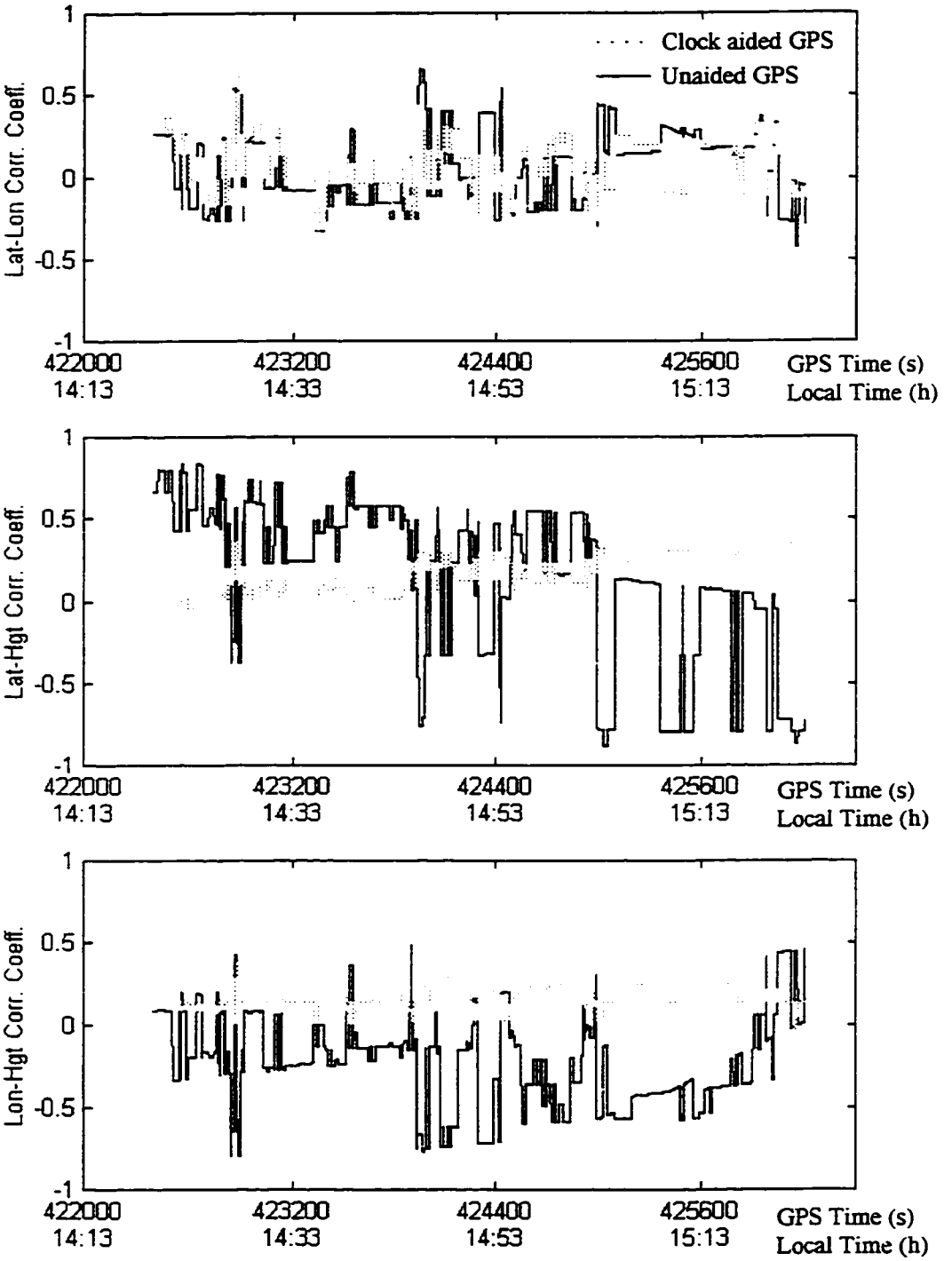

Figure 6.6 Correlation coefficients among three position errors

2. Stand-alone mode with post-mission information

Figure 6.7 presents position errors of unaided GPS in stand-alone mode with post-mission precise satellite orbits and clock corrections. It is clear that a one-to-three metre level accuracy can be achieved by overcoming SA components, namely satellite clock dithering and satellite ephemeris degradation. Biases are significant on both horizontal and vertical error components. They are believed to be mainly due to the ionospheric effect. While the effects of changes in the visible satellites are not apparent, position error spikes due to poor geometry still exist. A large spike at epoch 423436 second in longitude is very noticeable. This is because the GPS receiver output a blunder time measurement at that epoch. While all the pseudorange and Doppler measurements were sampled at the integer second, an exception happened at that point, namely the measurements was sampled at 423436.1 seconds. After careful analysis of data, it was found that the measurements at that point were actually sampled at the integer second, that is, at 423436 seconds, the measurement time was output as 423436.1 seconds. When the measurements at that point was treated as sampled at 423436 second, the spike disappears. For real-time application, this spike is impossible to be detected. It is, therefore, preserved here and later.

Figure 6.8 shows the position errors of rubidium clock aided GPS in stand-alone mode with post-mission precise satellite orbits and clock corrections. The effect of smoothing is demonstrated again by the removal of the position error spikes. Table 6.2 summarizes the results. Although the horizontal accuracy of the rubidium clock aided GPS is almost the same as that of the unaided GPS, the vertical accuracy is improved significantly.

Table 6.2 Statistics of the Nose Hill test, processed in stand-alone mode with post-mission precise satellite orbits and clock corrections

MEAN/RMS (m)

	LATITUDE	LONGITUDE*	HEIGHT
UNAIDED GPS	1.87/1.98	-0.23/0.34	3.25/3.51
RUBIDIUM CLOCK AIDED GPS	1.94/2.00	-0.19/0.29	2.74/2.80

* Excluding the bias at 423436 seconds.

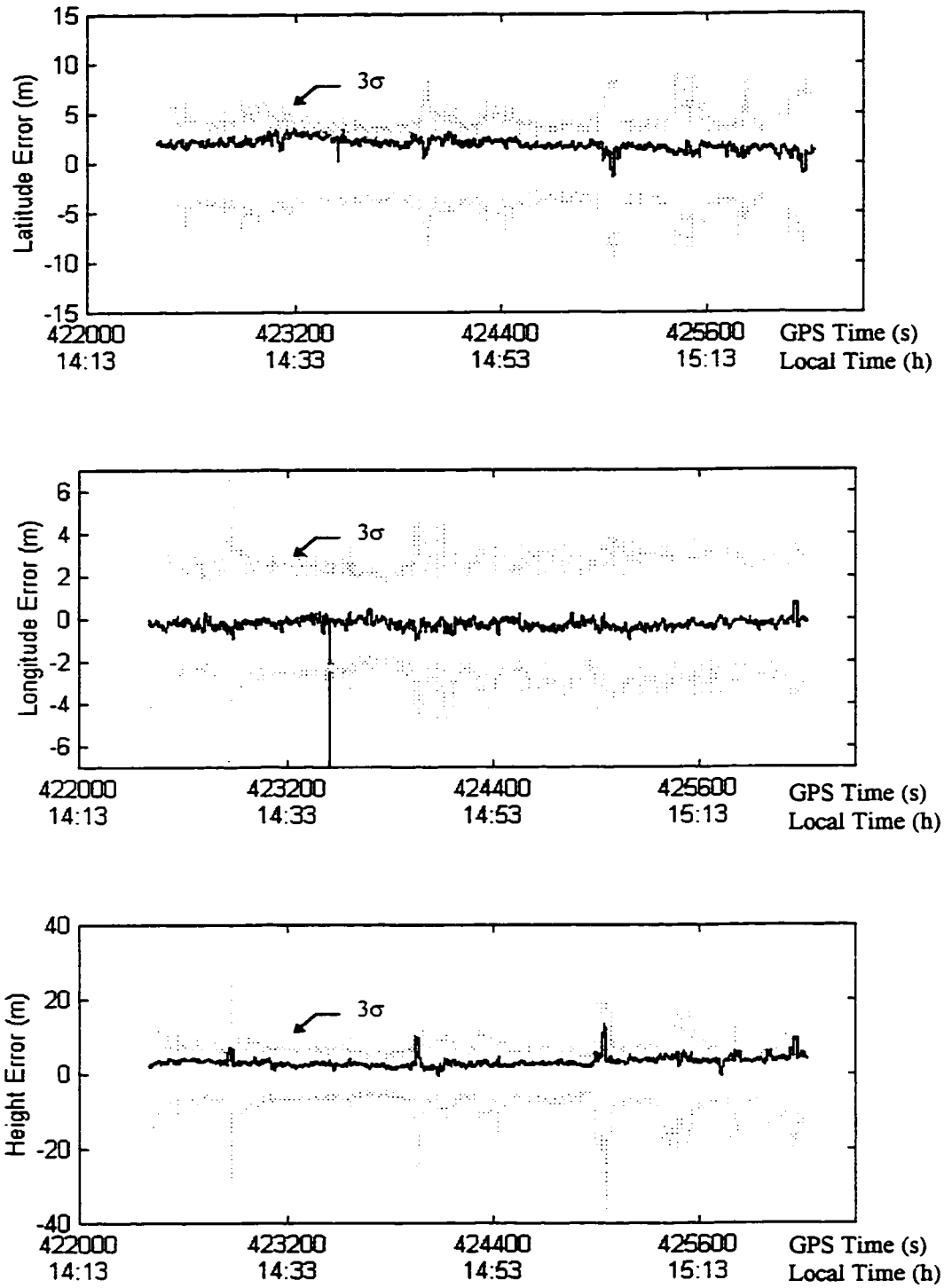

Figure 6.7 Position errors of unaided GPS, processed in stand-alone mode with post-mission information, Nose Hill test

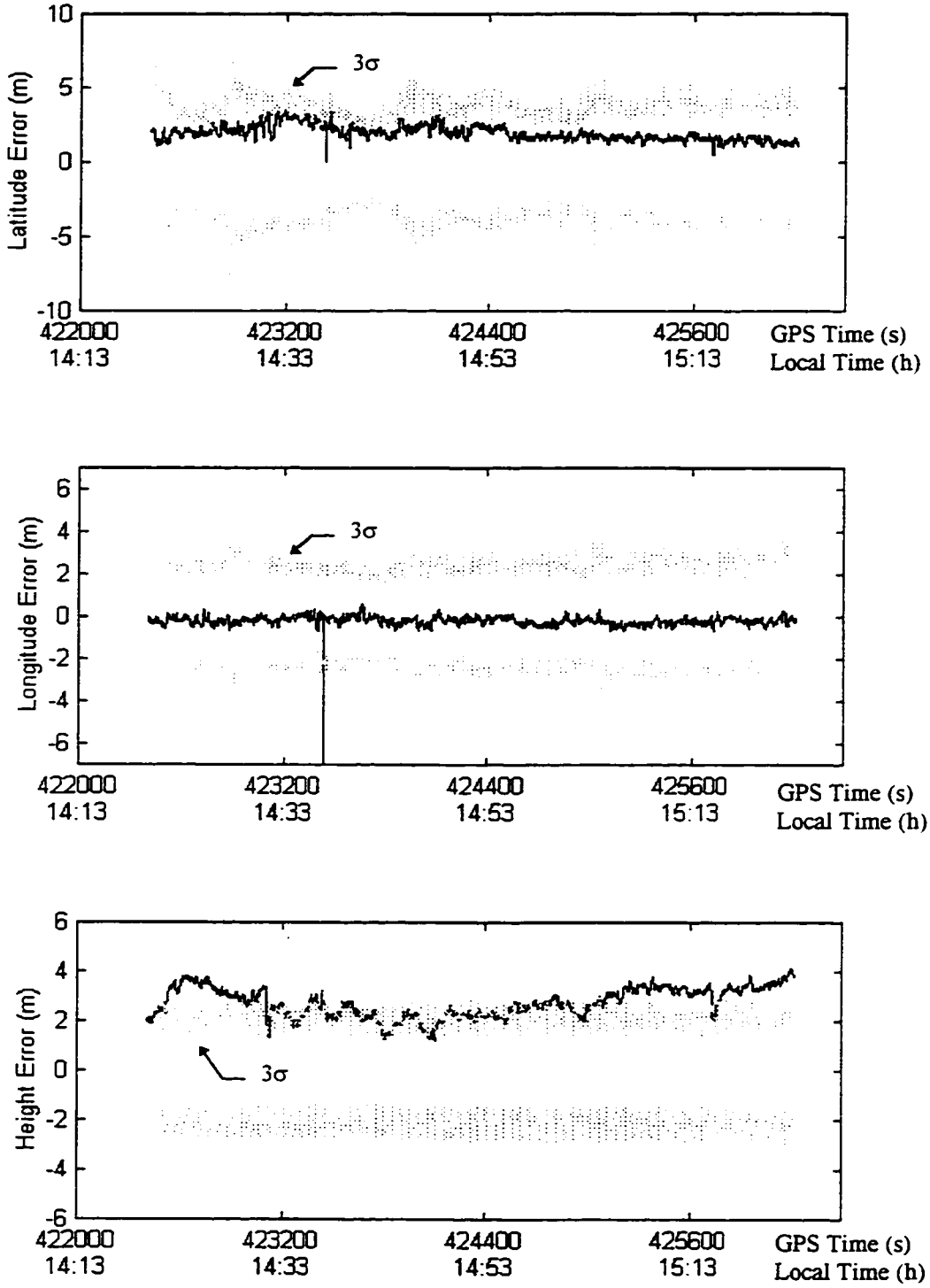

Figure 6.8 Position errors of rubidium clock aided GPS, processed in stand-alone mode with post-mission information, Nose Hill test

3. Differential mode

Figure 6.9 presents the position errors of unaided GPS in differential mode using broadcast ephemerides and satellite clock corrections at both the remote and the reference station. Carrier phase smoothing of the pseudorange measurements was not applied in this case. The position error spikes due to the poor satellite geometry still can be seen in the height error.

Figure 6.10 shows the position error of rubidium clock aided GPS in differential mode using broadcast information at the remote station but post-mission information at the reference station to calculate an accurate time base for the TCXO under SA. The smoothing effect of the rubidium clock aiding is noticeable in the vertical component. Table 6.3 summarizes the results.

Table 6.3 Statistics of the Nose Hill test, processed in pseudorange differential mode

MEAN/RMS (m)

	LATITUDE	LONGITUDE*	HEIGHT
UNAIDED GPS	0.27/0.58	-0.11/0.35	-0.51/0.95
RUBIDIUM CLOCK AIDED GPS	0.24/0.55	-0.10/0.33	-0.34/0.78

* Excluding the bias at 423436 seconds.

Neither improvements in the horizontal or vertical accuracy are significant, however, since the satellite geometry is good everywhere.

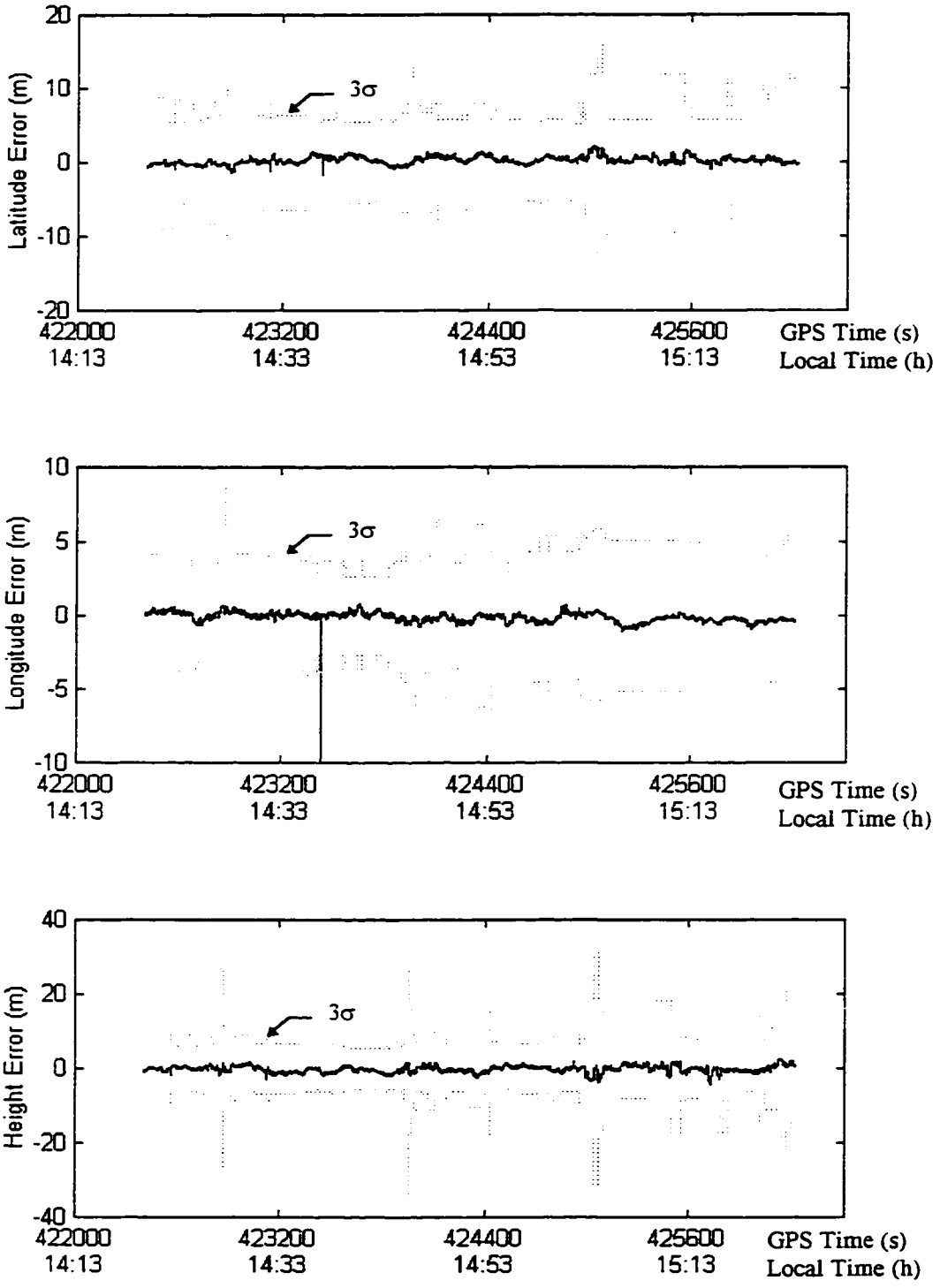

Figure 6.9 Position errors of unaided GPS, processed in differential pseudorange mode, Nose Hill test

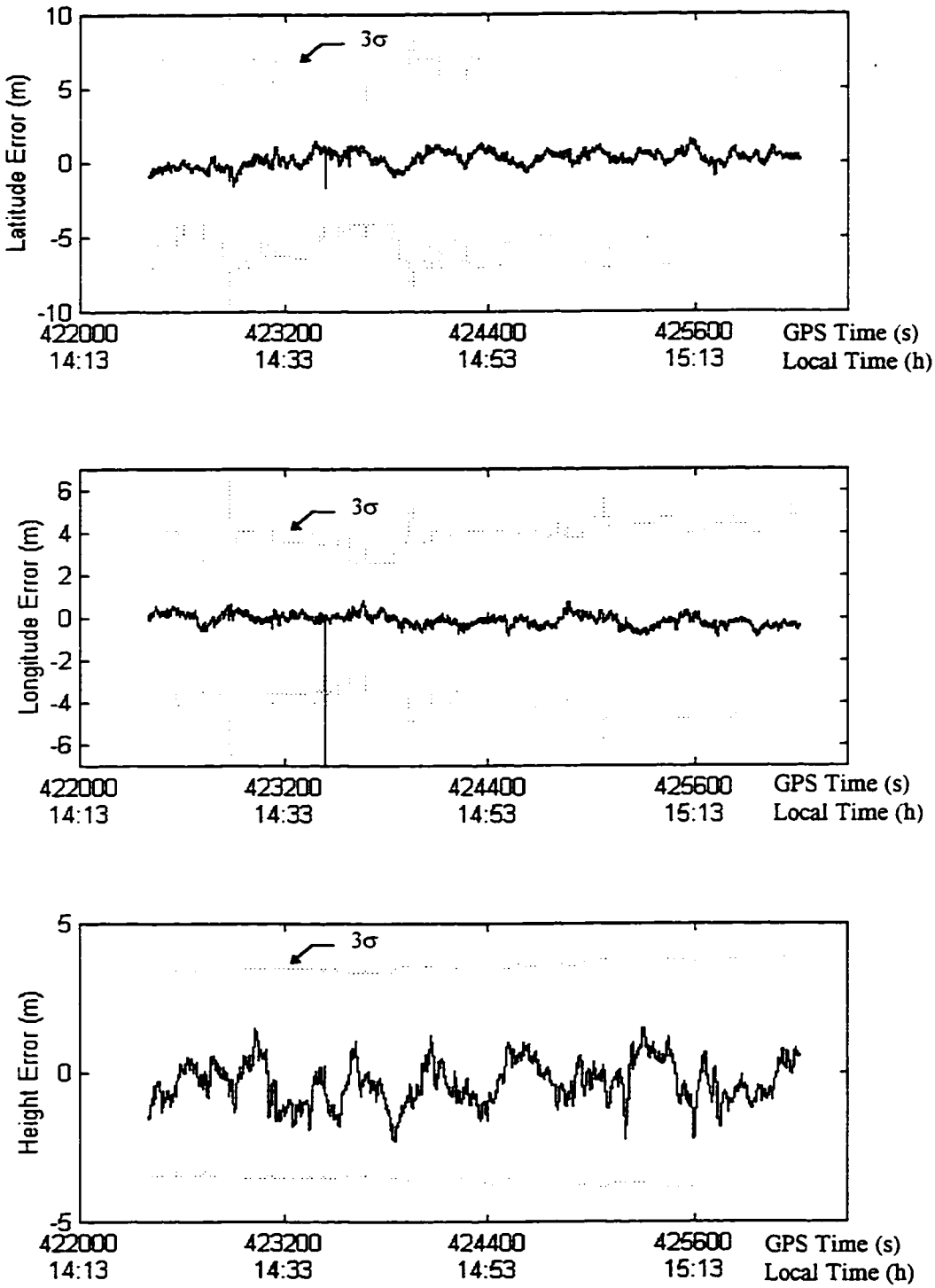

Figure 6.10 Position error of rubidium clock aided GPS, processed in differential pseudorange mode, with the accurate TCXO time base calculated using post-mission information at the reference station, Nose Hill test

6.1.3 Simulated downtown area

In urban environments, the buildings along the road mask satellite signals, thus GPS outages occur frequently. To simulate this environment, a virtual wall satellite rejection algorithm (Hayashi, 1996a) can be used. The basic concept of the algorithm is to build a virtual wall on each side of the road, as shown in the Figure 6.11. The walls block a part of the sky and mask the signals of some satellites.

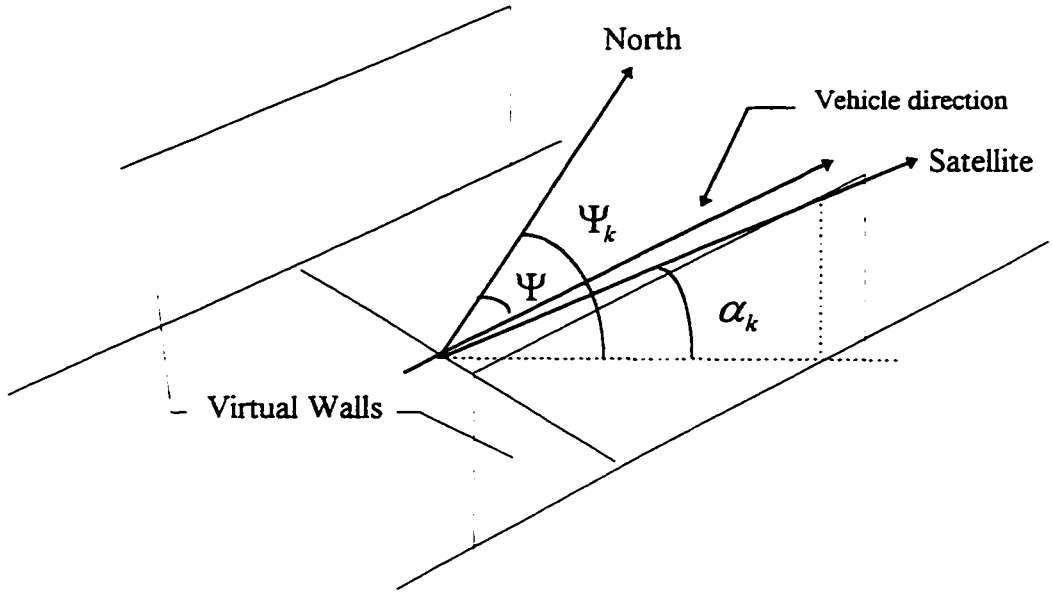

Figure 6.11 Basic concept of the virtual walls

Assume the vehicle goes along the central line of the road with heading Ψ. Given a cross-track cutoff angle α_c, the cutoff angle for the satellite with an azimuth of Ψ_k can be derived as:

$$\alpha_k = \tan^{-1}\left[\tan\alpha_c \cdot \sin\left|\Psi - \Psi_k\right|\right] \tag{6.1}$$

If the elevation of the satellite is less than the α_k, this satellite is assumed to be blocked by the walls and rejected by the algorithm. Since the test is aimed at inspecting the capability of the integrated navigation system for navigation using three or two satellites, a cross track cutoff angle of 70° was chosen, which corresponds to a wall height of 20 metres

with a cross track distance from the vehicle to walls of 7.5 metres. Figure 6.12 presents the number of visible satellites in the simulated downtown area using the Nose Hill test data. During most of the test, the number of visible satellites is two or three. Unaided GPS can provide position solutions only for a very short period of time (90 epochs out of 3800 epochs), during which four satellites can be seen.

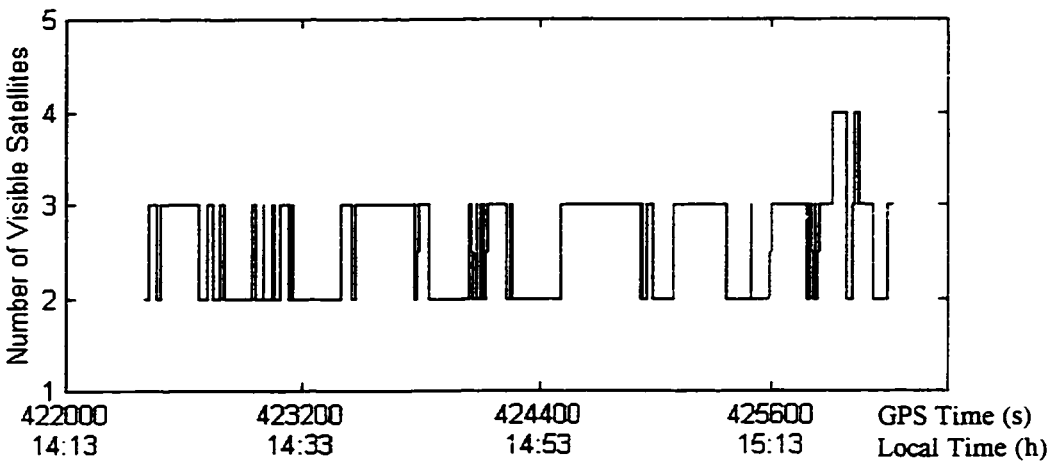

Figure 6.12 Number of visible satellites for the simulated downtown test

6.1.4 Rubidium clock aided GPS/barometer integration

All point positioning results in this section were computed by a navigation program developed by the author, which integrates rubidium clock aided GPS with the barometer using the Kalman filters described in Chapter 5. The data was processed in both stand-alone mode with post-mission information and differential mode. C/A code position solutions were computed each second using a satellite cutoff angle of five degrees. Before the vehicle entered the simulated downtown area, all the satellites in view in the controlled environment were tracked by the receiver to allow the rubidium clock aided GPS to estimate the clock offset and calibrate the barometer. After entering the simulated downtown area, the number of visible satellites fell to two or three, so the barometer error estimate was held fixed at the last estimated value.

Figure 6.13 presents the position errors of the integrated navigation system in stand-alone mode with post-mission information. The dashed envelopes are 3σ error envelopes derived from the master Kalman filter. The actual errors are within the estimated accuracy some 95% of the time, which constitutes a good indication that the error sources are modeled correctly in the Kalman filter. Tropospheric corrections were applied, and carrier phase smoothing of the pseudorange measurements was performed. Figure 6.14 presents the position errors of the integrated navigation system in differential mode. In this mode, carrier phase smoothing was not used. At the reference station, post-mission information was used to estimate the TCXO clock offset so that the clock offset error could be removed from the corrections. The same effect would have been obtained using a rubidium clock at the reference station with broadcast information. Table 6.4 summarizes the results.

Table 6.4 Statistics of the results for the rubidium clock aided GPS integrated with a barometer in the simulated downtown area

MEAN/RMS (m)

	LATITUDE	LONGITUDE*	HEIGHT
STAND-ALONE	3.23/4.24	1.06/4.97	2.08/3.17
DIFFERENTIAL	1.14/3.35	-0.10/5.38	-1.73/3.19

* Excluding the bias at 423436 seconds.

Rubidium clock aided GPS integrated with a barometer is able to navigate using two or three satellites in the entire simulated downtown area (3800 epochs), although the accuracy is reduced. It is noted that during the time when the number of visible satellites falls to two or three, the Kalman filter held the last barometric height bias obtained from the estimate of GPS height with good geometry (VDOP<5). The vertical accuracy of the integrated navigation system in this case is dependent upon the calibration accuracy, the barometric altitude accuracy and the clock offset estimate accuracy. For land vehicle navigation, the atmosphere and temperature are relatively stable in a local area. So the barometer performs well. In addition, horizontal errors show a strong correlation with the vertical error. If the accuracy of the barometric altitude could be improved, better

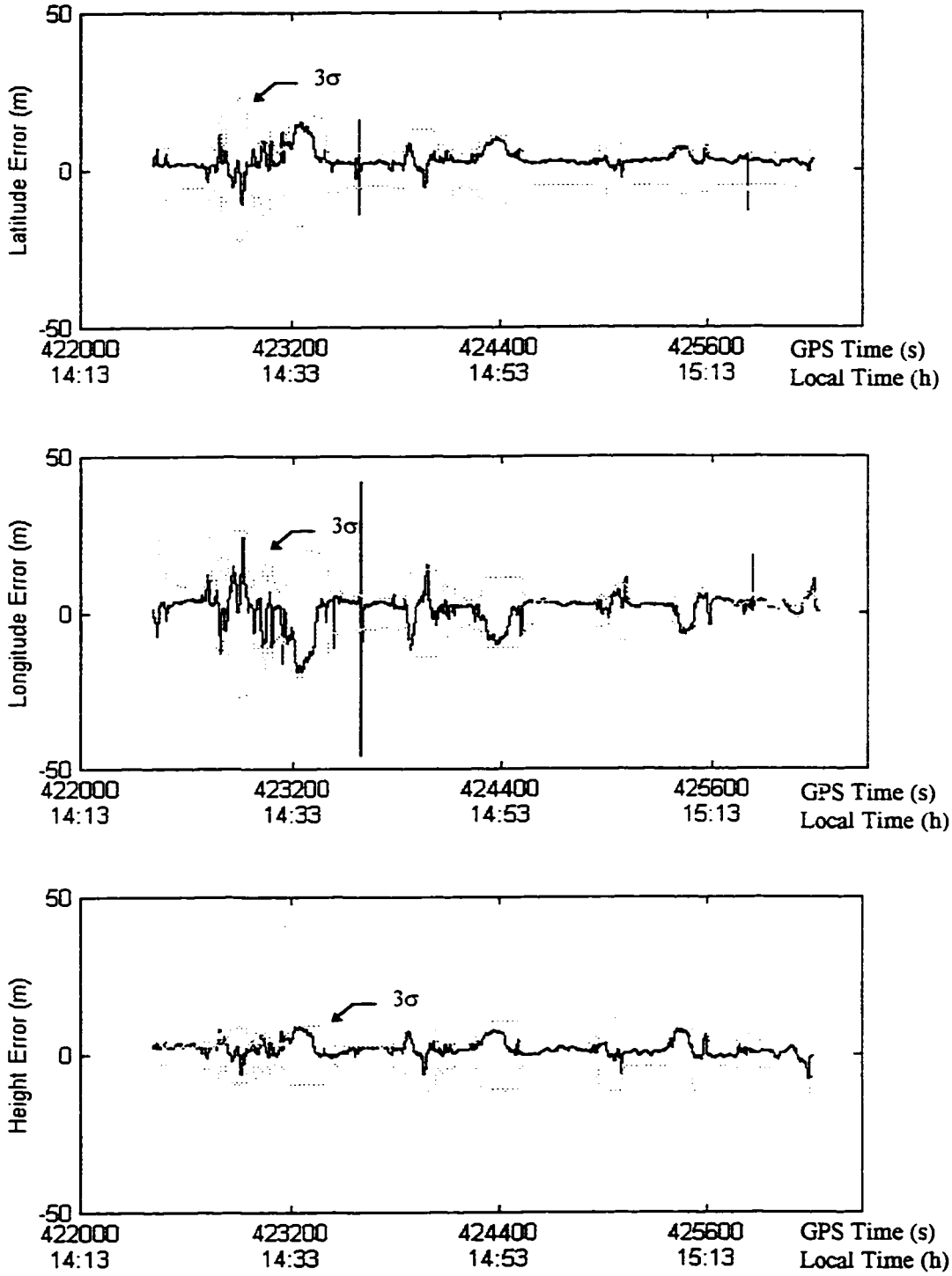

Figure 6.13 Position errors of the rubidium clock aided GPS integrated with a barometer in stand-alone mode with post-mission information, for the simulated downtown area (70° cut-off-across-track)

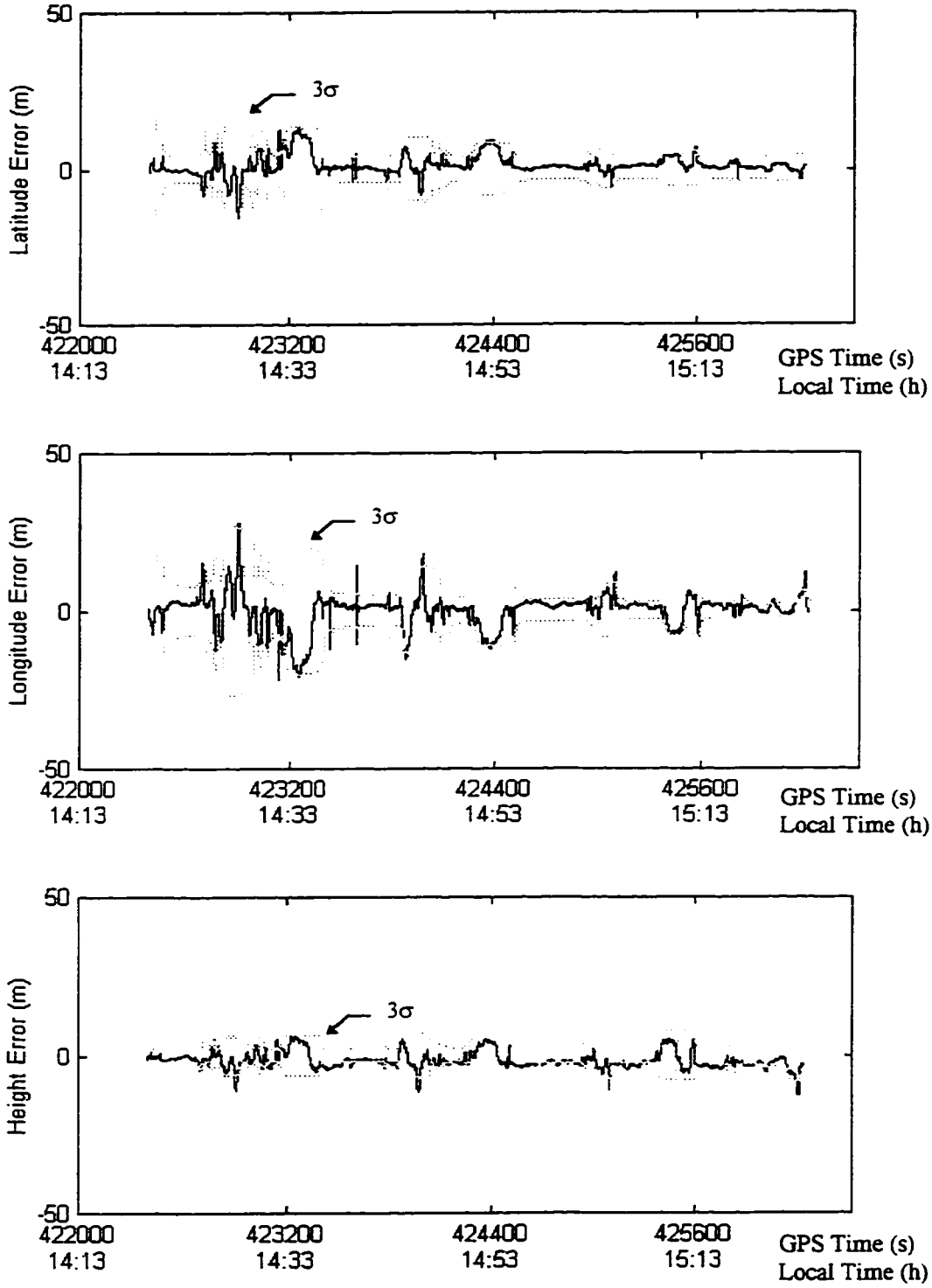

Figure 6.14 Position errors of the rubidium clock aided GPS integrated with a barometer in differential mode, in the simulated downtown area (70° cut-off-across-track)

horizontal accuracy would also be expected. While stand-alone GPS using post-mission information has similar positioning accuracy to differential GPS using corrections generated with post-mission information, the former has larger bias errors due to the ionosphere. Therefore, in the downtown test to be described later only DGPS will be used to demonstrate the performance of the navigation system.

6.1.5 Rubidium clock aided GPS/Barometer/gyro integration

As mentioned in Chapter 5, a gyro cannot measure the absolute heading until the corrections are applied from the GPS heading. The correction accuracy depends on the accuracy of the GPS heading, i.e., the vehicle's horizontal speed. To obtain an accuracy of 0.01 rad, the vehicle's horizontal speed must exceed 10 m/s. Figure 6.15 presents the vehicle's horizontal speed during the test.

Unlike the GPS position, which can be evaluated with a sub-decimetre accuracy by the reference position solution of the carrier phase measurements, very sophisticated and expensive equipment, such as high accuracy gyro compass and INS etc., are needed to evaluate the GPS heading. The GPS velocity can be evaluated in static mode without external equipment. The GPS heading, however, is treated as the heading reference when the vehicle's horizontal speed exceeds some value. The higher the vehicle's horizontal speed, the more accurate the GPS heading, provided that the accuracy of GPS velocity is the same in static mode as that in kinematic mode, which is a reasonable assumption under the dynamic considered herein (e.g. Cannon et al. 1997). Therefore, the time period of GPS time 422900 to 423800 second, during which the vehicle's horizontal speed is almost always more than 10 m/s, was chosen to evaluate the efficiency of the Kalman filter for the gyro.

The filter for the gyro does not compute the gyro heading until the calibration is applied from the GPS heading with satisfactory accuracy, when the vehicle's horizontal speed is high enough. The Kalman filter estimates the initial heading and measurement errors, then applies them to the gyro heading, i.e.:

$$\hat{\Psi}_g = \Psi_g - \hat{\Psi}_0 - \delta\hat{\Psi}_g \tag{6.2}$$

where $\hat{\Psi}_g$ is the calibrated gyro heading

$\hat{\Psi}_0$ is the estimated initial heading, and

$\delta\hat{\Psi}_g$ is the estimated gyro measurement error.

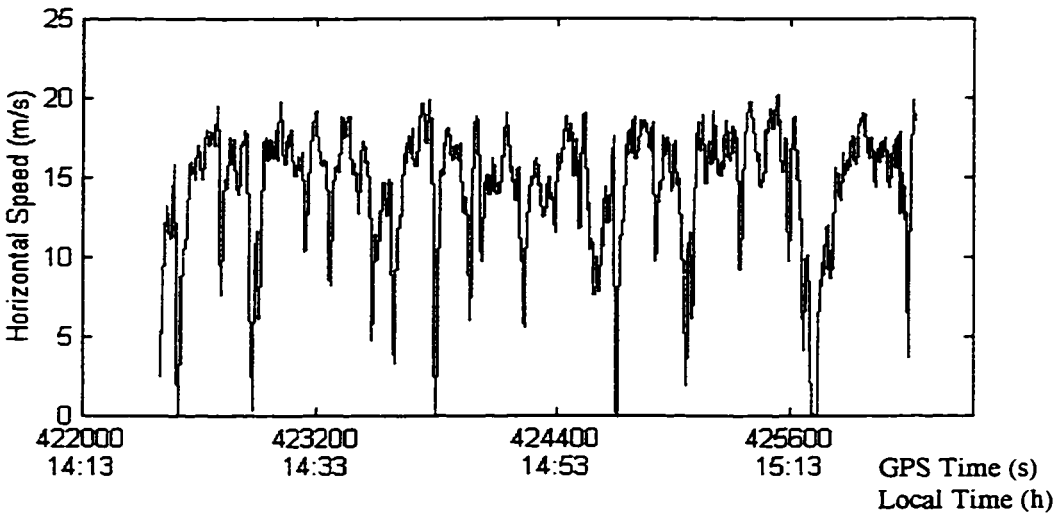

Figure 6.15 Horizontal speed of the vehicle during the Nose Hill test

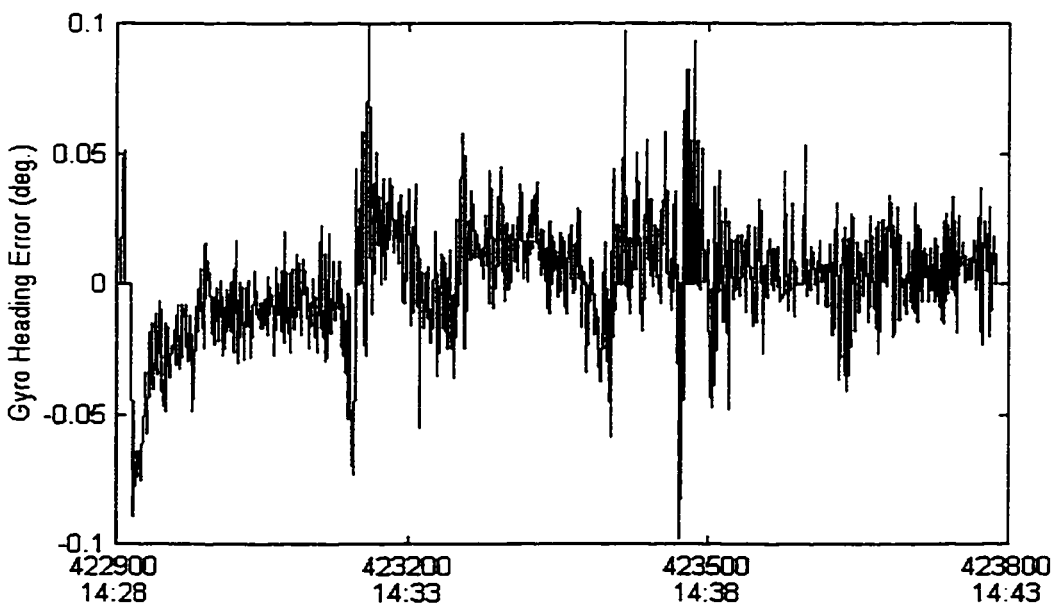

Figure 6.16 Calibrated gyro heading error using the GPS heading

Figure 6.16 presents the calibrated gyro heading error, which was computed using GPS heading as the reference heading as shown in Figure 6.17. The Kalman filter makes the gyro heading follow the GPS heading within 0.1 degree.

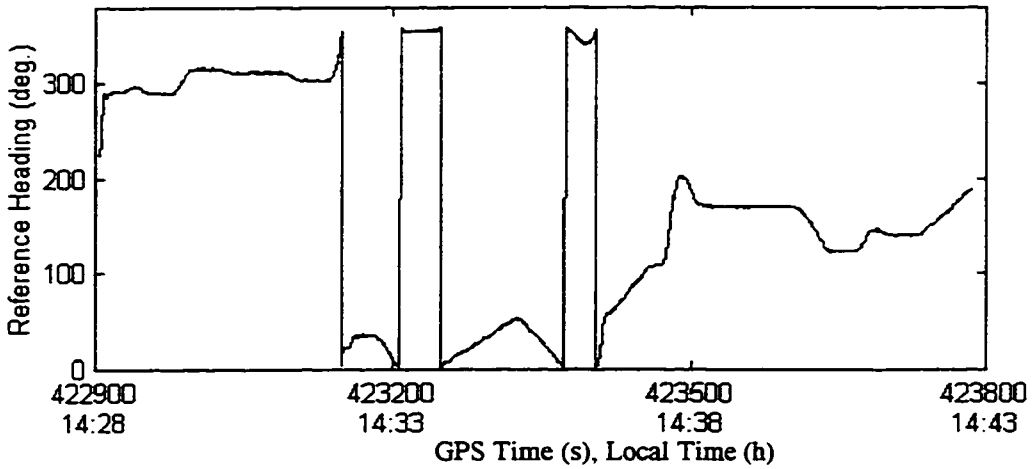

Figure 6.17 GPS heading computed using the GPS velocity

If the number of visible satellites falls to one after the gyro heading is calibrated by the GPS heading, the Kalman filter will predict the gyro heading error. Figure 6.18 shows the performance of the gyro in this situation. The gyro senses false heading rate due to severe variations in the vehicle's attitude so that the gyro heading appears to drift very fast. Figure 6.19 shows the reference height during the period. The vehicle was running on a slope during the period from 423030 to 423450 and the corresponding gyro drift can clearly be seen in Figure 6.18. Gyro drift is also correlated with heading changes as can be seen by comparing Figure 6.17 and 6.18.

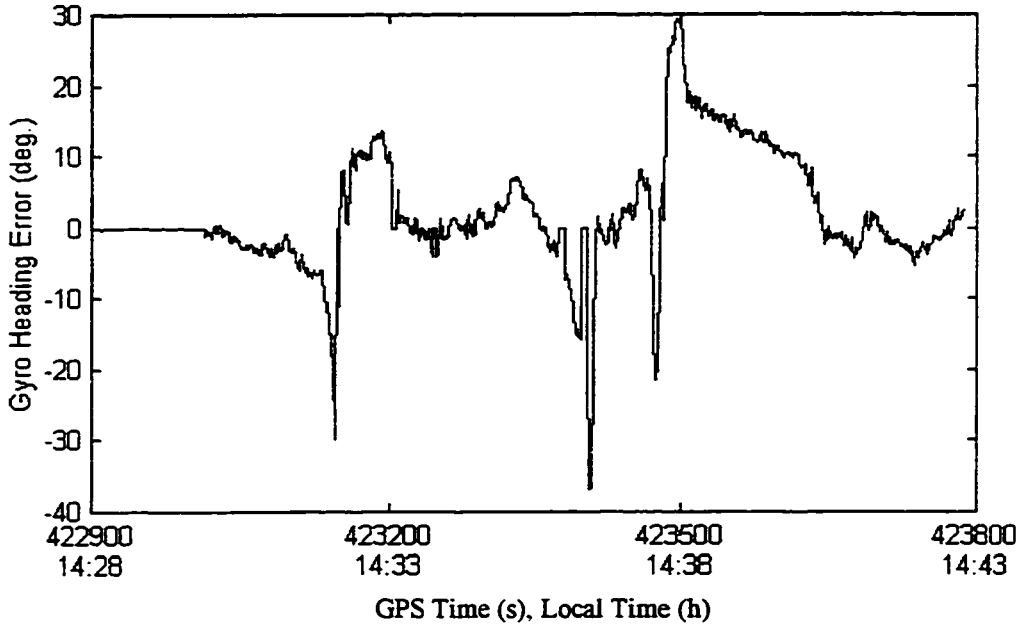

Figure 6.18 Performance of the gyro after it is calibrated by the GPS heading

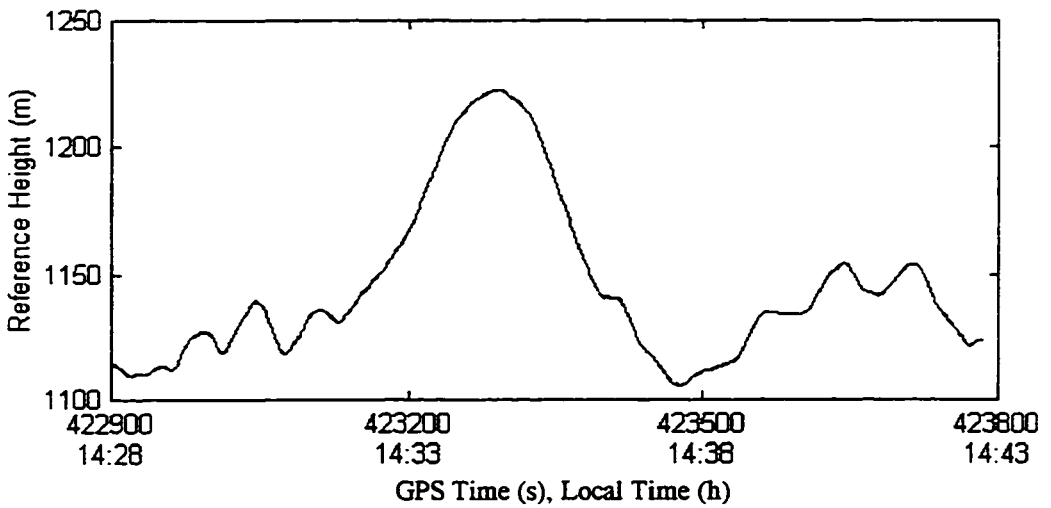

Figure 6.19 Reference height computed by FLYKIN™

The gyro heading rate error results from two sources: misalignment of the installation and the inclination of the vehicle. If the gyro is mounted on the vehicle with a misalignment angle α and misalignment azimuth angle β, and the vehicle has a heading rate ω_h, a pitch

rate ω_p and a roll rate ω_r, as shown in Figure 6.20, where the (x_v, y_v, z_v) is the vehicle frame coordinate system, the angular rate detected by the gyro is:

$$\omega_g = \omega_h \cos\alpha + H \sin\alpha \tag{6.3}$$

where $H = \omega_r \cos\beta + \omega_p \sin\beta$

Considering that the misalignment angle usually is small, one may write Eq. (6.3) as:

$$\omega_g = \omega_h + \alpha(\omega_r \cos\beta + \omega_p \sin\beta) \tag{6.4}$$

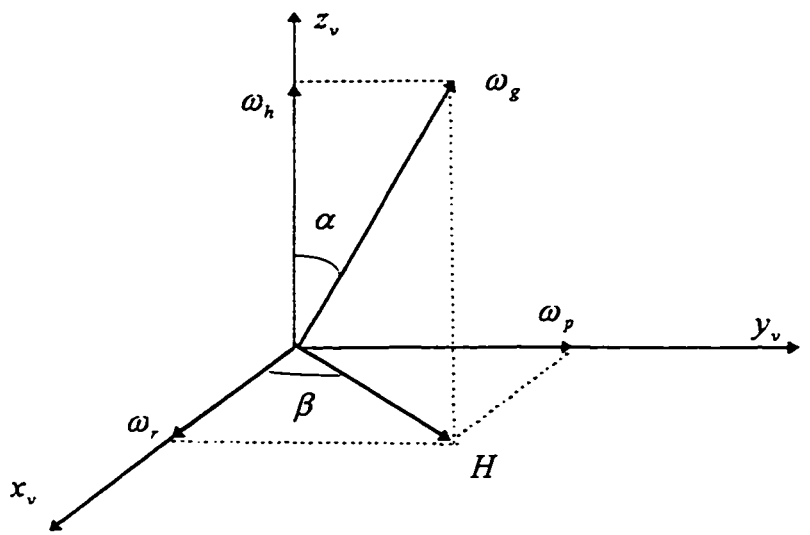

Figure 6.20 Misalignment of a gyro in a car

If the vehicle has a pitch angle of θ and a roll angle of γ, as shown in Figure 6.21, where (x, y, z) is the horizon coordinate system, one can write the real heading rate of the vehicle as:

$$\omega_z = \omega_{z'} \cos\theta - \omega_r \sin\theta \tag{6.5}$$

and $$\omega_{z'} = \omega_g \cos\gamma + \omega_p \sin\gamma \tag{6.6}$$

One may obtain:

$$\omega_z = \omega_g \cos\gamma \cos\theta + \omega_p \sin\gamma \cos\theta - \omega_r \sin\theta \tag{6.7}$$

If the roll and pitch angles are small, the gyro heading rate error can be expressed as:

$$d\omega = \omega_p(\gamma - \alpha\sin\beta) - \omega_r(\theta + \alpha\cos\beta) \tag{6.8}$$

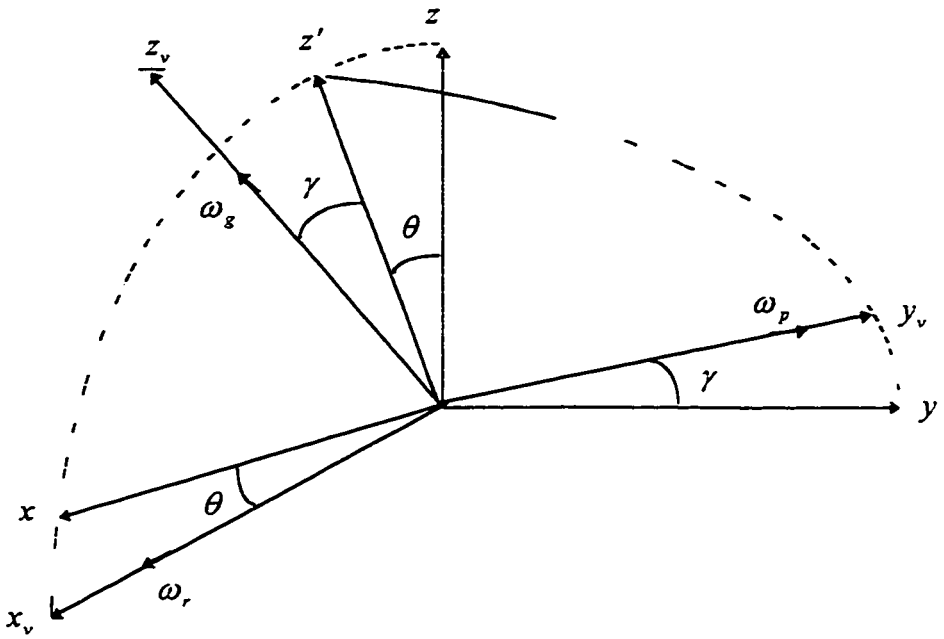

Figure 6.21 Inclination of the vehicle.

Usually, the sharper the turn on the road, the larger the incline angle of the road, thus, the larger the gyro heading error. Comparing Figure 6.17 with Figure 6.18, this situation is clearly visible. In downtown areas, however, the roads may be more level than the test road used herein. The performance of the gyro is therefore expected to be better in such areas.

Theoretically, rubidium clock aided GPS integrated with a barometer cannot navigate with only one satellite measurement. While the Kalman filter is able to predict the position based on the past measurements, it will diverge dramatically. Figure 6.22 presents the positioning error of the rubidium clock aided GPS integrated with a barometer when only one satellite is available.

But, the rubidium clock aided GPS integrated with a barometer and a gyro is able to navigate using only one satellite measurement as long as the gyro heading has been calibrated. Figure 6.23 shows the positioning error of the rubidium clock aided GPS integrated with a barometer and a gyro. Since the gyro drifts very fast due to the incline of the vehicle, the performance of the integrated system degrades rapidly with time.

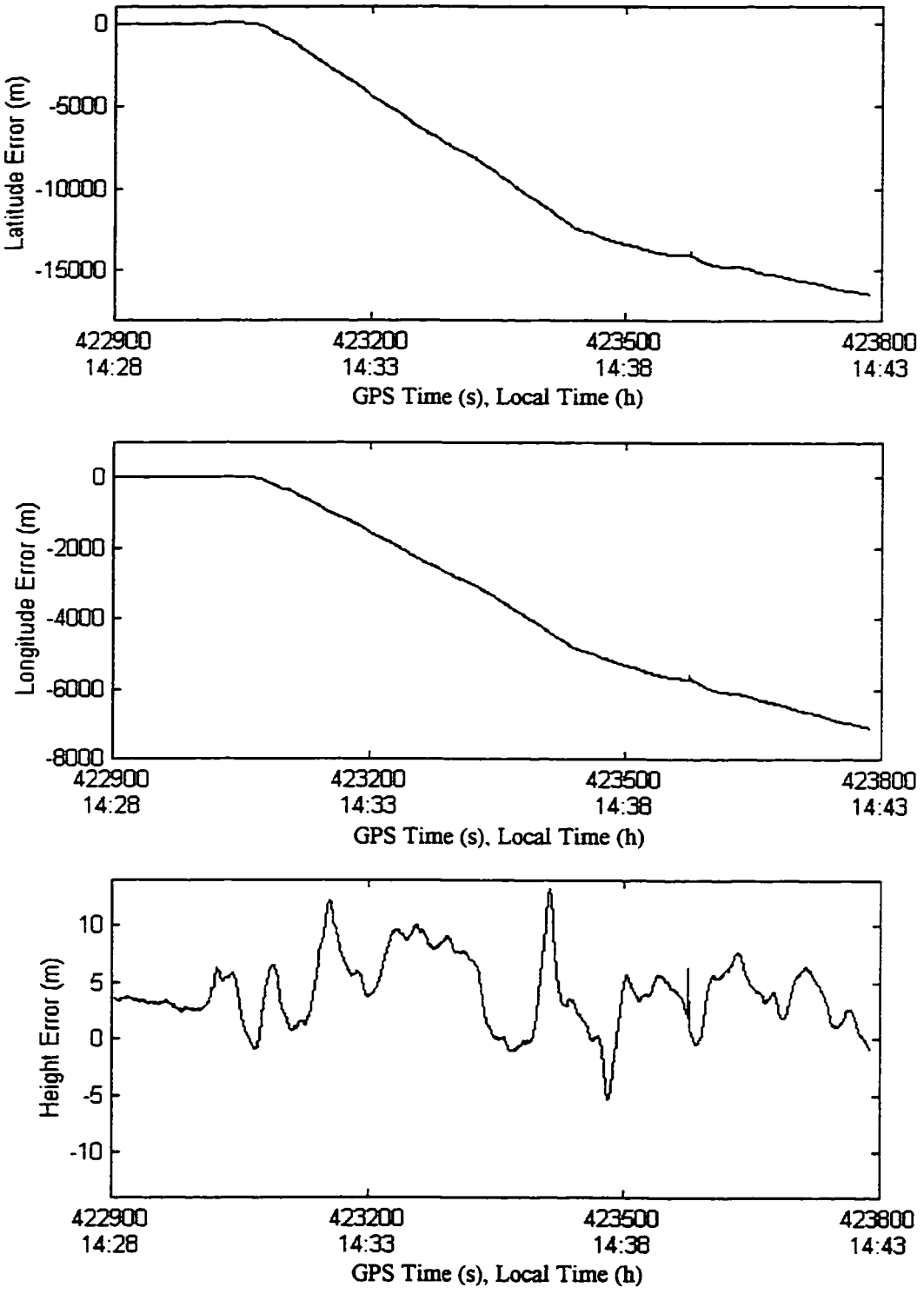

Figure 6.22 Positioning errors of the rubidium clock aided GPS integrated with a barometer using one satellite measurement

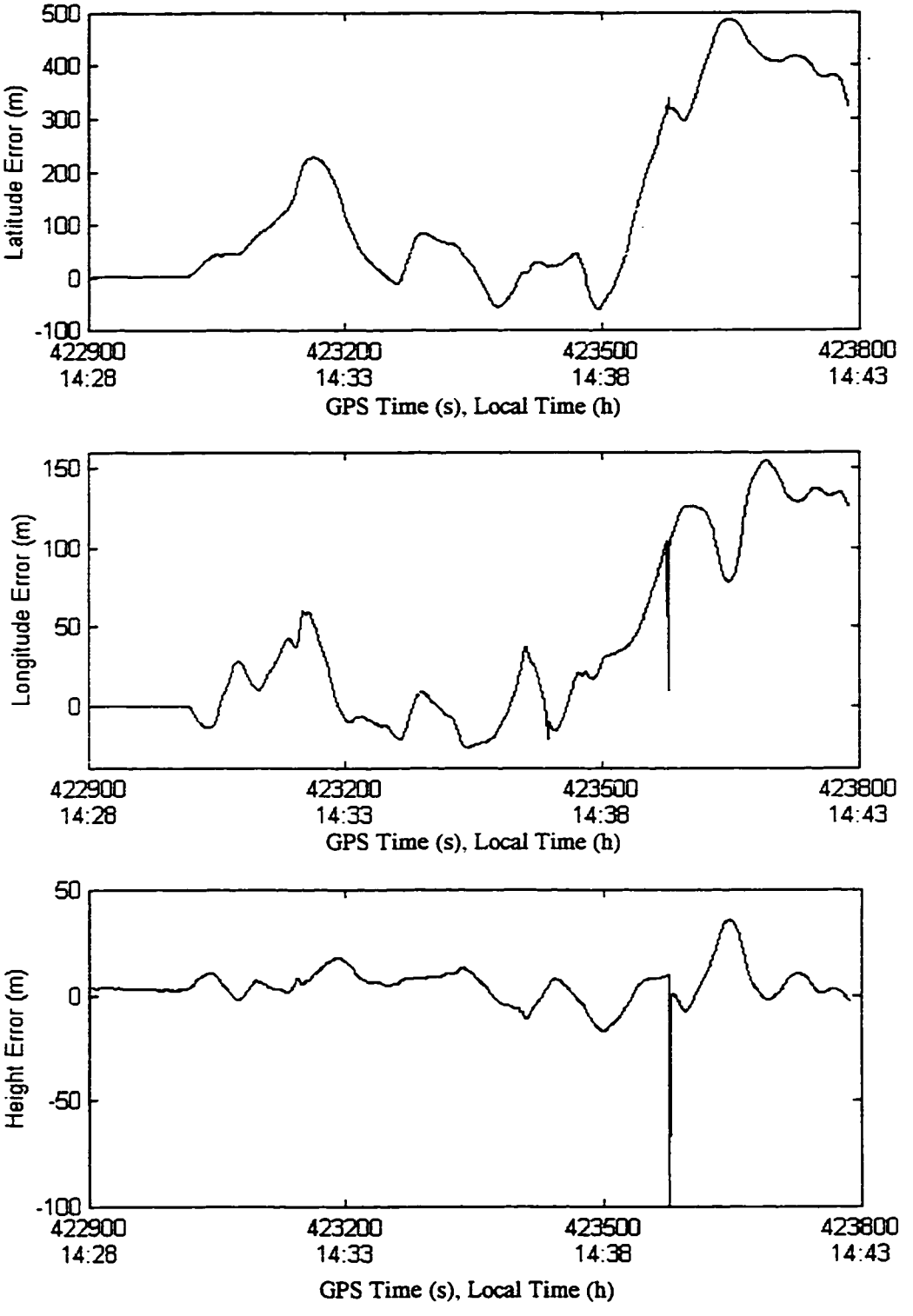

Figure 6.23 Positioning errors of the rubidium clock aided GPS integrated with a barometer and a gyro using one satellite measurement

6.2 Field Test in Downtown Area

6.2.1 Test description

A field test was carried out in downtown Calgary on April 6, 1997. The test time was deliberately selected from 5:50 to 7:05 a.m. to observe the performance of the navigation system under both the poorest and the best satellite geometry in a day, and avoid the heavy traffic. Figure 6.24 presents the number of visible satellites and Figure 6.25 the DOPs during the downtown Calgary test, with a cutoff angle of five degree. Repeating the same trajectory eight times enabled one to examine the repeatability of the navigation system derived trajectories. Each run time duration is shown in both Figure 6.24 and Figure 6.25 as well.

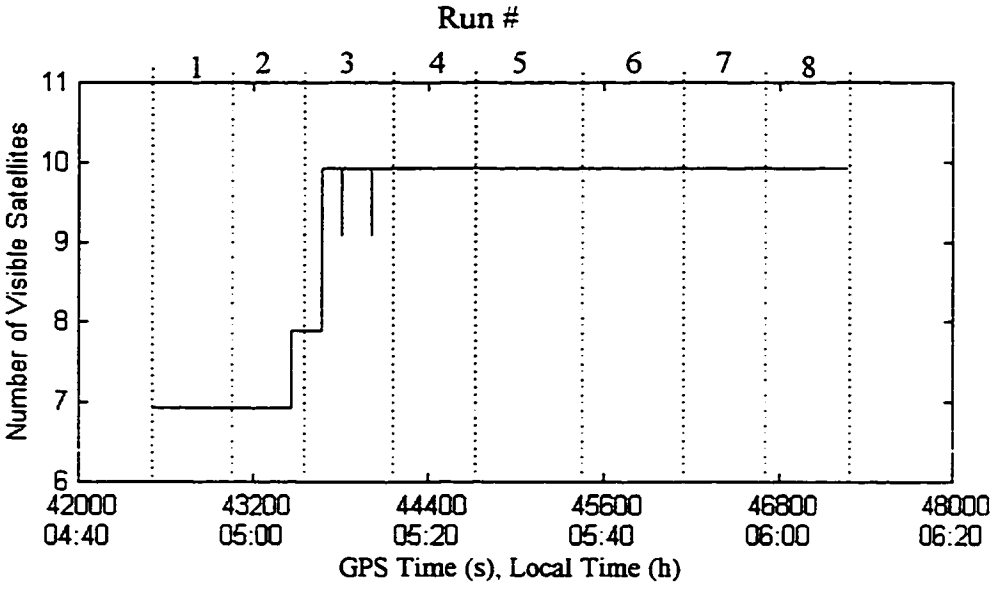

Figure 6.24 Number of available satellites during the downtown Calgary test

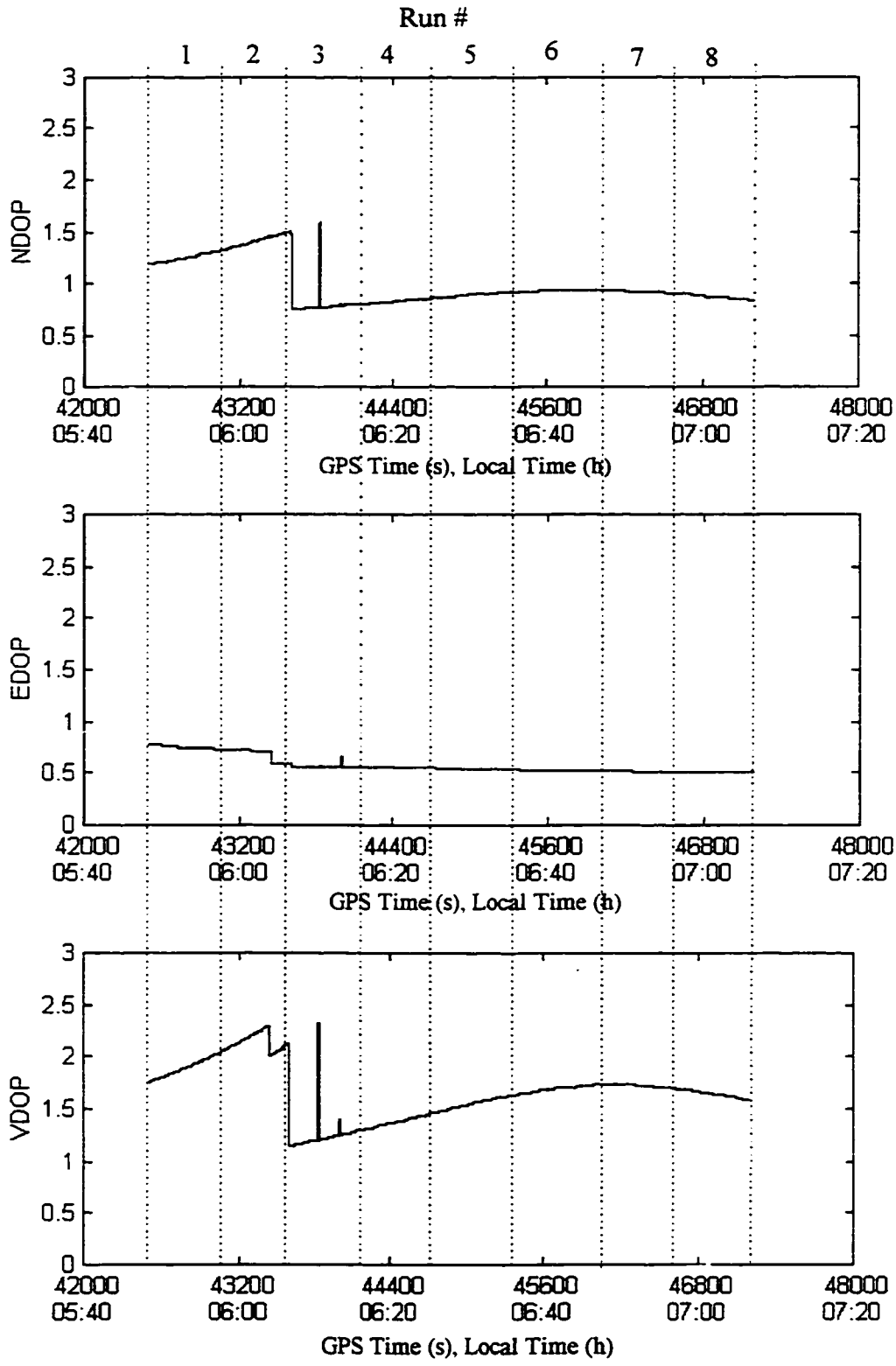

Figure 6.25 Satellite geometry during the downtown Calgary test using a mask angle of 5°

The test route, shown in Figure 6.26, was carefully chosen so that the navigation system encountered various severe environments, such as tall buildings (10-story or higher) on both sides of the road along 6th Avenue, Centre Street and 8th Street, tall buildings on one side but low buildings (3-story or lower) or trees on the other side of the road along part of Center Street, part of 8th Street and 7th Street, and only tall buildings and/or low buildings on one side of the road along 1st Avenue, 3rd Avenue and 4th street. The dashed line is the horizontal component of the trajectory. Eau Claire Avenue and 5th Street, where there are no buildings or trees along the road, were intentionally included to allow the GPS receiver to obtain at least four satellite measurements, so that the Kalman filter could calibrate the barometer and the gyro in every run.

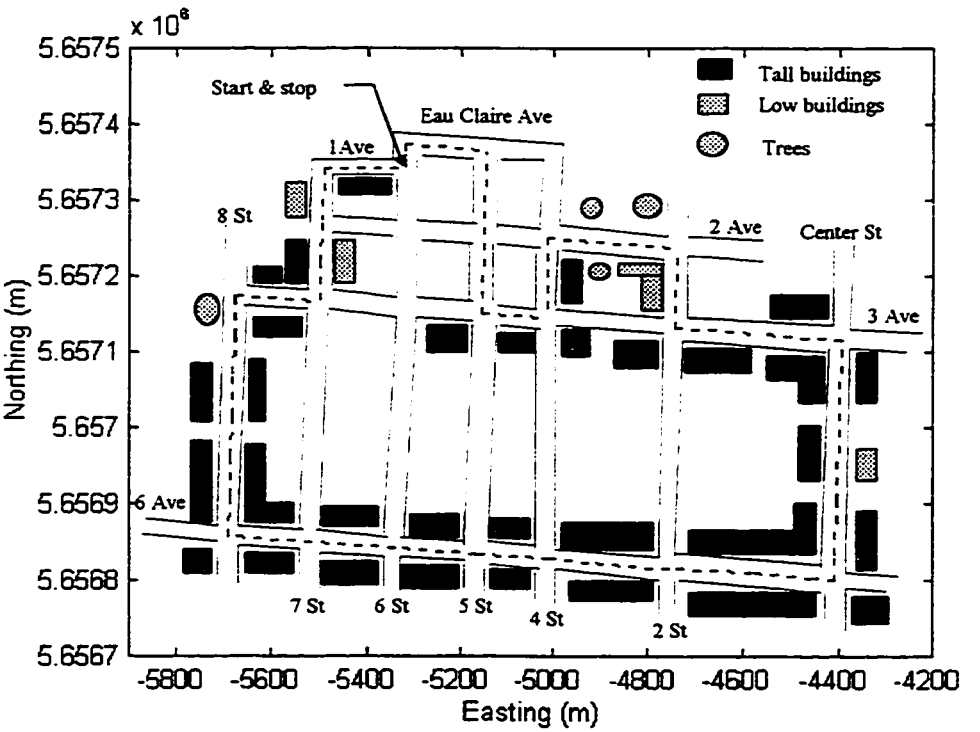

Figure 6.26 Test route, downtown Calgary test.

The navigation system was mounted on a vehicle. The antenna of the GPS receiver was installed on the roof of the vehicle. Another NovAtel GPSCard receiver equipped with a

TCXO clock was used as the reference station, placed on the roof of the Engineering Building at the University of Calgary, some 10 km away. The driving speed varied between 0 and 30 km/h and the 4-km trajectory required approximately 10 minutes to complete. L1 code, barometric pressure measurements and gyro heading rate measurements were collected at one second intervals over a period of 75 minutes.

Since the number of visible satellites, as shown in Figure 6.27, is less than four during most of the test runs, it is impossible to use carrier phase differential GPS to derive the reference trajectory. Instead, the horizontal component of the trajectory shown in Figure 6.26 derived from a digital map provided by the City of Calgary, was used to assess the GPS derived trajectory.

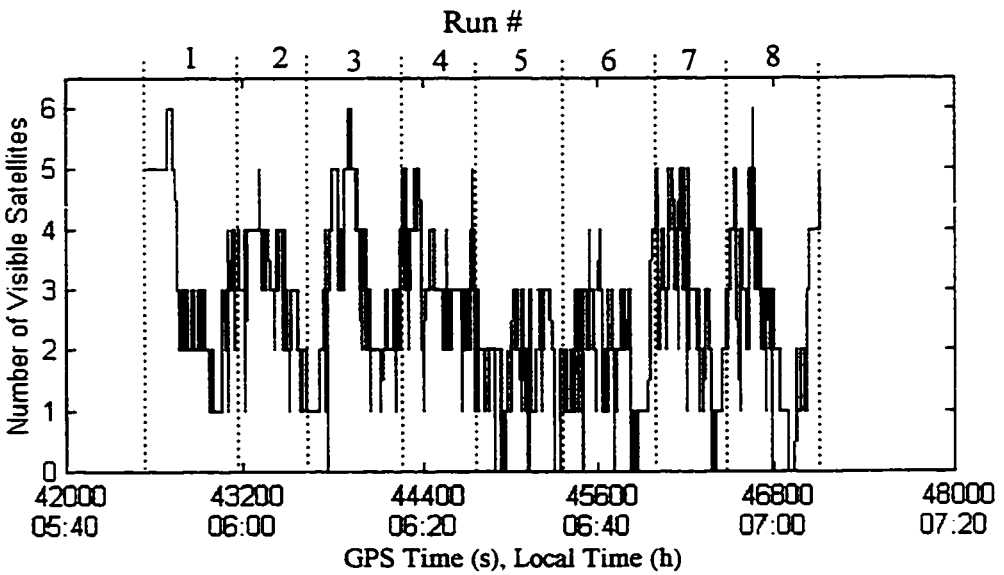

Figure 6.27 Number of visible satellites in the downtown Calgary test

Although the accuracy of the digital map is approximately 5 metres in downtown Calgary, the reference trajectory can only check the across track error and consistency of the position solutions. The GPS position solutions are, therefore, transformed into UTM coordinates in accordance with the digital map.

The solutions were computed in differential mode using a satellite cutoff angle of five degree and broadcast ephemerides and satellite corrections. However, post-mission information was used to derive an accurate time base with the TCXO clock at the reference station. The processing interval was one second. Neither tropospheric corrections nor carrier phase smoothing of the pseudorange measurements were applied. The navigation system was designed to be modular, and as such the data was processed in the following ways, namely

- unaided GPS
- rubidium clock aided GPS
- GPS/barometer integration
- rubidium clock aided GPS/barometer integration
- GPS/barometer/gyro integration, and
- rubidium clock aided GPS/barometer/gyro integration,

to examine the performance of the navigation system in different modes.

6.2.2 Unaided GPS

The unaided GPS point solutions were computed with C^3NAV^{TM}, which requires at least four satellite measurements. Figure 6.28 presents the horizontal components of the positioning solutions in run #1. Along Eau Claire Avenue and 5th Street, there is clear view to the sky. The receiver could therefore obtain enough measurements and the GPS positioning solutions are consistent with the reference trajectory. On 1st Avenue, there were several epochs when the receiver had enough measurements. The deviation of the GPS solutions from the reference trajectory is believed to be the result of multipath,

noting that there is a tall building on the southern side of the road. Unaided GPS was not possible in other sections of the route.

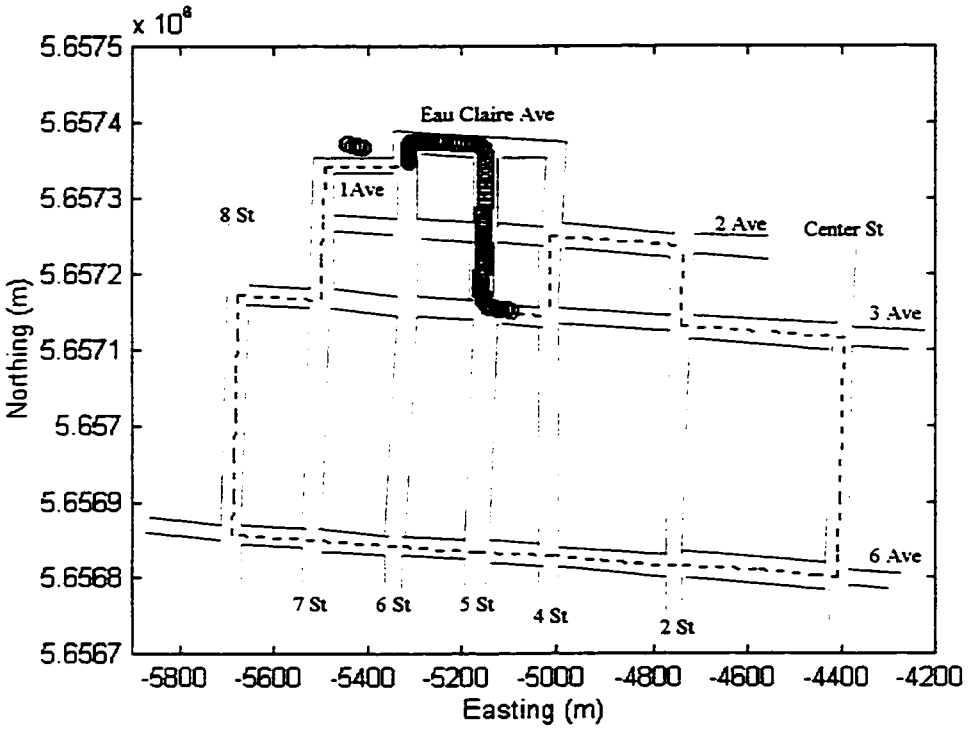

Figure 6.28 Horizontal trajectory using unaided GPS, downtown Calgary test, run #1

6.2.3 Rubidium clock aided GPS

The results in this and the following sections were computed using the navigation program, which implements the integration of rubidium clock aided GPS with a barometer and a gyro. The navigation mode was set as 'clock aiding' and the minimum number of satellite required for navigation was set to three. The availability is increased by quite a few epochs, amounting to availability almost twice the distance of unaided GPS, as shown in Figure 6.29.

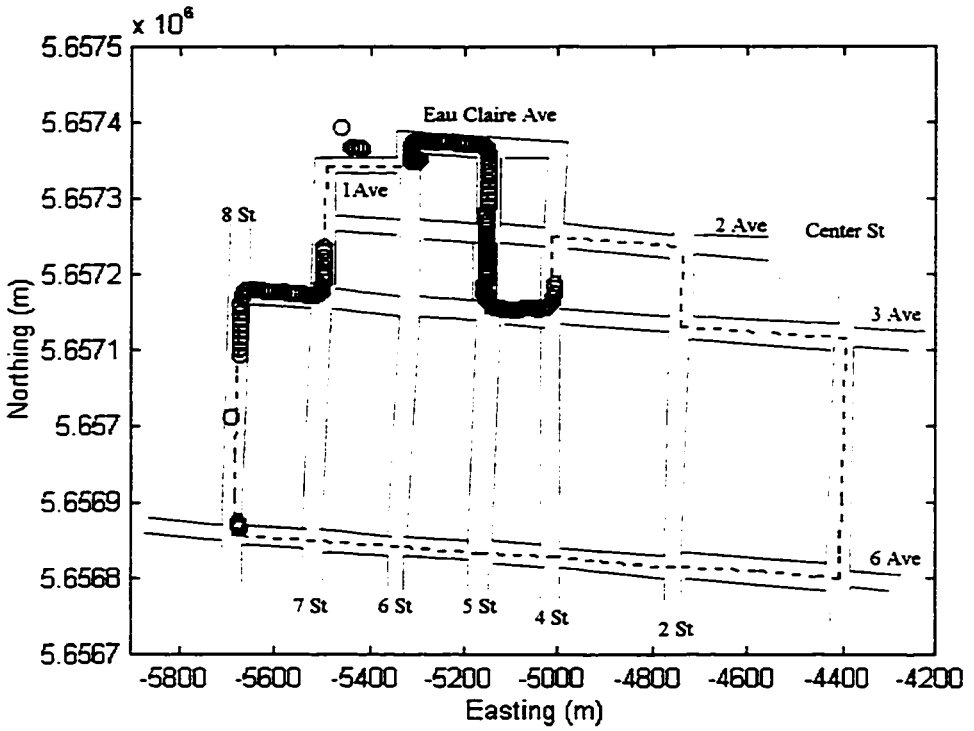

Figure 6.29 Horizontal trajectory by the rubidium clock aided GPS, downtown Calgary test, run #1

6.2.4 GPS/barometer integration

The navigation program was set in the mode of 'GPS + barometer' and the minimum number of satellite required for navigation was set to three. When the number of visible satellites is more than three and the VDOP is less than 5, the Kalman filter calibrates the barometer with GPS measurements. When the number of visible satellites falls to three or the VDOP becomes larger than 5, the Kalman filter predicts the barometric height error based on the past measurements. Figure 6.30 presents the estimated horizontal trajectory of GPS integrated with a barometer. The trajectory is similar to that of Figure 6.29 due to the high correlation between clock and the height component.

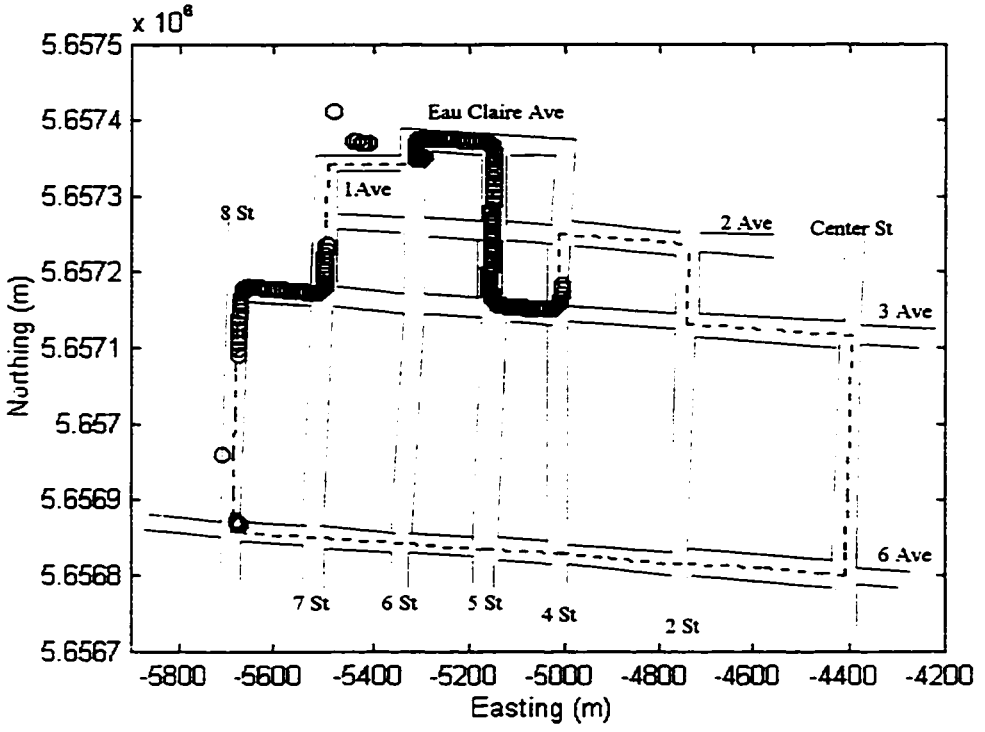

Figure 6.30 Horizontal trajectory using GPS integrated with a barometer, downtown Calgary test, run #1

6.2.5 Rubidium clock aided GPS/barometer integration

The navigation program was set in the mode of 'clock aided GPS + barometer' and the minimum number of satellites required for navigation was set as two. When the number of visible satellites is more than two and the VDOP is less than 5, the Kalman filter will calibrate the barometer with GPS measurements. When the number of visible satellites falls to three or the VDOP is larger than 5, the Kalman filter will predict the barometric height error basing on the past measurements. Figure 6.31 presents the estimated horizontal trajectory of the rubidium clock aided GPS integrated with a barometer. Figure 6.32 shows the estimated position standard deviations derived by the master Kalman filter.

The position availability is increased significantly since the required number of satellites is reduced to two. At the corner of 3rd Avenue and Center Street, the corner of 6th Avenue

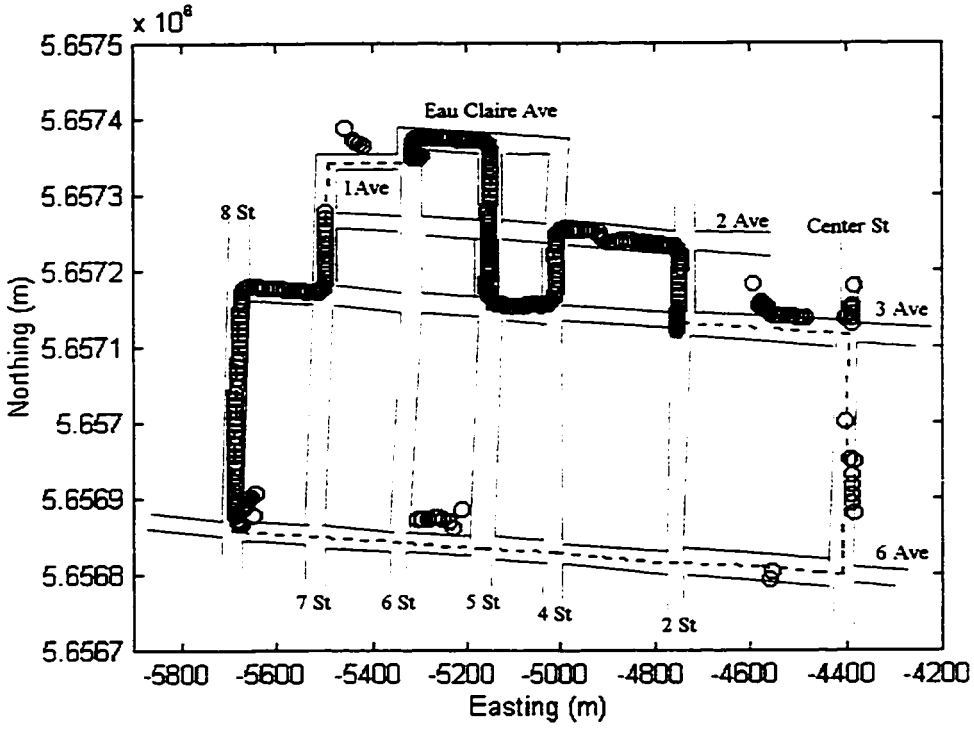

Figure 6.31 Horizontal trajectory using the rubidium clock aided GPS integrated with a barometer, downtown Calgary test, run #1

and 8th Street and on 6th Avenue, the cross track error is apparent. The error is believed to be the combination of the estimation error and multipath. The variances of the barometric height measurement and the clock offset measurement were all set as 1.0 m^2, that is, the height solutions were mainly decided by the barometer and the clock measurements. The horizontal solutions, however, were also affected by the satellite constellation and pseudorange measurements. This is shown in Figure 6.32. Since the reference trajectory was not available for this test, the position errors' standard deviation can be used to evaluate the accuracy of the navigation system during the test. If the error sources are modeled correctly as shown in Figure 6.13 and 6.14, the position error should not exceed 30 m within 95% time when the navigation system was available.

6.2.6 GPS/barometer/gyro integration

The navigation program was set in the mode of 'GPS + barometer + gyro' and the minimum number of satellites required for navigation was set as two. When the number of visible satellites is more than three and the VDOP is less than 5, the Kalman filter

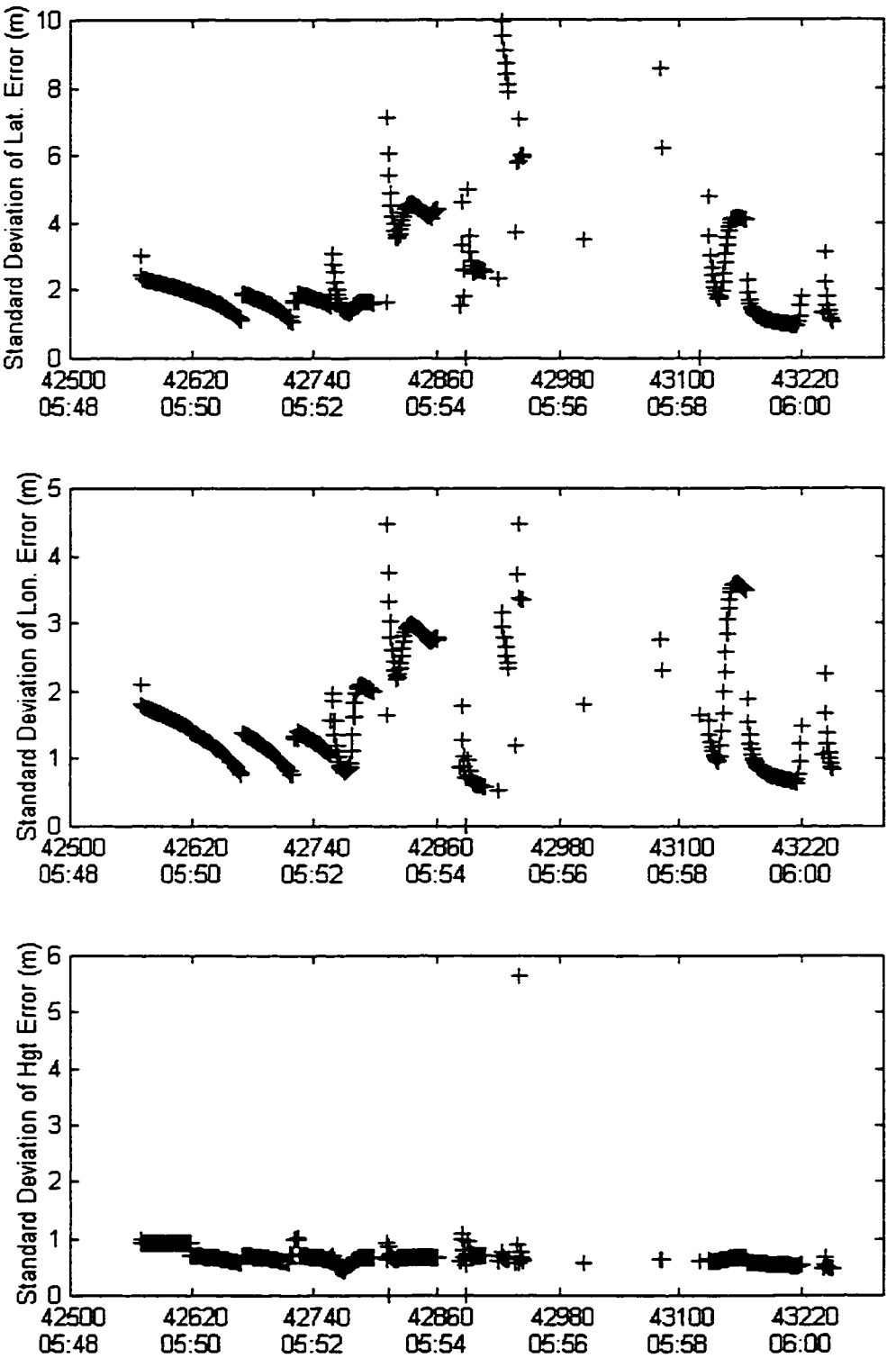

Figure 6.32 Position standard deviations, derived by the master Kalman filter in the mode 'clock aided GPS + Barometer'

calibrates the barometer with GPS measurements. When the number of visible satellites falls to three or the VDOP is larger than 5, the Kalman filter predicts the barometric height error based on the past measurements. For the gyro, when the number of visible satellites is more than two and HDOP is less than 5, the Kalman filter calibrates the gyro.

When the number of visible satellites falls to two or the HDOP is more than 5, the Kalman filter predicts the gyro heading error based on the past measurements. Figure 6.33 presents the estimated trajectory of GPS integrated with a barometer and a gyro.

The navigation availability in this mode is nearly the same as that in the mode of 'clock aided GPS + barometer'. The cross track error in this mode is obviously larger considering the gyro's drift due to the inclination of the vehicle during turning. Since the position estimate based on gyro heading measurements is propagated from the past position

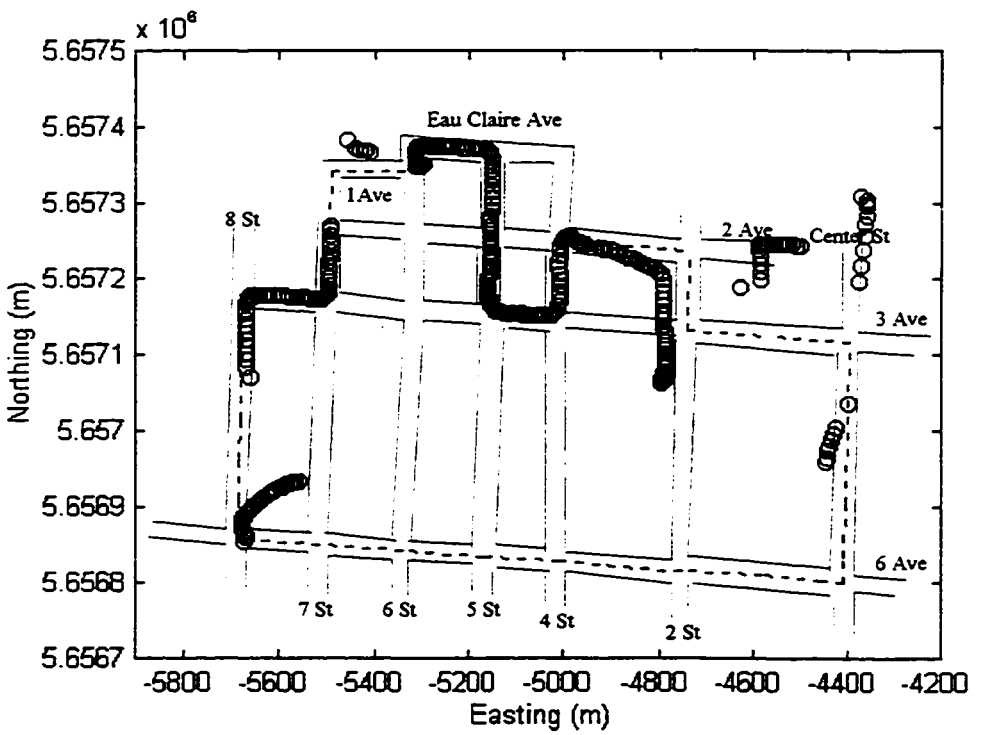

Figure 6.33 Horizontal trajectory using GPS integrated with a barometer and a gyro, downtown Calgary test, run #1

estimate, the gyro's heading error will result in significant cross track error. The estimated trajectories on 2nd Avenue and 8th Street show the obvious gyro heading error. The position estimates around the corner of 3rd Avenue and Centre Street have so large cross track errors that they are almost useless.

6.2.7 Rubidium clock aided GPS/barometer/gyro integration

The navigation program was set in the mode of 'clock aided GPS + barometer + gyro' and the minimum number of satellites required for navigation was set as one. When the number of visible satellites is more than two and the VDOP is less than 5, the Kalman filter calibrates the barometer with GPS measurements. When the number of visible satellites falls to two or the VDOP is larger than 5, the Kalman filter predicts the barometric height error based on the past measurements. For the gyro, when the number of visible satellites is more than one and the HDOP is less than 5, the Kalman filter

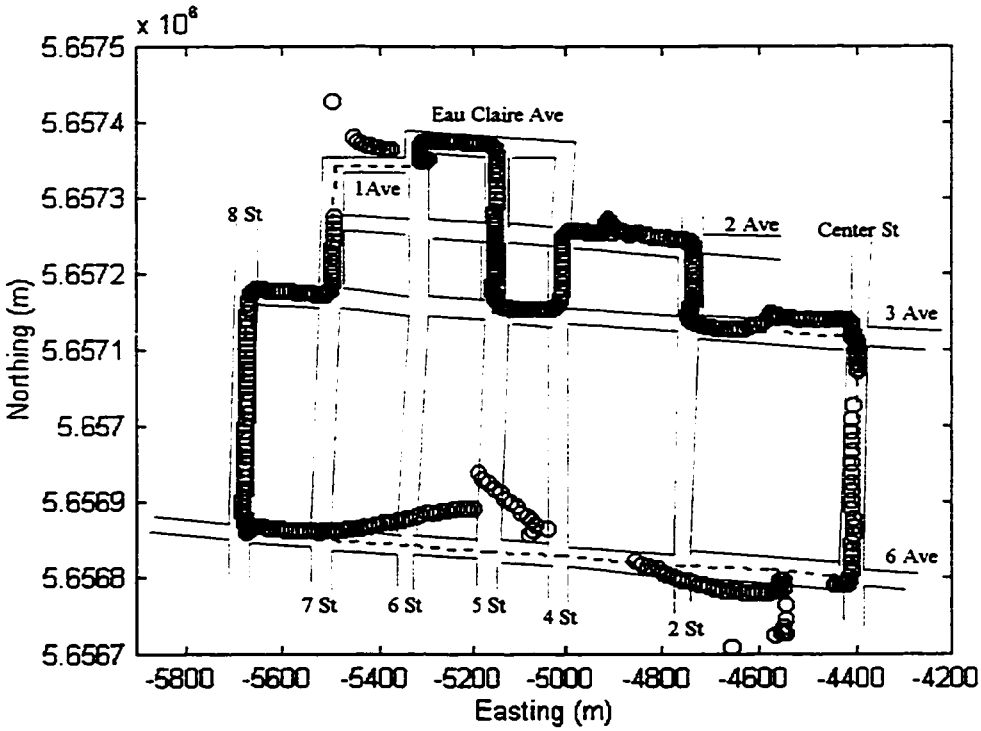

Figure 6.34 Horizontal trajectory using the rubidium clock aided GPS integrated with a barometer and a gyro, downtown Calgary test, run #1

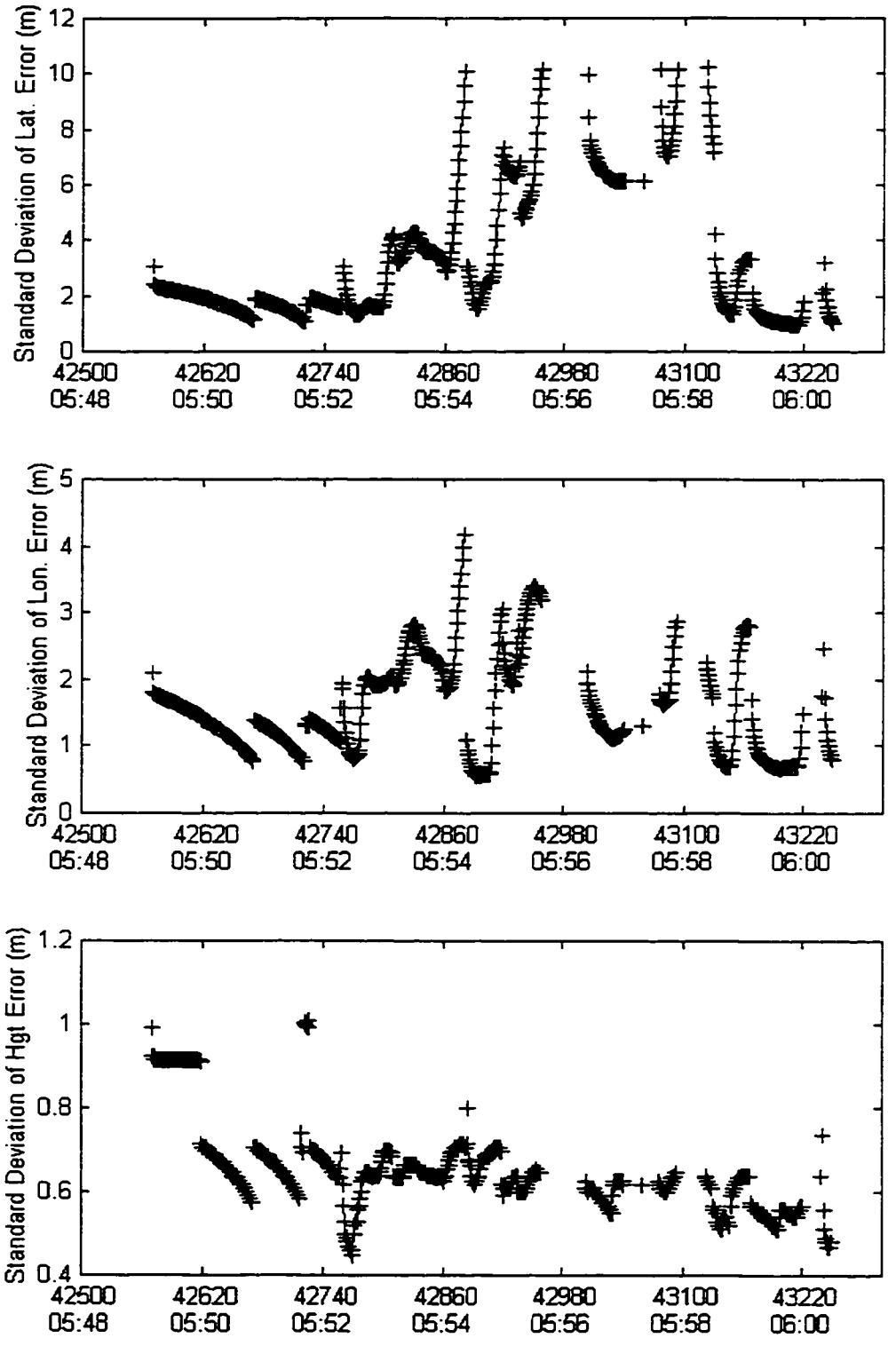

Figure 6.35 Position standard deviations, derived by the master Kalman filter in the mode 'clock aided GPS + Barometer + Gyro'

calibrates the gyro. When the number of visible satellites falls to one or the HDOP is more than 5, the Kalman filter predicts the gyro heading error based on the past measurements. Figure 6.34 presents the estimated trajectory of rubidium clock aided GPS integrated with a barometer and a gyro.

The position availability is increased to 90% in terms of time and distance. Rubidium clock aided GPS integrated with a barometer provides better accuracy and more availability than GPS integrated with a barometer does. The gyro, thus, had more chances to be calibrated with higher accuracy. On the other hand, the calibrated gyro improves the position estimate at the corner of 3rd Avenue and Center Street, and the corner of 6th Avenue and 8th Street. Figure 6.35 shows the estimated position standard deviations derived by the master Kalman filter. The results are similar to those obtained in Figure 6.32.

6.2.8 Summary of the downtown Calgary test

Results for the other runs are presented in Appendix A. In run #5 and #6 there were not enough satellites for GPS to calibrate the rubidium clock, the barometer and the gyro, and thus the Kalman filters diverged. Results of these two runs are not included.

Rubidium clock aided GPS and GPS/barometer integration have nearly the same availability and similar accuracy, because the test route is relatively flat and the barometer could give better height measurements after correction. While rubidium clock aided GPS/barometer integration and GPS/barometer/gyro integration have similar availability, the performance of the later depends on the gyro's performance when the number of satellites in view falls to two. In run #2, GPS/barometer/gyro integration provides better solutions at the corner of 4th Street and 2nd Avenue. In run #3, gyro drift is obvious from the solution of GPS/barometer/gyro integration at the corner of 3rd Avenue and Center Street. In run #4, the solution of rubidium clock aided GPS/barometer integration on 6th Avenue has a large cross road bias, which is believed to be due to multipath; the solution of GPS/barometer/gyro has a smaller cross road bias, because of good gyro performance during the period. In run #7, rubidium clock aided GPS/barometer integration and

GPS/barometer/gyro have similar solutions. In run #8, the solution of GPS/barometer/gyro was degraded by the gyro drift. Of all the integration modes, rubidium clock aided GPS/barometer/gyro integration provides the best availability as expected.

Table 6.5 summarizes the navigation availability of the navigation system in different modes for the six test runs described above and the sum thereof. Figure 6.36 shows the availability of the navigation system in different modes for the summary of all test runs described above. Rubidium clock aiding improves the navigation availability significantly.

Table 6.5 Summary of results

	Navigation Availability (%)						
Navigation Mode	run #1	run #2	run #3	run #4	run #7	run #8	Total
Unaided GPS	29	13	17	6	13	13	16
Clock Aided GPS	39	32	26	27	31	23	31
GPS + Barometer	39	31	31	27	31	25	31
Clock Aided GPS + Barometer	65	51	54	56	67	48	57
GPS + Barometer + Gyro	62	50	47	45	55	41	50
Clock Aided GPS + Barometer + Gyro	92	79	63	73	86	67	74

As mentioned in section 6.2.5, an exact reference trajectory was not available for the test. While the position errors' standard deviation can be used to evaluate the accuracy of the navigation system, the assumption made in section 6.2.5 still needs to be verified. The reliable means is to use another set of position sensors with reasonable accuracy to evaluate the navigation system studied herein.

While the rubidium clock, barometer and rate gyro used herein are expensive ($8,000 USD for the clock, $1,000 USD for the gyro and $800 USD for the barometer), the thesis objective is to explore the potential of augmenting GPS with these sensors. Cheaper sensors are available in market, such as $2,000 - $4,000 rubidium clocks and $20 - $100 gyros and barometers. Those sensors are suitable for commercial use.

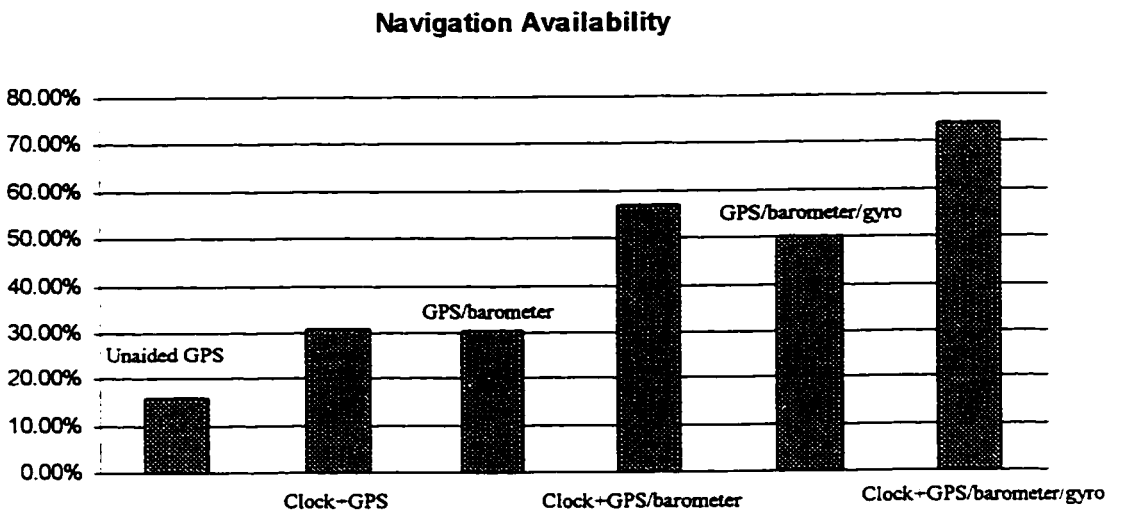

Figure 6.36 Navigation availability in different modes

CHAPTER 7
CONCLUSIONS AND RECOMMENDATIONS

7.1 Conclusions

The rubidium clock is a sufficiently stable and precise clock for GPS navigation. It allows us to obtain a better receiver clock offset estimate from the GPS measurements, when the rubidium clock is utilized as the receiver's oscillator. Thus, rubidium clock aiding significantly improves positioning accuracy. The improvement depends upon the correlation between the clock offset error and position errors and the improvement in the estimation of the clock offset. In general, the poorer the satellite geometry, the more correlated the clock offset error with the position errors, thus, the more likely the position accuracy can be improved. With a good satellite geometry, rubidium clock aided GPS is able to achieve a height accuracy similar to or better than the horizontal accuracy.

The rubidium clock drift is nearly linear. An adaptive low-pass filter, therefore, can be used to estimate the clock offset from the GPS measurements. The laboratory experiments and field trials have shown that the clock constrained GPS algorithm, which employs the adaptive low-pass filter, is able to improve the positioning accuracy. Its effect is especially beneficial for land vehicle navigation, which often encounters positioning error spikes due to sudden changes in the number of visible satellites and poor satellite geometry. The clock constrained GPS algorithm developed herein processes the data sequentially, thus it only needs the last measurement. It is a fast and practical navigation algorithm.

In addition to the rubidium clock, augmentation with a barometer and a gyro can further improve availability. While the barometric height measurements are dependent upon atmospheric pressure and temperature, the barometer demonstrated unexpectedly good performance for land vehicle navigation due to the relatively stable local atmosphere and temperature. The tests in the controlled environment and downtown area have indicated that rubidium clock aided GPS integrated with a barometer can navigate using two

satellites. The positioning accuracy is mainly dependent upon the constellation of the satellites and the accuracy of barometric height measurements.

The gyro's measurements are not as reliable as the barometer's. Large heading measurement errors are induced once the vehicle is tilted. The gyro, therefore, needs to be calibrated frequently by the GPS measurements. Although the rubidium clock aided GPS integrated with a barometer and a gyro is capable of performing one satellite navigation, the navigation performance is determined to a large extent by the gyro heading measurements. Fortunately, for land vehicle navigation in a downtown area, most streets are smooth and flat. The test in downtown Calgary revealed that the gyro measurements depend on the GPS calibration quality. Since the number of visible satellites often falls to two (for nearly 35% of time), the quality of GPS heading measurements, which are derived from the GPS velocity, can not be ensured at all times.

Using a barometer and a gyro without clock aiding is an alternative integration approach. GPS/barometer integration provides nearly the same navigation availability and accuracy to that of rubidium aided GPS. Both navigation algorithms can perform three-satellite navigation for a relatively long time, provided that the satellite geometry is adequate for the purpose.

GPS/barometer/gyro integration has comparable availability as that of rubidium clock aided GPS/barometer integration. The latter often provides superior position solutions to the former under the same conditions. Since the barometric measurements are reliable in a local area, rubidium clock aided GPS integrated with a barometer is able to perform two-satellite navigation for a long time as long as the satellite geometry is adequate. GPS/barometer/gyro integration, however, can not perform two-satellite navigation for very long. Since the position solution is propagated on the basis of the last position solution and the gyro heading measurement, unpredictable gyro drifts will result in

divergence of the Kalman filter. Of the all integration modes, the rubidium clock aided GPS/barometer/gyro provides the highest availability.

7.2 Recommendations

The rubidium clock has proven to be stable enough for clock aiding of GPS. It is still of interest to investigate whether or not a lower cost clock, such as a high quality oven-controlled crystal oscillator (OCXO) clock, is suitable for clock aiding GPS. The OCXO clock drifts much faster than the rubidium clock does, so the OCXO clock modeling would be different from the rubidium clock modeling.

The silicon strain gage barometer, which senses the deformation of the silicon, was shown to have a time lag. If the lag could be modeled precisely, the barometric height measurement would be improved significantly. The performance of the integrated system, thus, would be further enhanced.

Inclination of the vehicle induces large errors in the gyro heading measurements, since the gyro is mounted directly on the vehicle's frame. Using the past and updated position estimates to estimate the slope and using the gyro rate measurements to estimate the tilt angle might help to reduce the errors. The obvious solution for heading measurements, however, is to add a magnetic compass to the system. Combination of the compass and gyro will overcome each other's weakness. In a downtown area, adding a distance/speed sensor, such as an odometer, to obtain a dead reckoning system would also improve availability and accuracy.

Finally, the use of GPS/GLONASS, instead of GPS only, would also significantly enhance availability (e.g. Lachapelle et al. 1997).

REFERENCE

Allan, D.W. (1961), "Statistics of Atomic Frequency Standards," Proc. of the IEEE, vol. 54, pp. 221-230.

Andrew Corporation (1994), "AUTOGYRO Installation Manual", Document No. 37318, Rev. A, P/N 224894, St. Petersburg, FL.

Ball Efratom Division (1989), "Low Noise Rubidium Frequency Standard Operation and maintenance Manual,".

Bedrosian, E. (1962), "The Analytic Signal Representation of Modulated Waveforms," Proc. IRE, vol. 50, pp. 2071-2076.

Bernier, L.G., Gardiol, F.E. (1985), "The Analytic Signal Representation of Oscillators with Application to Frequency Stability Analysis," Proc. of the 39th Annual Frequency Control Symposium, Philadelphia, pp. 127-131.

Blais, J.A.R. & Vassiliou, A.A. (1987), "Spectral Analysis of One-dimensional Data Sequence", Technical Report, Department of Geomatics Engineering, The University of Calgary.

Brown, R.G. & Hwang, P.Y.C. (1992), "Introduction to Random Signals and Applied Kalman Filtering", John Wiley & Sons, Inc.

Bullock, J.B. (1995), "A Prototype Portable Vehicle Navigation System Utilizing Map Aided GPS", UCGE Reports Number 20081, Department of Geomatics Engineering, The University of Calgary.

Cannon, M.E. (1991), "Airborne GPS/INS with an Application to Aerotriangulation", Ph.D. Dissertation, Dept. of Geomatics Engineering, The University of Calgary.

Cannon, M.E., Lachapelle, G. and Qiu, W. (1995), "C^{3}NAV^{TM} Operating Manual", The University of Calgary.

Cannon, M.E., G. Lachapelle, M. Szarmes, J. HeberT, J. Keith, and S. Jokerst (1997), "DGPS Kinematic Carrier Phase Signal Simulation Analysis for Precise Velocity and Position Determination." Proceedings of National Technical Meeting , The Institute of Navigation, Alexandria, VA., 335-350.

Carlson, N.A. (1988), "Information-sharing Approach to Federal Kalman Filtering", Proceedings of National Aerospace Electronics Conference, Naecon, Dayton, pp. 228 - 238.

Damper, R.I. (1995), "Introduction to discrete-time signals and systems," New York : Chapman & Hall.

Gao, Y. (1992), "A Robust Quality Control System for GPS Navigation and Kinematic Positioning", Master's Thesis, Department of Geomatics Engineering, The University of Calgary.

Gao, Y., Heroux, P. and Kouba, J. (1994), "Estimation of GPS Receiver and Satellite L1/L2 Signal Delay Biases Using Data From CACS," Proc. of KIS94, Banff, Canada, pp. 109-117.

GPS Silicon Valley (1994), "Installation and Operation Manual for GPS Frequency Reference Generator".

Hayashi, N. (1996a), "Augmentation of GPS with a Barometer and a Heading Rate Gyroscope for Urban Vehicular Navigation," Master Thesis, Report No. 20098, Department of Geomatics Engineering, The University of Calgary.

Hayashi, N. (1996b), "Low-cost Sensor Constraint GPS Vehicle Navigation in an Urban Environment", Proc. ION GPS-96, pp. 1409 - 1417.

Henriksen, J., G.Lachapelle, J.Raquet and J.Stephen (1996), "Analysis of Stand-Alone GPS Positioning Using Post-Mission Information", Proc. ION GPS-96, 251 - 259.

Heroux, P. (1997), "Personal Communication with Jamie Henriksen,".

Hwang, P.Y.C. & Brown, R.G. (1990), "GPS Navigation Combining Pseudo-range with Continuous Carrier Phase Using a Kalman Filter", Navigation, The Jour of the Institute of Navigation, 37:2.

Kouba, J. and Popelar, J. (1994), "Modern Geodetic Reference Frames for Precise Satellite Positioning and Navigation," Proc. of KIS94, Banff, Canada, pp. 79-85.

Krakiwsky, E.J. (1990), "The Method of Least Squares: A Synthesis of Advances," UCGE Reports No. 10003, Department of Geomatics Engineering, The University of Calgary.

Lachapelle, G. (1995), "GPS Theory and Applications," ENGO 625 Lecture Notes Department of Geomatics Engineering, The University of Calgary.

Lachapelle, G., Cannon, M.E., Tang, C., Lan, H., Wee, S., Ryan, S. and Forbes, F. (1996) "Shipborne and Airborne DGPS Positioning Using Various Receiver Technologies

and RTCM Message Types 1/9 and 18-21," Canadian Aeronautics and Space Journal, vol. 42, No. 1, March 1996, pp. 37-44.

Lachapelle, G., S. Ryan, M. Petovello, and J. Stephen (1997), "Augmentation of GPS-GLONASS for Vehicular Navigation Under Signal Masking." Proceedings of GPS97, The Institute of Navigation, Alexandria, VA, 1511 - 1519.

Lee, Y.C. (1993), "RAIM Availability for GPS Augment with Barometric Altimeter Aiding and Clock Coasting", Navigation, The Journal of ION, Vol. 40, No. 2, pp. 179-198.

Lutgens, F.K. and Tarbuck, E.J. (1982), "The Atmosphere - An Introduction to Meteorology", Second Edition, Prentice-Hall Inc., Englewood Cliffs, NJ.

Martin, E.H. (1980), "GPS User Equipment Error Models," Global Positioning System Papers, Vol. I, ION, Washington DC, pp. 109-118.

McBurney, P.W. and Brown, R.G. (1988), "Receiver Clock Stability: An Important Aid in GPS Integrity Problem", Poc. ION National Technical Meeting, Santa Barbara, CA, 526 - 537.

Misra, P., M. Pratt, B. Burk and R. Ferranti (1995a), "Adaptive Modeling of Receiver Clock for Meter-level DGPS Vertical Positioning", Proceeding of ION GPS-95, pp. 1127 - 1135.

Misra, P., M. Pratt, R. Muchnik and B. Manganis (1995b), "A General RAIM Algorithm Based on Receiver Clock", Proc. ION GPS-95, 1941 - 1948.

Murphy, J.J. and Skidmore, T.A. (1994), "A Low-cost Atomic Clock: Impact on the

National Airspace and GNSS Availability", Proceeding of ION GPS-94, Salt Lake City, pp. 1329-1336.

NovAtel (1994), "GPSCard OEM Series Installation and Operating Manual,".

Priestley, M.B. (1981), "Spectral Analysis and Time Series", Academic Press, Inc., Harcourt Brace Jovanovich.

Papoulis, A. (1984) Probability, Random Variables, and Stochastic Processes, 2nd Edition, McGraw-Hill Book Co., New York.

Siouris, G.M. (1993), "Aerospace Avionics Systems - A Modern Synthesis," Academic Press, Inc., Harcourt Brace & Company.

Skone, S., M.E.Cannon, K.Lochhead, P.Heroux and F.Lahaye (1996), "Performance Evaluation of the NRCAN Wide Area System", Proc. ION GPS-96, 1793 - 1802.

Sturza, M.A. (1984), "GPS Navigation Using Three Satellites and a Precise Clock", Global Positioning System, Vol. ii, Washington, DC: The Institute of Navigation, pp. 122-132.

Sydnor, R. and Allan, D.W. (1996), " The Selection and Use of Precise Frequency and Time Systems," ITU Handbook.

Viatran Corporation (1995), "X45/X46 Series Pressure Transducers Installation Data," Grand Island, NY.

Yu, J. (1984), "Kalman Filter and Its Application in INS", Northwestern Polytechnical University Press, Xian, China.

APPENDIX A

RESULTS OF DOWNTOWN CALGARY TEST

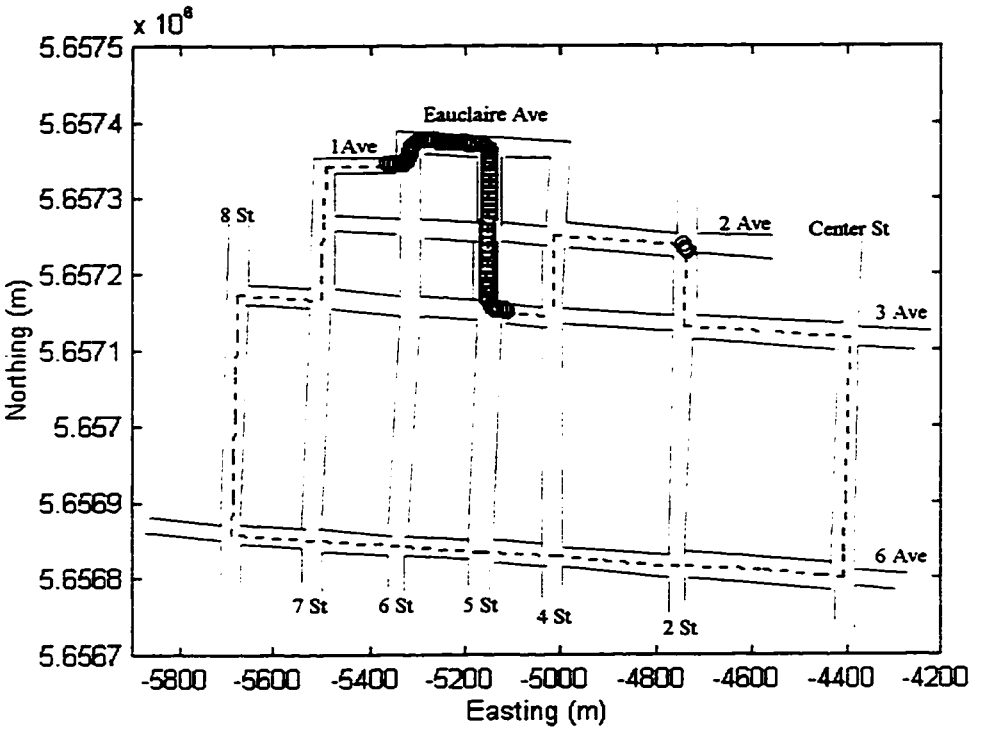

Figure A.1 Run #2, using unaided GPS

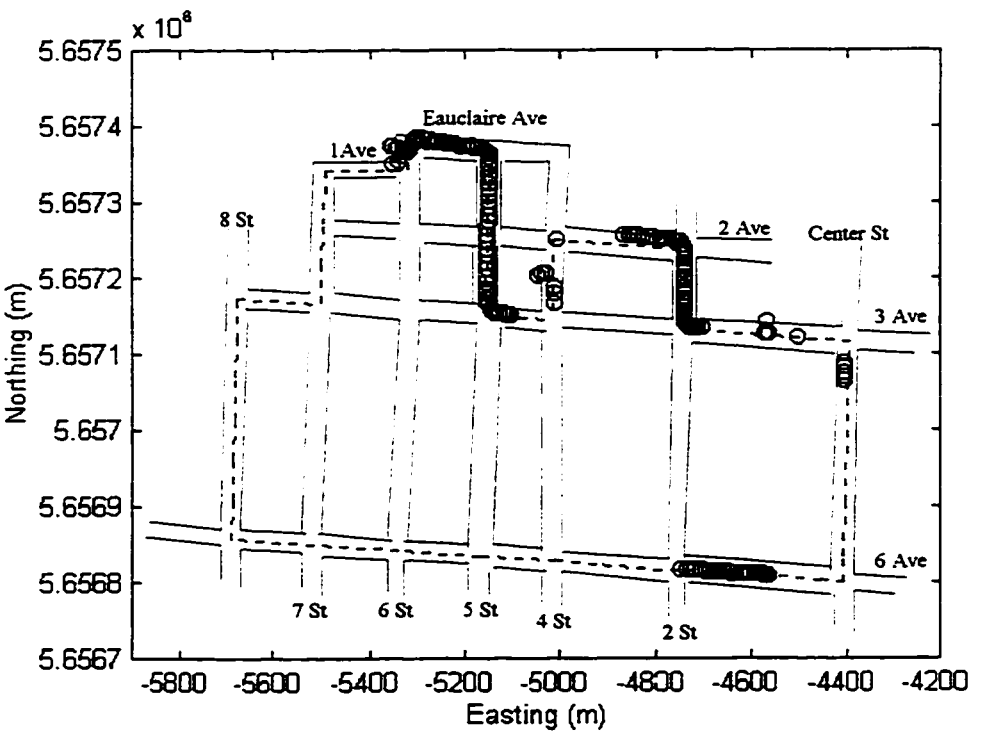

Figure A.2 Run #2, using rubidium clock aided GPS

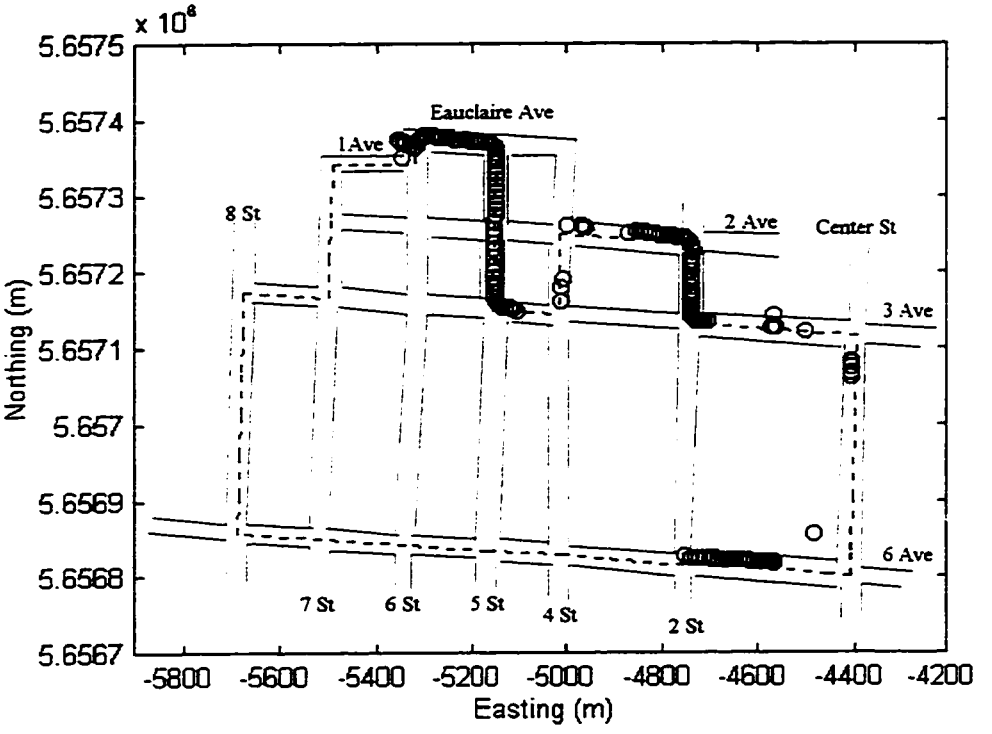

Figure A.3 Run #2, using GPS/barometer integration

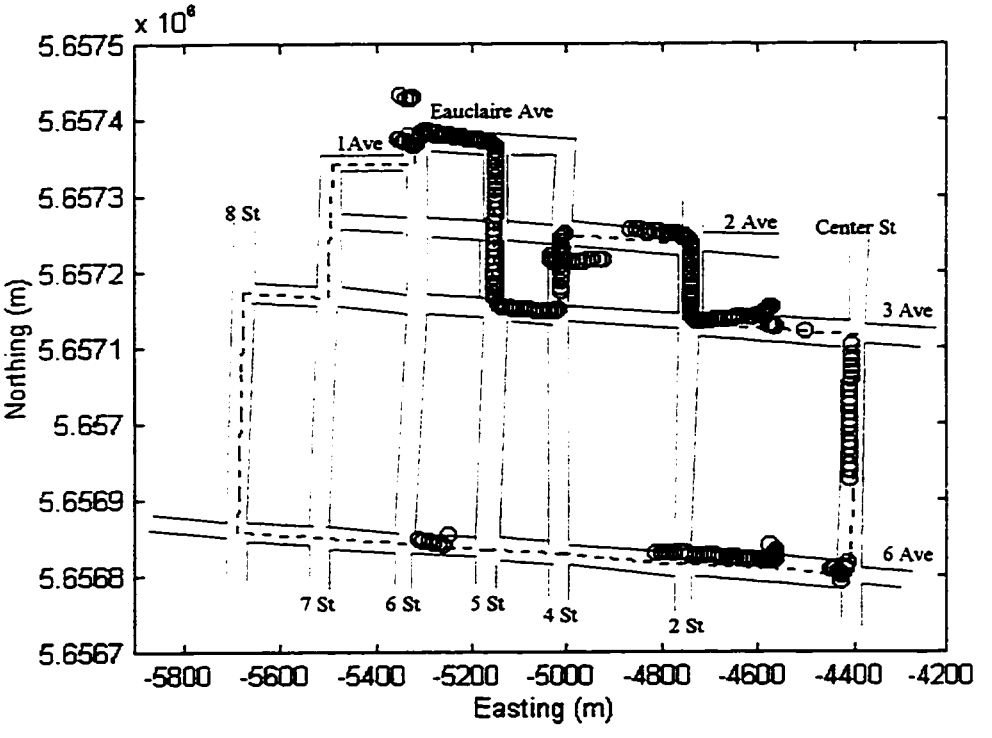

Figure A.4 Run #2, using rubidium clock aided GPS/barometer integration

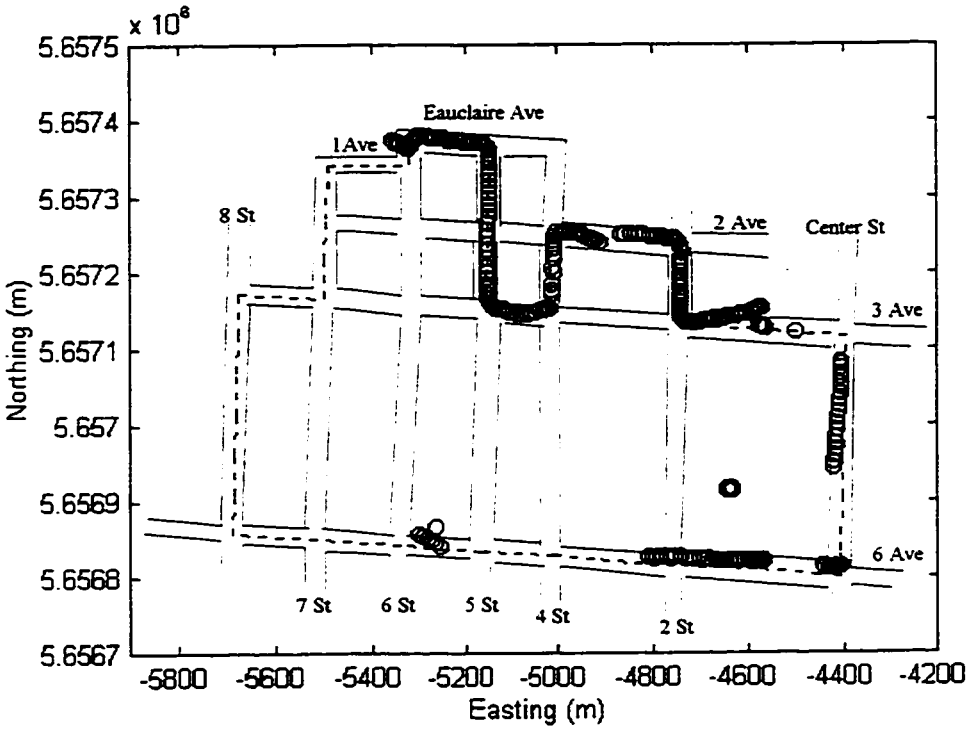

Figure A.5 Run #2, using GPS/barometer/gyro integration

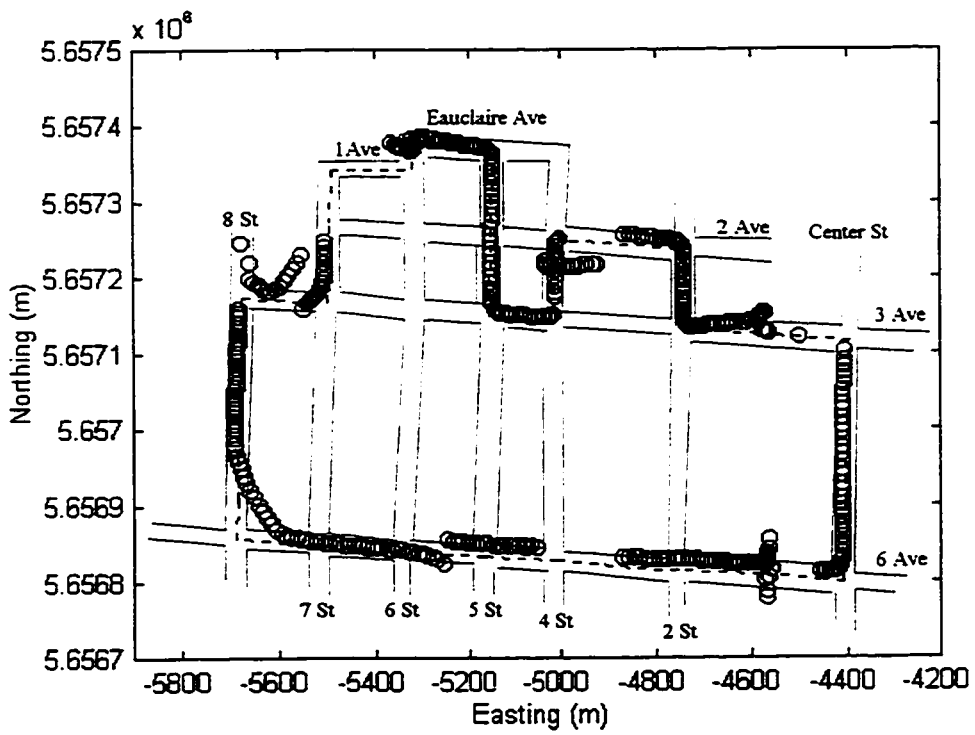

Figure A.6 Run #2, using rubidium clock aided GPS/barometer/gyro integration

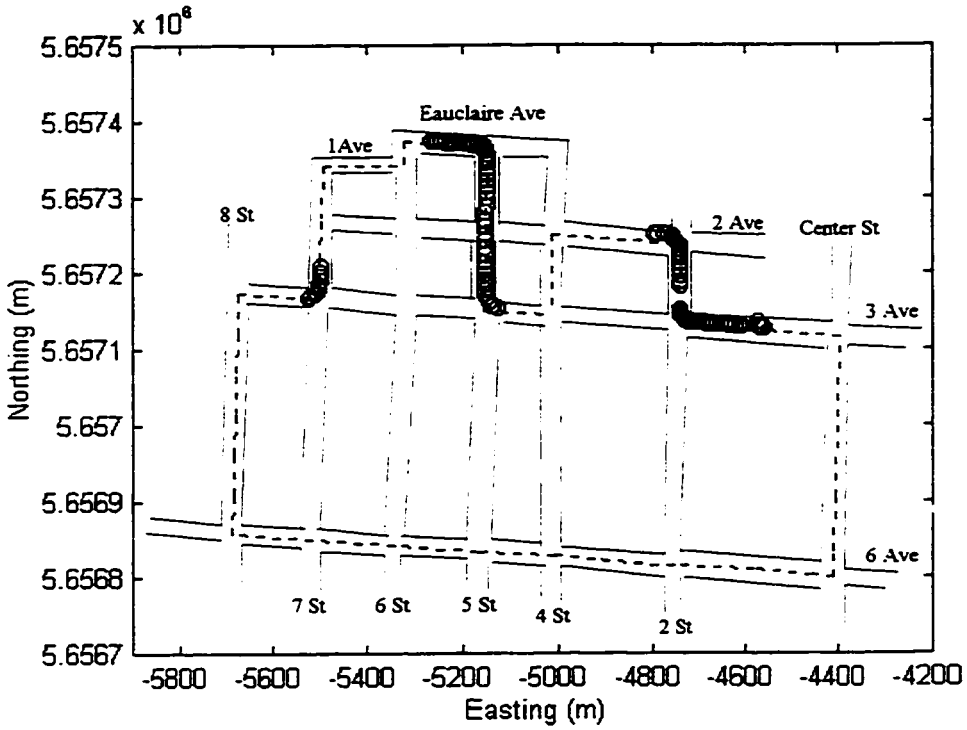

Figure A.7 Run #3, using unaided GPS

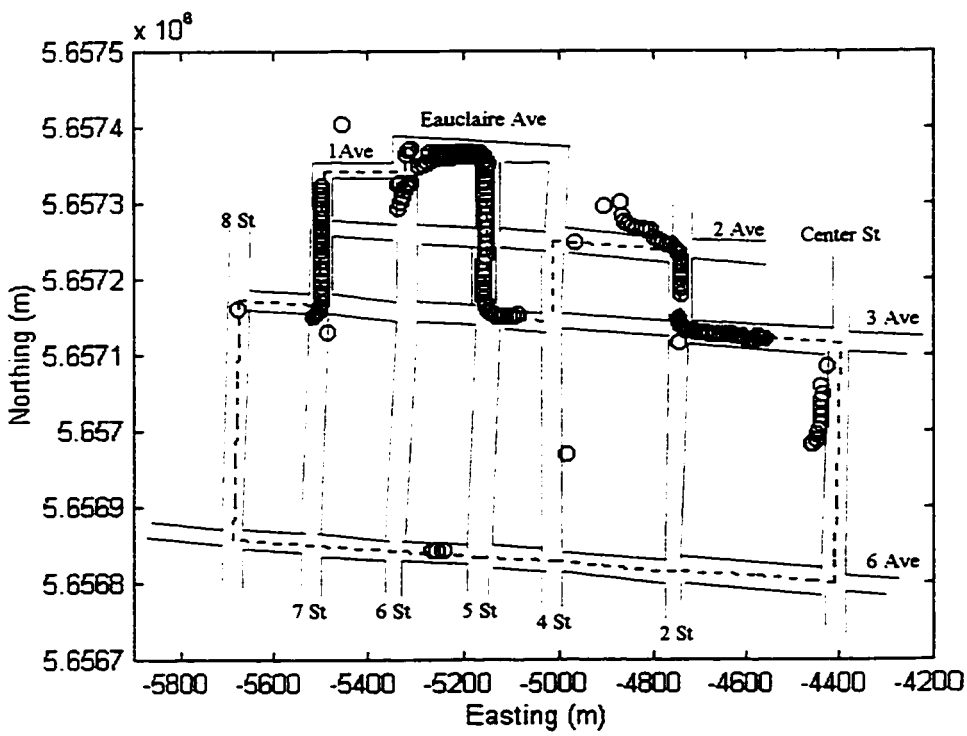

Figure A.8 Run #3, using rubidium clock aided GPS

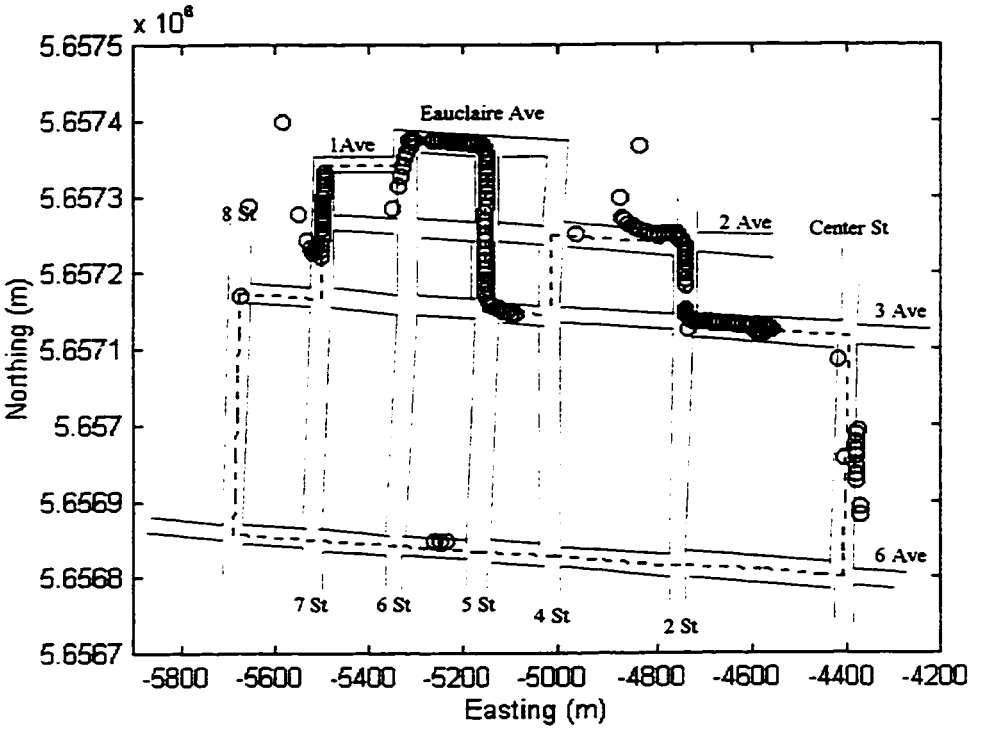

Figure A.9 Run #3, using GPS/barometer integration

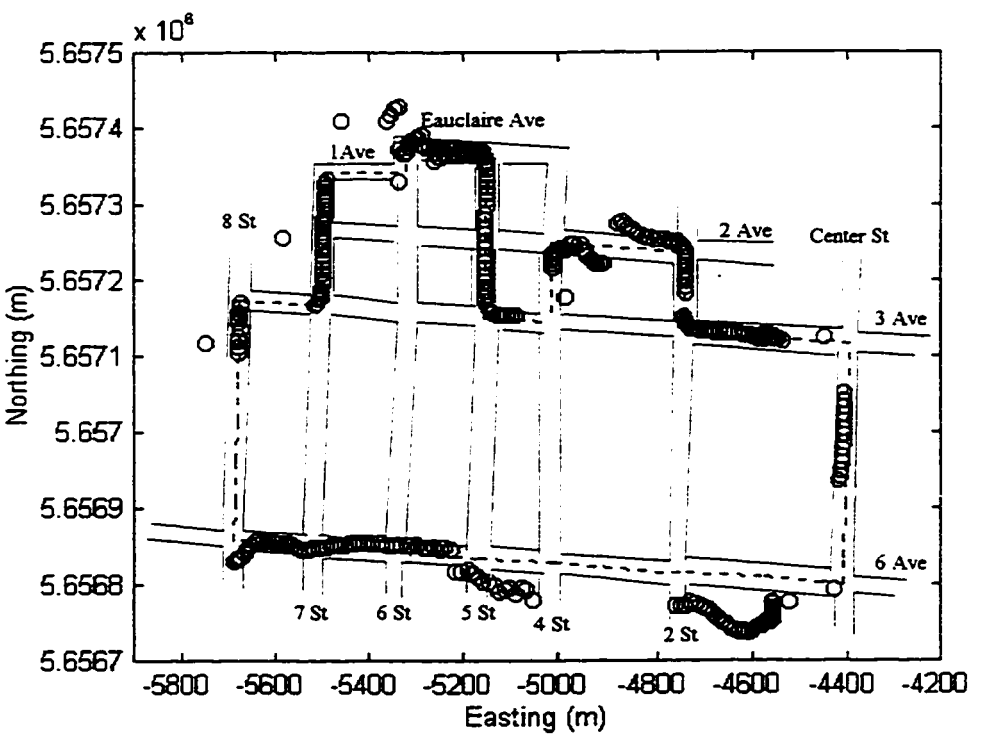

Figure A.10 Run #3, using rubidium clock aided GPS/barometer integration

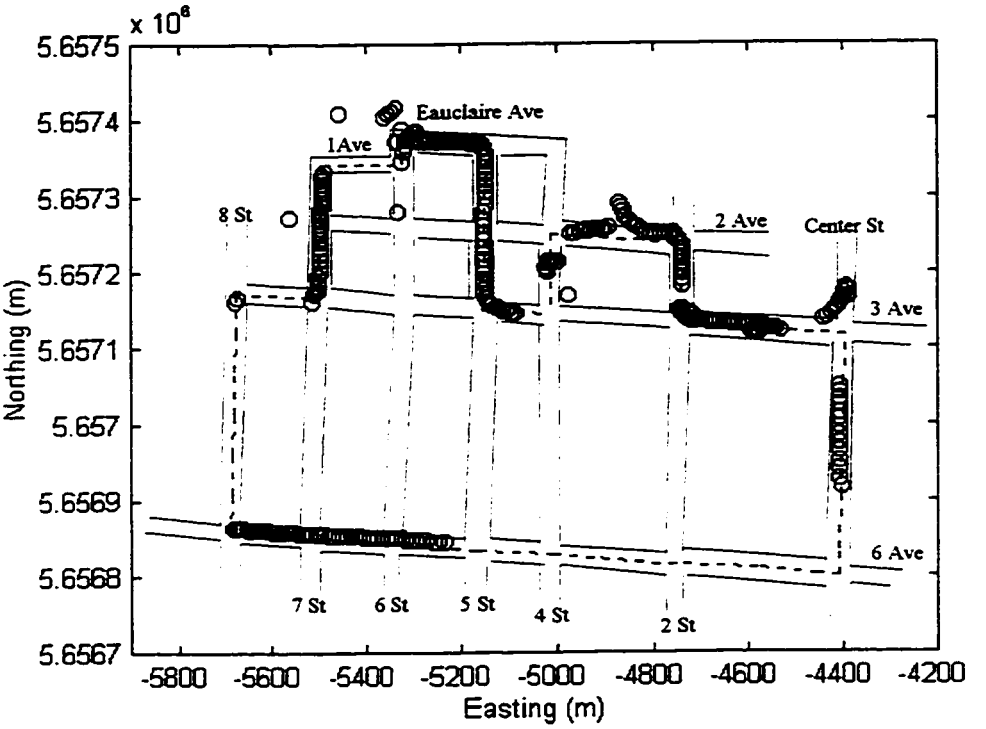

Figure A.11 Run #3, using GPS/barometer/gyro integration

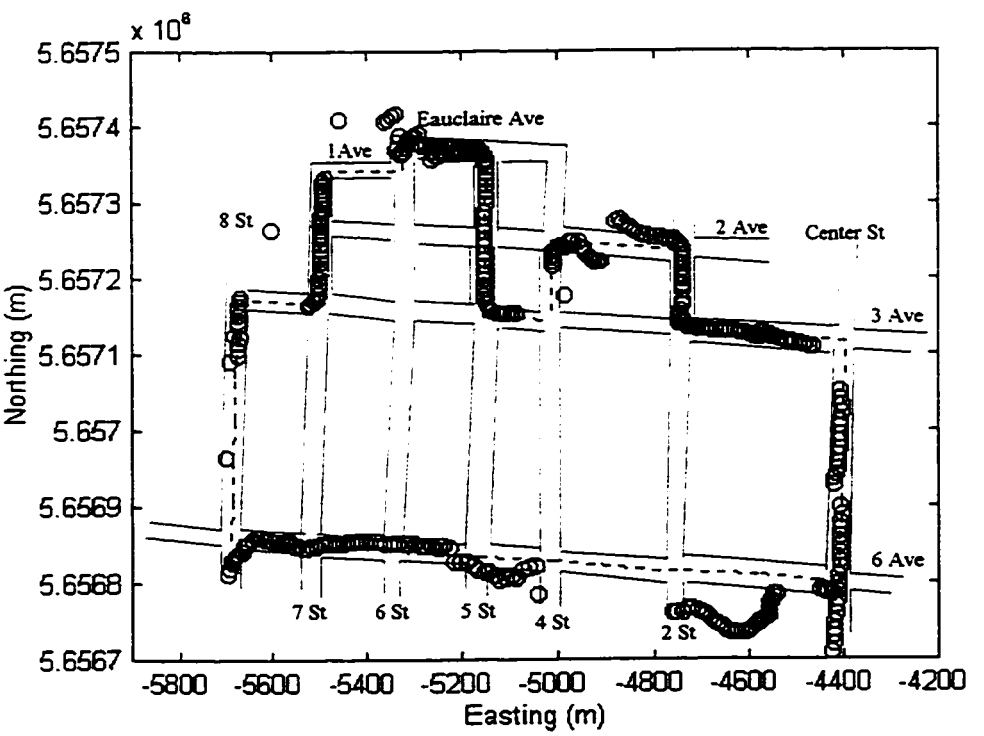

Figure A.12 Run #3, using rubidium clock aided GPS/barometer/gyro integration

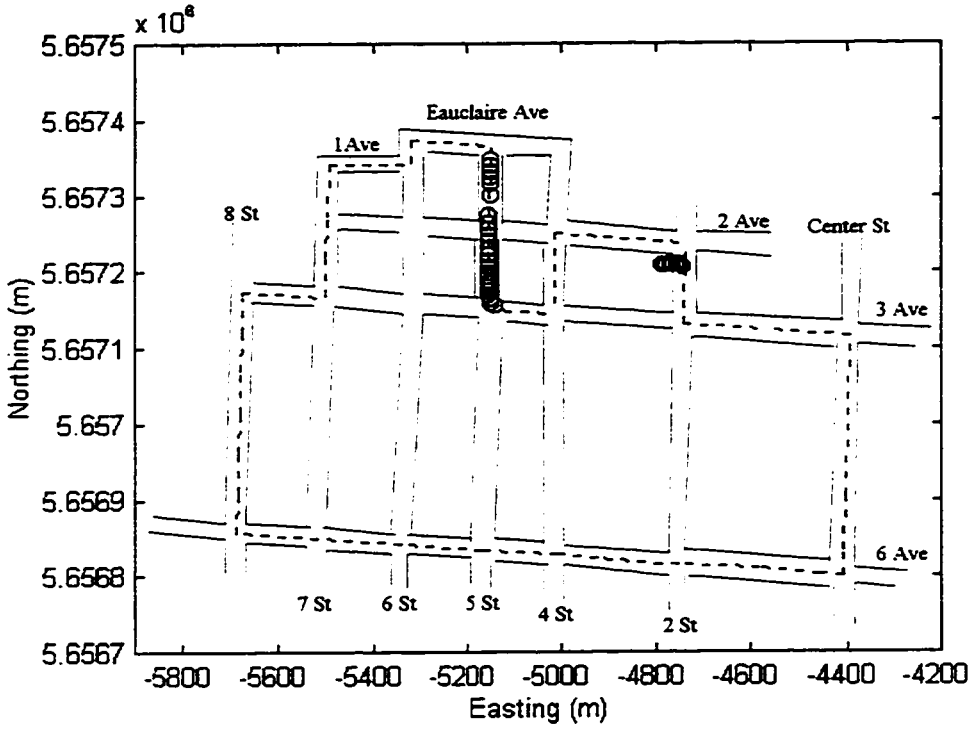

Figure A.13 Run #4, using unaided GPS

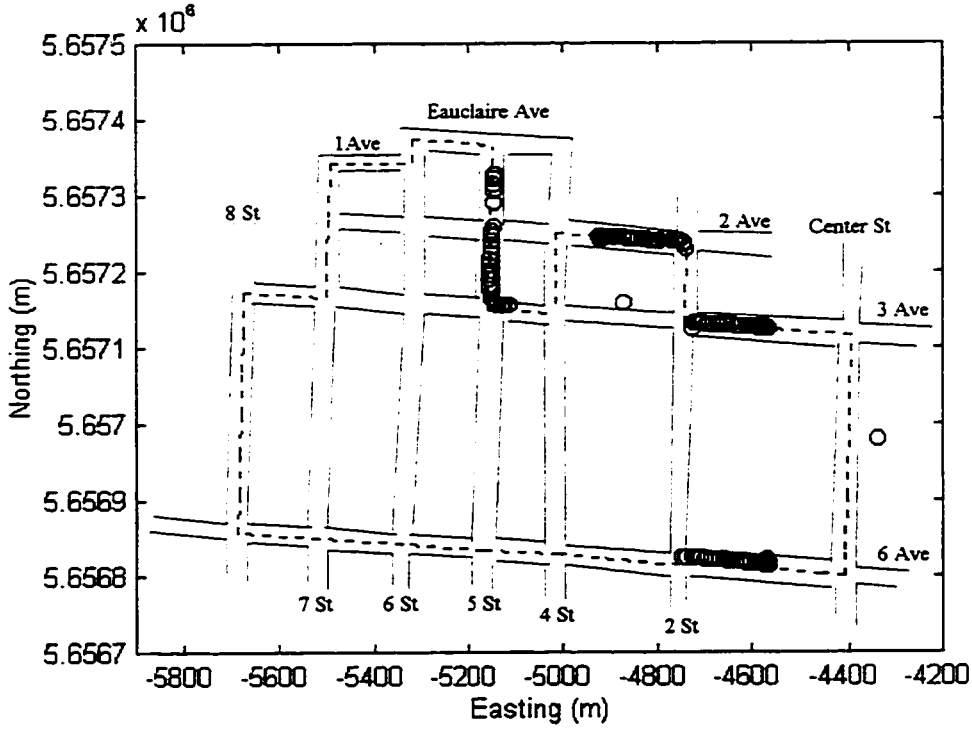

Figure A.14 Run #4, using rubidium clock aided GPS

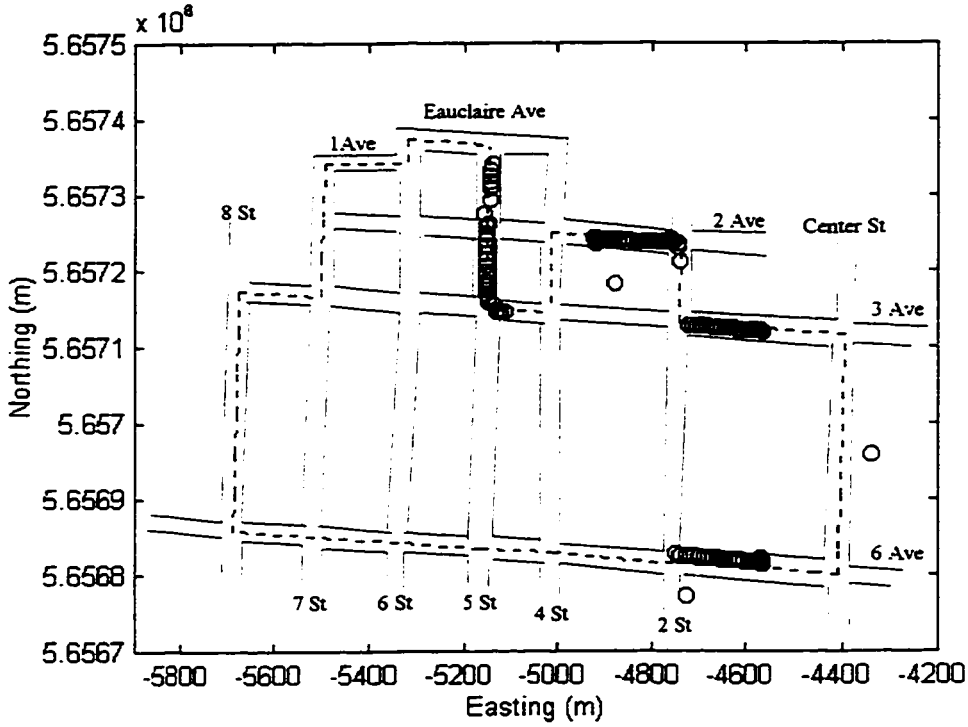

Figure A.15 Run #4, using GPS/barometer integration

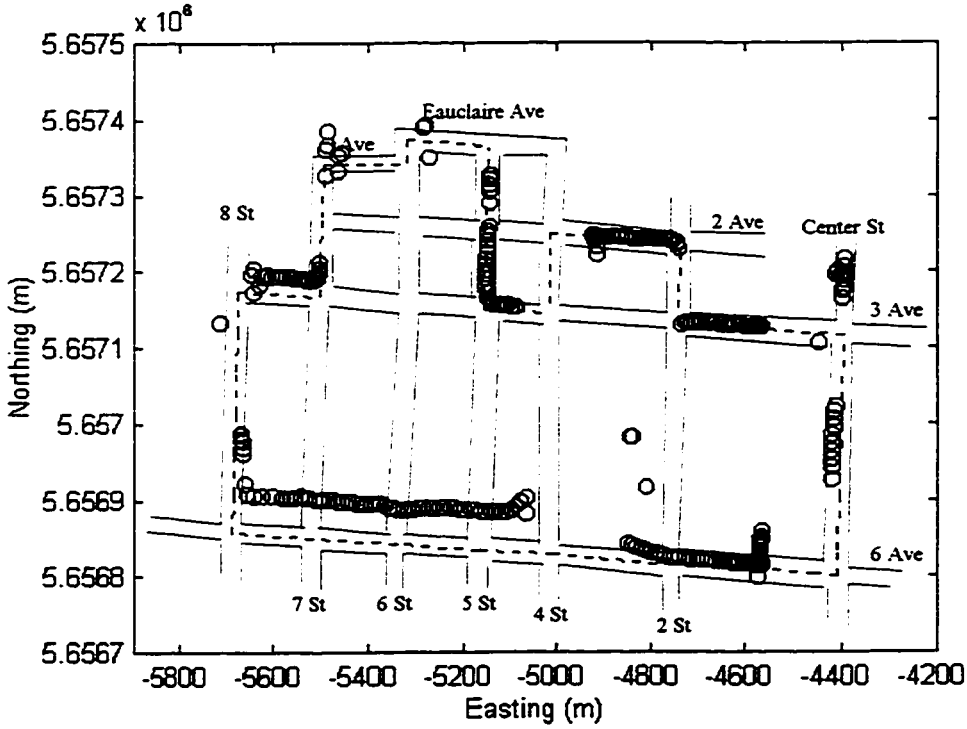

Figure A.16 Run #4, using rubidium clock aided GPS/barometer integration

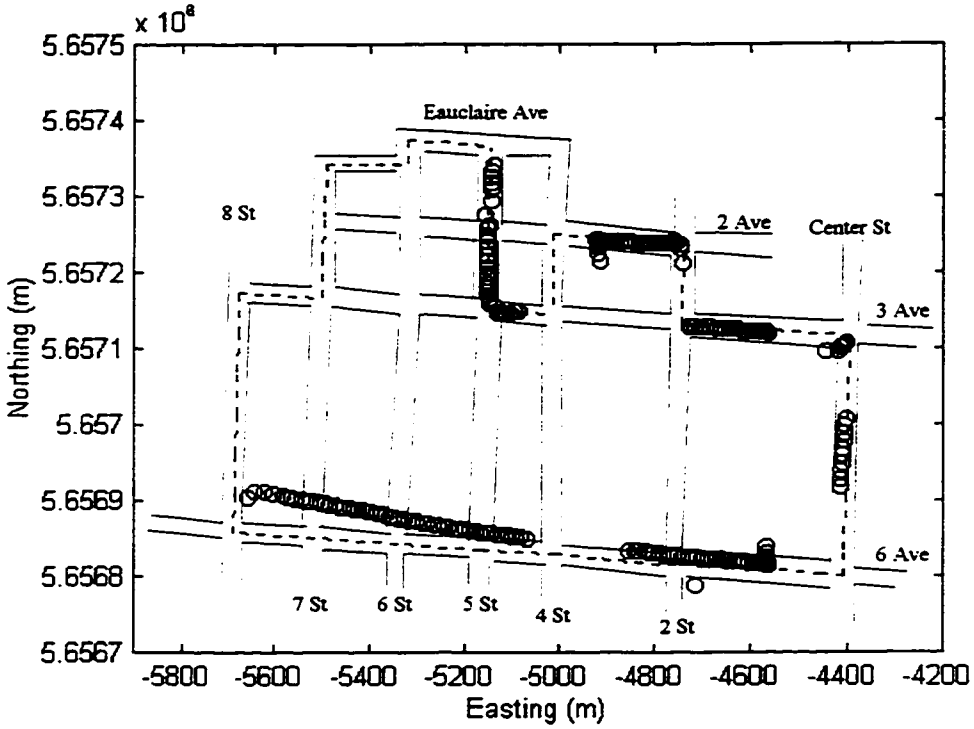

Figure A.17 Run #4, using GPS/barometer/gyro integration

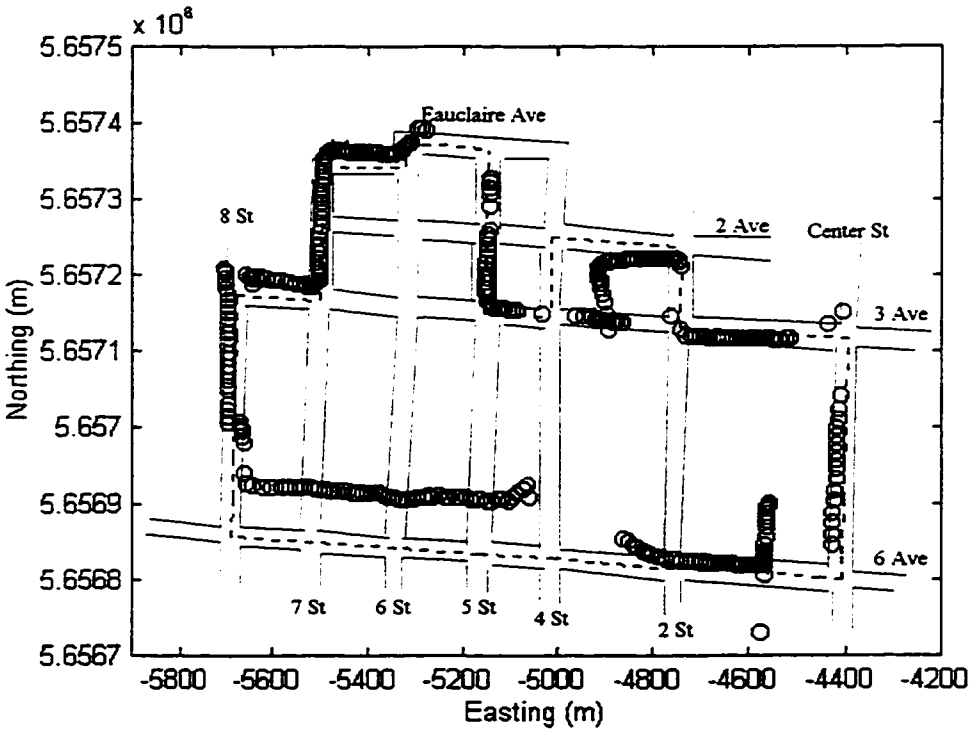

Figure A.18 Run #4, using rubidium clock aided GPS/barometer/gyro integration

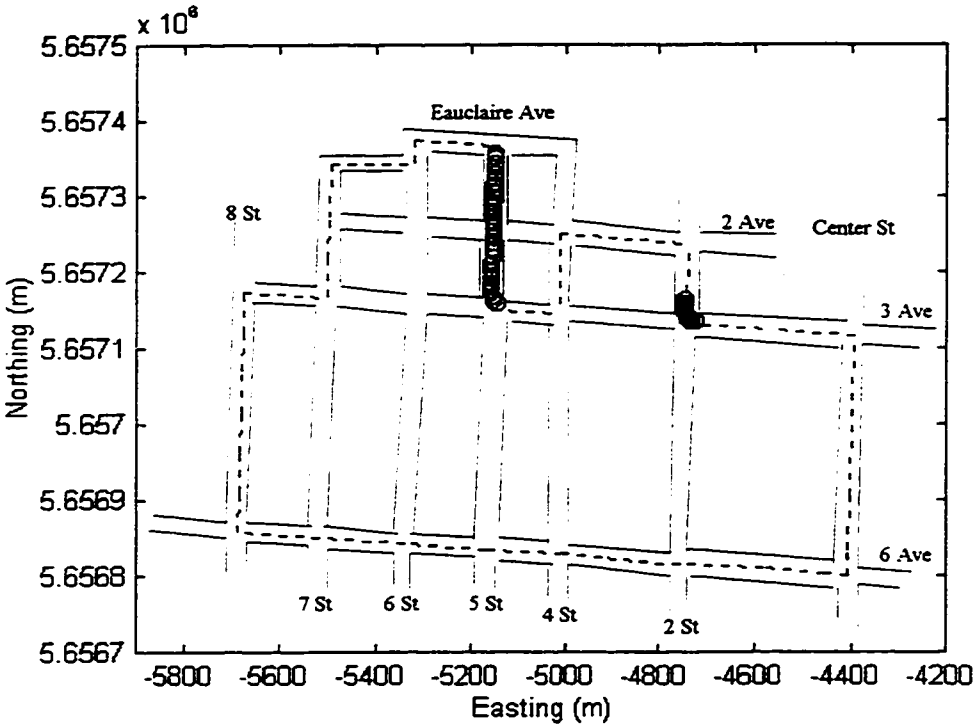

Figure A.19 Run #7, using unaided GPS

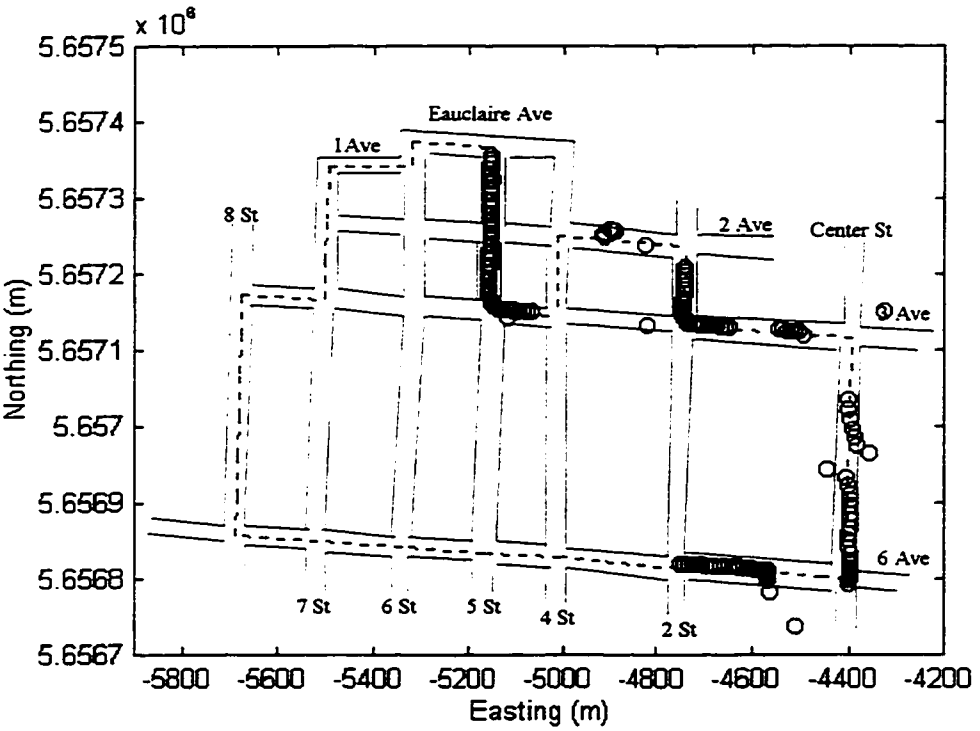

Figure A.20 Run #7, using rubidium clock aided GPS

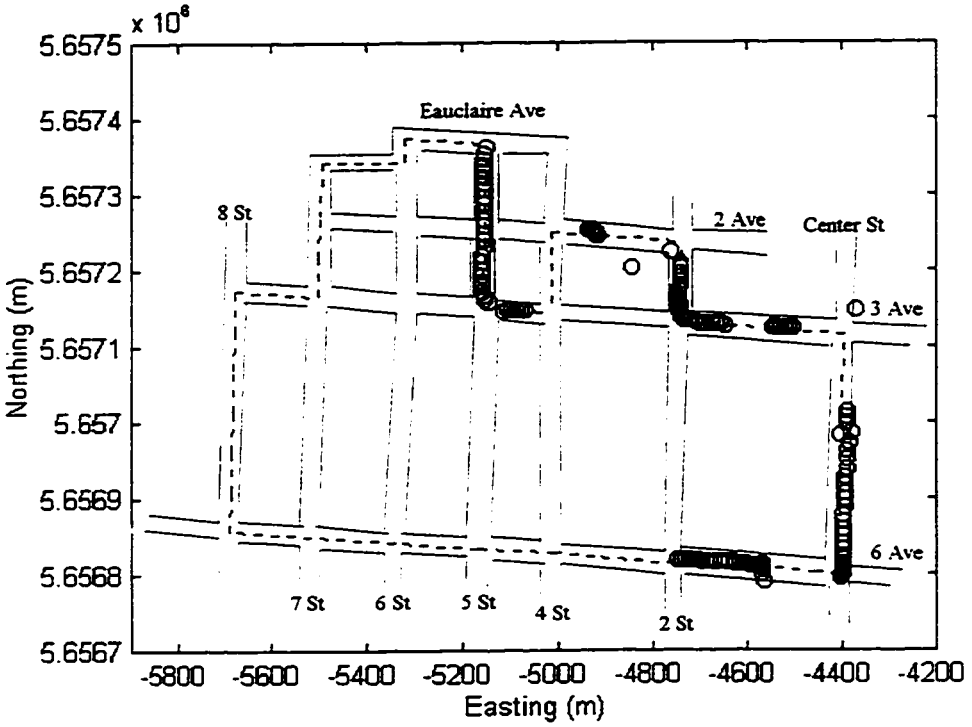

Figure A.21

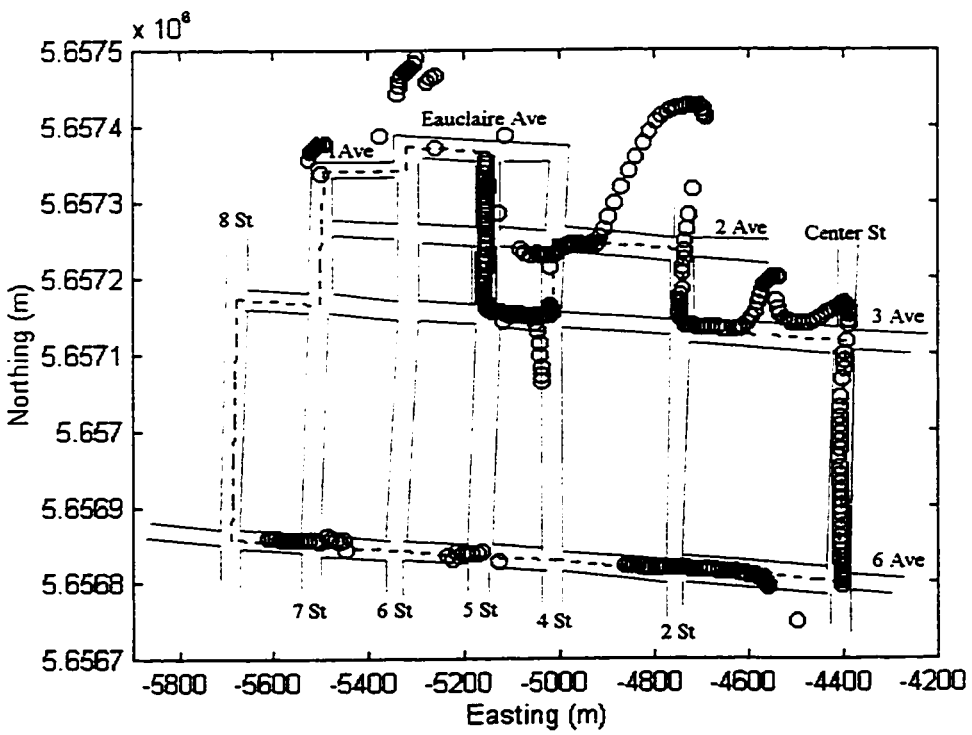

Figure A.22 Run #7, using rubidium clock aided GPS/barometer integration

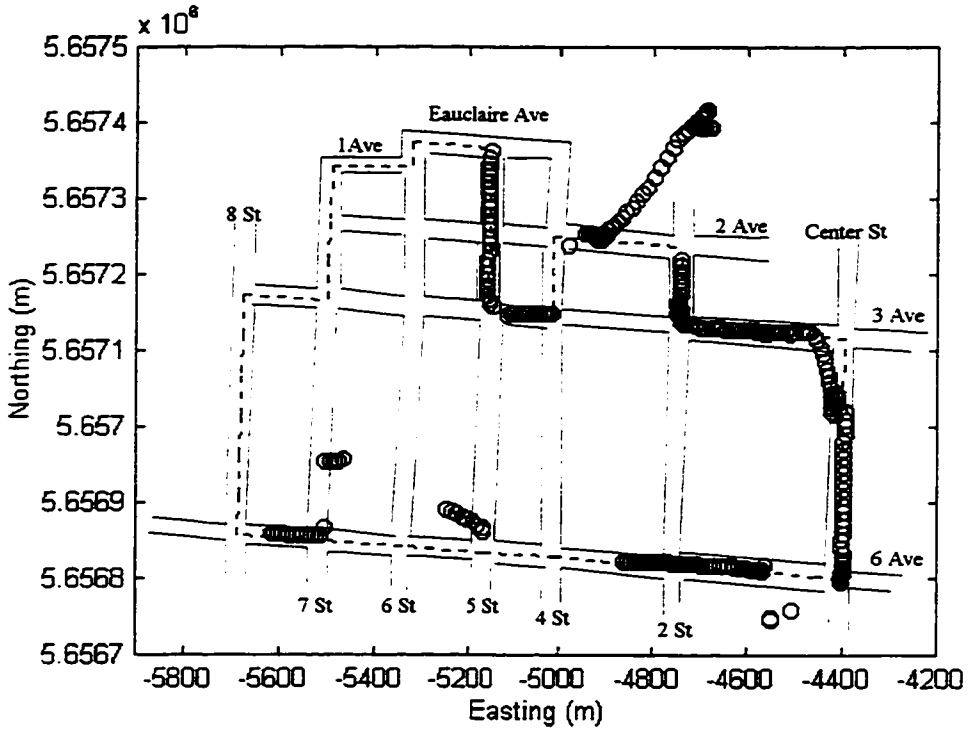

Figure A.23 Run #7, using GPS/barometer/gyro integration

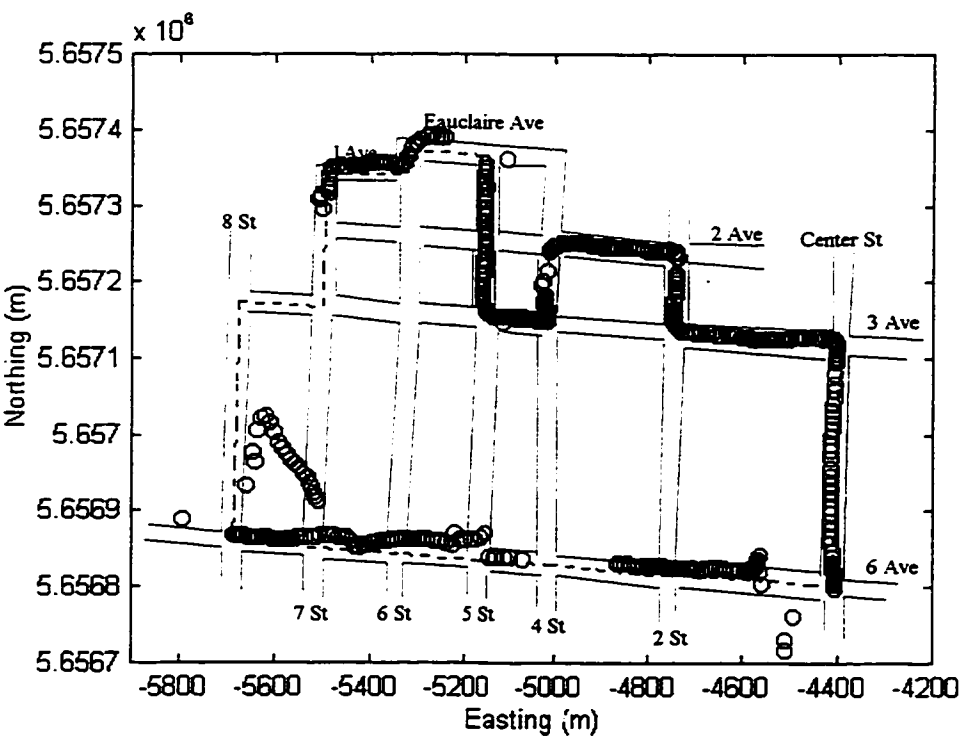

Figure A.24 Run #7, using rubidium clock aided GPS/barometer/gyro integration

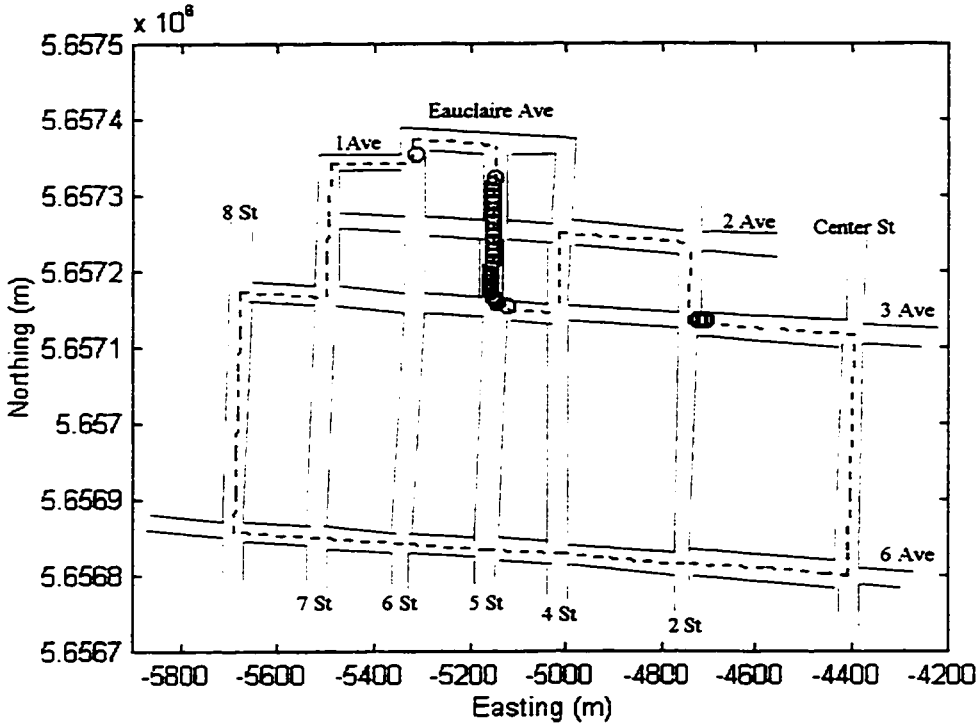

Figure A.25 Run #8, using unaided GPS

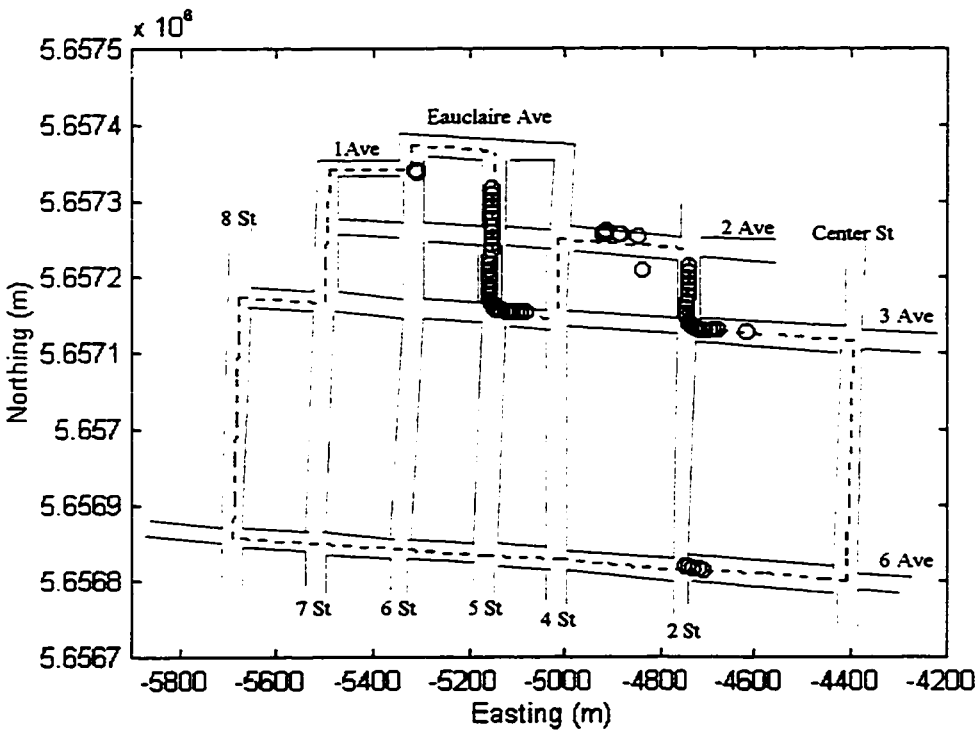

Figure A.26 Run #8, using rubidium clock aided GPS

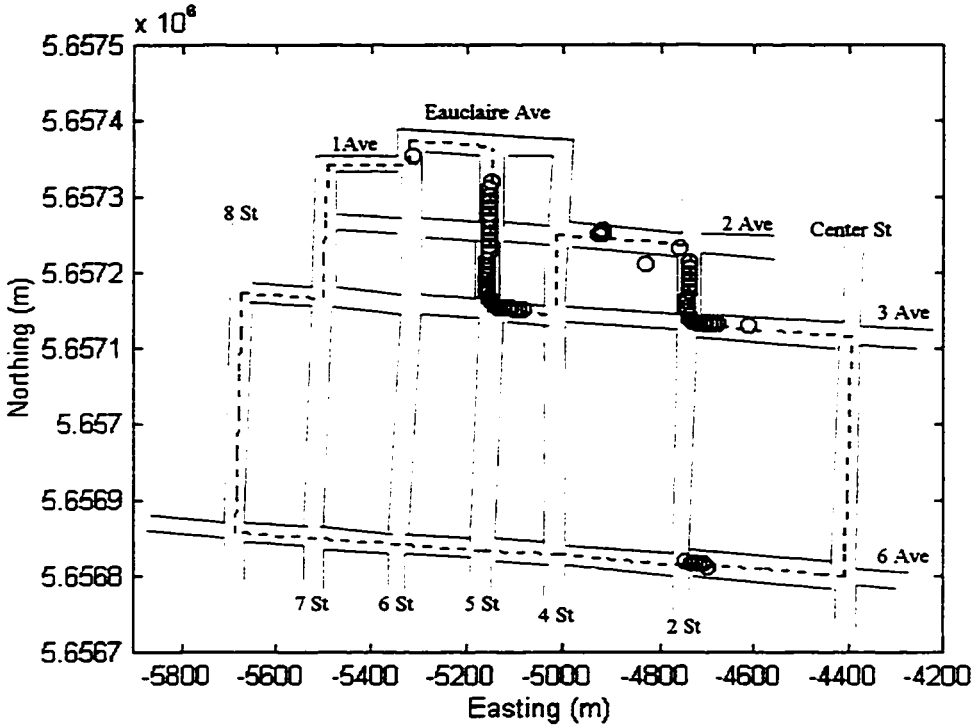

Figure A.27

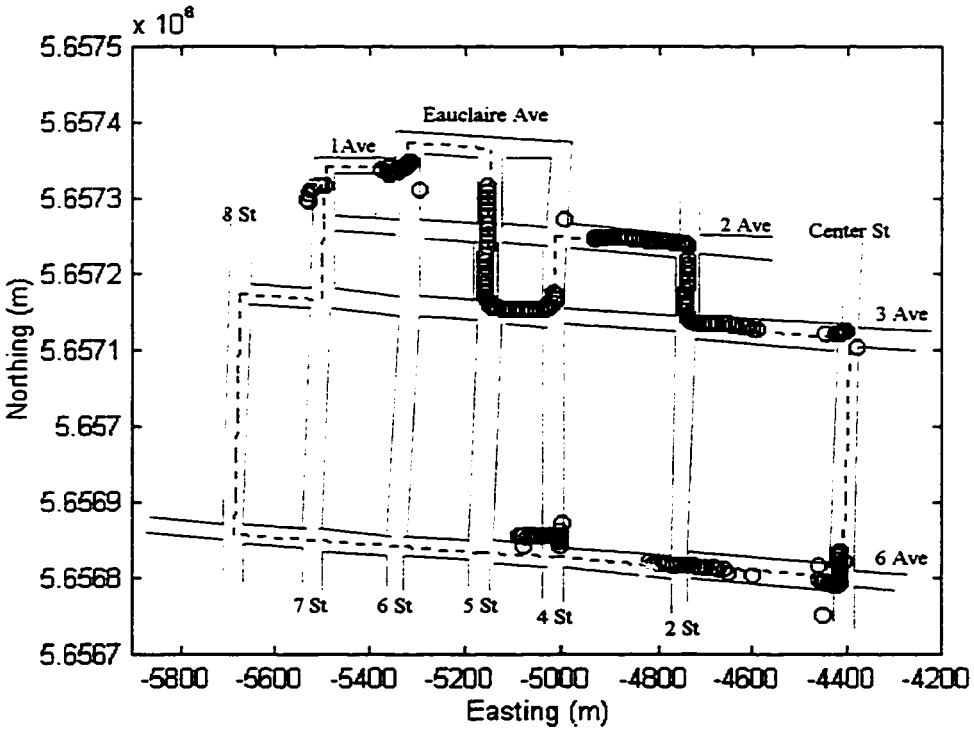

Figure A.28 Run #8, using rubidium clock aided GPS/barometer integration

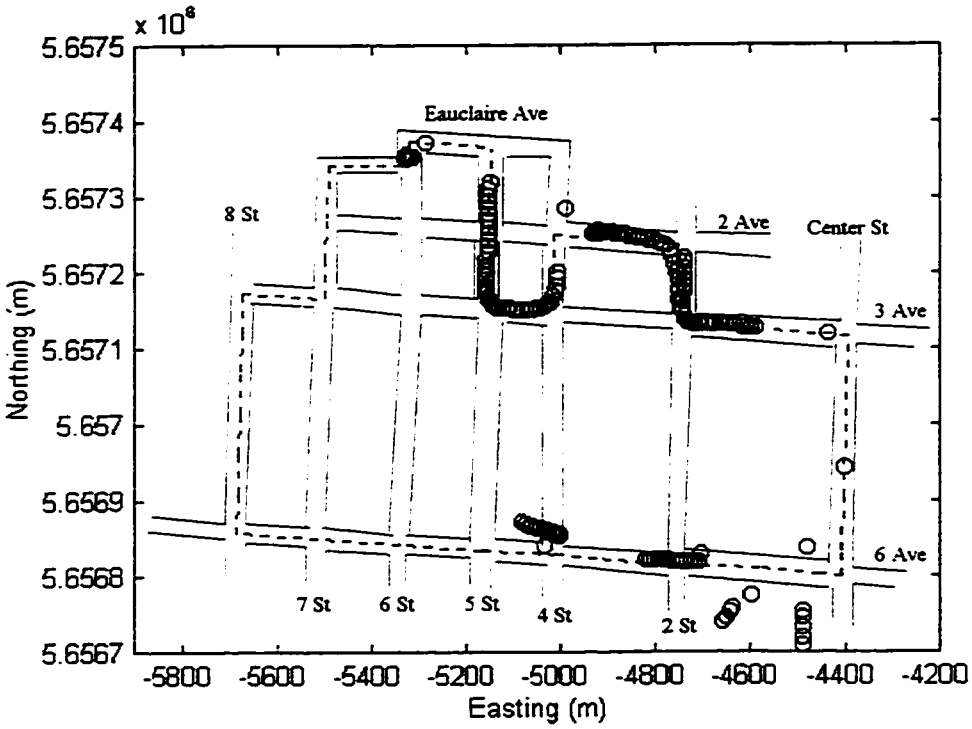

Figure A.29 Run #8, using GPS/barometer/gyro integration

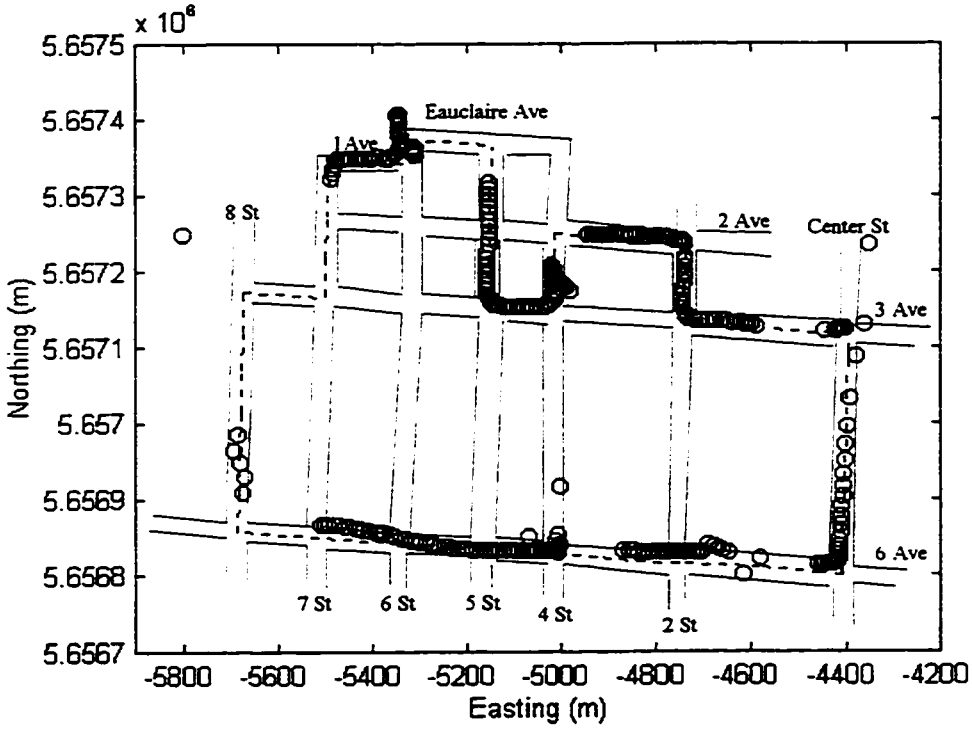

Figure A.30 Run #8, using rubidium clock aided GPS/barometer/gyro integration

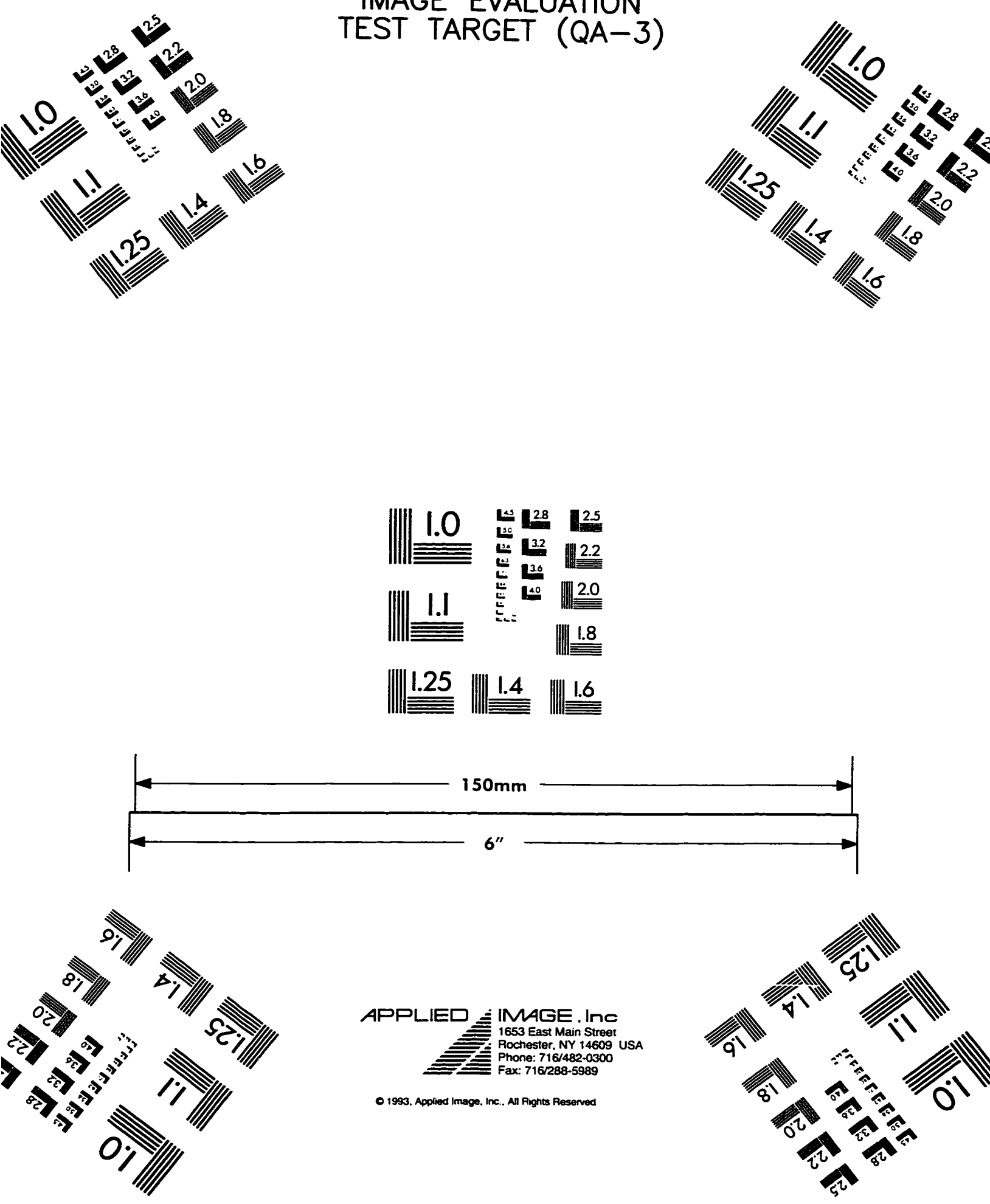
IMAGE EVALUATION
TEST TARGET (QA-3)
1.0
1.1
1.25
1.4
1.6
1.8
2.0
2.2
2.5
2.8
3.2
3.6
4.0
150mm
6"
APPLIED IMAGE, Inc
1653 East Main Street
Rochester, NY 14609 USA
Phone: 716/482-0300
Fax: 716/288-5989
© 1993, Applied Image, Inc., All Rights Reserved